NUREG/CR-2331
BNL-NUREG-51454
VOL. 3, NO. 3

SAFETY RESEARCH PROGRAMS SPONSORED BY OFFICE OF NUCLEAR REGULATORY RESEARCH

QUARTERLY PROGRESS REPORT
JULY 1 — SEPTEMBER 30, 1983

Date Published — January 1984

DEPARTMENT OF NUCLEAR ENERGY, BROOKHAVEN NATIONAL LABORATORY
UPTON, NEW YORK 11973

Prepared for the U.S. Nuclear Regulatory Commission
Office of Nuclear Regulatory Research
Contract No. DE-AC02-76CH00016

NUREG/CR-2331
BNL-NUREG-51454
VOL. 3, NO. 3
AN, R-1,4,5,7,8, RD

SAFETY RESEARCH PROGRAMS SPONSORED BY OFFICE OF NUCLEAR REGULATORY RESEARCH

QUARTERLY PROGRESS REPORT
JULY 1 — SEPTEMBER 30, 1983

Herbert J.C. Kouts, Department Chairman
Walter Y. Kato, Deputy Chairman

Principal Investigators:

R.A. Bari
R.J. Cerbone
T. Ginsberg
G.A. Greene
J.G. Guppy
R.E. Hall
W.J. Luckas, Jr.
M. Reich
P. Saha
C. Sastre
J.R. Weeks
W. Wulff
D. van Rooyen

Compiled by: Allen J. Weiss
Manuscript Completed December 1983

DEPARTMENT OF NUCLEAR ENERGY
BROOKHAVEN NATIONAL LABORATORY, ASSOCIATED UNIVERSITIES, INC.
UPTON, NEW YORK 11973

Prepared for the
OFFICE OF NUCLEAR REGULATORY RESEARCH
U.S. NUCLEAR REGULATORY COMMISSION
CONTRACT NO. DE-AC02-76CH00016
FIN NOS. A-3011,-3014,-3015,-3016,-3024,-3041,-3208,-3215,-3219,-3225,-3226,-3227,-3257,-3260

Available from
GPO Sales Program
Division of Technical Information and Document Control
U.S. Nuclear Regulatory Commission
Washington, D.C. 20555
and
National Technical Information Service
Springfield, Virginia 22161

FOREWORD

The Advanced and Water Reactor Safety Research Programs Quarterly Progress Reports have been combined and are included in this report entitled, "Safety Research Programs Sponsored by the Office of Nuclear Regulatory Research - Quarterly Progress Report." This progress report will describe current activities and technical progress in the programs at Brookhaven National Laboratory sponsored by the Division of Accident Evaluation, Division of Engineering Technology, and Division of Facility Operations of the U. S. Nuclear Regulatory Commission, Office of Nuclear Regulatory Research.

The projects reported are the following: HTGR Safety Evaluation, SSC Development, Validation and Application, CRBR Balance of Plant Modeling, Thermal-Hydraulic Reactor Safety Experiments, LWR Plant Analyzer Development, LWR Code Assessment and Application, Thermal Reactor Code Development (RAMONA-3B); Stress Corrosion Cracking of PWR Steam Generator Tubing, Bolting Failure Analysis, Probability Based Load Combinations for Design of Category I Structures, Mechanical Piping Benchmark Problems; Human Error Data for Nuclear Power Plant Safety-Related Events, and Human Factors in Nuclear Power Plant Safeguards. The previous reports have covered the period October 1, 1976 through June 30, 1983.

TABLE OF CONTENTS

TABLE OF CONTENTS (Cont'd.)

TABLE OF CONTENTS (Cont'd.)

FIGURES

FIGURES (Cont'd.)

FIGURES (Cont'd.)

FIGURES (Cont'd.)

FIGURES (Cont'd.)

TABLES

I. DIVISION OF ACCIDENT EVALUATION

SUMMARY

HTGR Safety Evaluation

Stackpole 2020 medium sized samples (3 inches ϕ x 6 inches long) were removed from HIL #1 for weight change measurements after 3023 hours. Average weight loss was 0.00053 W%/hr for the four samples, which is about four times slower than the one from small samples (1/2 inches ϕ), assuming a linear relationship between oxidant content and oxidation rate.

The cross sections of the 2020 graphites oxidized in different atmospheres were examined with SEM. It seems that CO_2 atmospheres usually do not cause pittings but attack the binder phase rather uniformly. H_2O atmospheres without H_2 added caused some pittings, but the oxidation depth is somewhat shallow, i.e., center of a specimen is usually intact. Adding H_2 to H_2O atmosphere causes more pittings on the inside and outside surfaces. This effort will continue to study as many specimens as possible.

A high temperature system utilizing a high frequency generator has been built, and the maximum operating temperature is $\sim$2100°C. Preliminary runs with Ag showed that temperature gradient and homogeneous nucleation temperature are the major factors determining the particle size of the aerosols.

The review and summary of the LCS performance assessment has been completed. All conclusions arrived at in the previous work (Siting Study) remain unchanged. The report is currently being circulated as a draft and is expected to be issued shortly.

The independent core and PCRV thermal analysis code for UCHA transients (THATCH Code) is now operational in its first version and has been applied to some sample transients with operating LCS. The further required improvements are currently in progress.

SSC Development, Validation and Application

The Super System Code (SSC) Development, Validation and Application Program encompasses a series of three computer codes: (1) SSC-L for system transients in loop-type LMFBRs; (2) SSC-P for system transients in pool-type LMFBRs, and (3) SSC-S for long term shutdown transients. In addition to these code development and application efforts, validation of these codes is an ongoing task.

Under SSC-L activities, a two-dimensional, transient model to account for intra-assembly heat and flow redistribution effects was developed. This work is part of a larger effort to include improved representation of interassembly

heat transfer effects under low flow conditions. Comparison of computed results to experimental data has been good. In another SSC-L related area, assistance was given to a German engineer visiting BNL to include modeling of special design features of the KNK-II reactor. These special models included: 1) an air blast, dump heat exchanger in the secondary loop which removes decay heat following steam generator isolation, and 2) control valves in the primary and intermediate loops, which adjust the sodium flow rates after scram to maintain fairly constant loop temperatures.

Work continued on SSC-P to make it compatible with the latest version of the base program library, so as to take advantage of many improvements made under SSC-L development. Also, modeling of certain reactivity feedback effects was modified in order to provide improved simulation of a series of reactivity transients to be performed in the near future on the EBR-II reactor plant (a cold-pool type design).

Effort under SSC-S activities continued to focus on improved modeling for the upper plenum. Further testing of the two-dimensional transient model was accomplished. A preliminary report is being written.

Code validation was conducted by generating pre-test calculations using the recently revised reactivity modeling in order to make eventual comparisons to experimental data from a series of tests to be run at the EBR-II facility. Some of these tests will involve pump coastdowns without reactor scram. Furthermore, additional validation work was accomplished in several areas, including: one-dimensional upper plenum model, IHX inlet plenum thermal masses, and FFTF long term post-test analysis.

CRBR Balance of Plant Modeling

The Balance of Plant (BOP) Modeling Program deals with the development of safety analysis tools for system simulation of nuclear power plants. It provides for the development and validation of models to represent and link together BOP components (e.g., steam generator components, feedwater heaters, turbine/generator, condensers) that are generic to all types of nuclear power plants. This system transient analysis package is designated MINET to reflect the generality of the models and methods, which are based on a momentum integral network method. The code is to be fast-running and capable of operating as a self-standing code or to be easily interfaced to other system codes.

Testing of the recent, major restructuring efforts for the self-standing version of the MINET code is being conducted. Additional fluids and material properties have been included and the range of steam table application extended to allow operation at low condenser pressures. An extension to allow representation of cross-flow heat exchangers has been added. A turbine stage model is currently being incorporated into MINET. Since the initialization of heat exchangers can be intricate (particularly when one or both fluids pass through multiple heat transfer regimes), several trial iteration schemes were checked before selecting the best one for these purposes.

The MINET code is designed to be easily interfaced to existing systems codes. For example, the initial version of MINET is interfaced to the LMFBR system transient code, SSC. Here MINET provides the steam generator representation as well as the balance of plant. Efforts are now underway to interface MINET with the BWR system code, RAMONA, to provide it with a BOP and certain other auxiliary systems capability for water reactor applications.

Under MINET code validation activities, a report summarizing the comparisons with experimental data from a coastdown to natural circulation test conducted at the EBR-II facility was completed.

Thermal-Hydraulic Reactor Safety Experiments

It is shown that the particle bed heat removal rates observed in the BNL top-flood experiments agree reasonably well with the predictions based upon the latest version of the Lipinski (1983) model for particle size ranges of 0.89 mm to 12.7 mm. Calculations performed using the debris bed quench model suggest that, depending upon the particle size and the decay heat level, remelting of the debris during the quench process in the yet unquenched regions of the bed is possible.

Selected results from debris bed quenching experiments with bottom injection of the coolant are presented. The results show that the heat removal rate is a strong function of the water injection rate. At low coolant injection rates, a quench front is observed to propagate upwards within the bed at a constant speed.

Liquid metal-liquid coolant film boiling experiments performed to date have been observed to fall into two distinct regimes. In one case, the film boiling is stable and the liquid metal/vapor interface is flat and smooth. On the other hand, the second class of experiments shows an agitated liquid metal interface with the metal splashing upwards into the coolant layer as much as several centimeters. The resulting heat transfer rates in this case were observed to be three to five times higher than those predicted by the Berenson film boiling model.

LWR Plant Analyzer Development

The LWR Plant Analyzer Program is being conducted to develop an engineering plant analyzer capable of performing accurate, real-time and faster than real-time simulations of plant transients and Small Break Loss of Coolant Accidents (SBLOCAs) in LWR power plants. The first program phase was carried out earlier to establish the feasibility of achieving faster than real-time simulations and faster than main-frame, general-purpose computer (CDC-7600) simulations through the use of modern, interactive, high-speed, special-purpose minicomputers, which are specifically designed for interactive time-critical systems simulations. It has been successfully demonstrated that special-purpose minicomputers can compete with, and outperform, main-frame

computers in reactor simulations. The current program phase is being carried out to provide a complete BWR simulating capability, including on-line, multi-color graphics display of safety-related parameters.

The results of the program are important primarily for reactor safety analyses, but also for on-line plant monitoring and accident diagnosis, for accident mitigation, further for developing operator training programs, and for assessing and improving existing and future training simulators. Major assets of the simulator under development are its extremely low cost, unsurpassed convenience of operation and high speed of simulation. Major achievements of the program are summarized below.

Existing simulator capabilities and limitations regarding their representation of the Nuclear Steam Supply System have been assessed previously. Current simulators have been found to be limited to steady-state simulations and to restricted quasi-steady transients within the range of normal operating conditions.

A special-purpose, high-speed peripheral processor had been selected earlier, which is specifically designed for efficient systems simulations at real-time or faster computing speeds. The processor is the AD10 from Applied Dynamics International (ADI) of Ann Arbor, Michigan. A PDP-11/34 Minicomputer serves as the host computer to program and control the AD10 peripheral processor. Both the host computer and the peripheral processor have been operating at BNL since March 15, 1982.

An existing model for nonequilibrium, nonhomogeneous two-phase flow in a specific BWR hydraulics system has been implemented on the AD10 processor for the purpose of comparing the computing speed and accuracy of the AD10, executing the code called HIPA-PB2 for High-Speed Interactive Plant Analysis of the Peach Bottom-2 BWR power plant. The implementation of HIPA-PB2 has been carried out in the high-level language MPS-10 of the AD10.

It has been demonstrated during the last quarter of 1982 that the AD10 special-purpose peripheral processor can produce accurate simulations of BWR design base transients at computing speeds ten times faster than real-time and 110 times faster than the CDC-7600 main-frame computer carrying out the same simulation.

After the successful completion of the feasibility demonstration, work has continued to expand the hydraulics simulation used for that demonstration to produce the capability of simulating the entire Nuclear Steam Supply System as well as the flow of the working medium through turbines, condensers and feedwater trains.

Models have been developed and implemented for point neutron kinetics with five feedback mechanisms and seven scram trip initiations, for thermal conduction in fuel elements, for steam line dynamics capable of simulating acoustical effects from sudden valve actions, for turbines, condensers, feedwater preheaters and feedwater pumps, and for emergency coolant injection systems.

The software systems of both the PDP-11/34 host computer and the AD10 special-purpose peripheral processor have been upgraded to achieve greater computing speed and a larger number of analog input/output channels. Two AD10s are coupled via a direct bus-to-bus interface to compute in parallel.

During the current reporting period, models have been developed, scaled and implemented for the feedwater controller, the pressure regulator and the recirculation flow controller. Twenty-eight parameters for initiating control systems and valve failures and for selecting set points can now be changed on-line from a 32-channel control panel. Sixteen dedicated analog output lines are provided for the simultaneous display of 5 selected parameters. All input-output channels are addressed approximately 200 times per second.

Work has continued to develop a set of 60 blank diagrams with labelled axis for multicolor displays of selected parameters as functions of time, via the IBM personal computer. The IBM personal computer, however, has been found to be too slow for real-time display from the AD10.

The interest in the Plant Analyzer Development Program continues to be high, both in domestic and foreign institutions. Seven presentations were given with demonstrations, and an invited paper was presented during the current reporting period.

LWR Code Assessment and Application

Since no new versions of TRAC or RELAP5 codes have been released recently, more emphasis has been placed on the code applications area. Significant progress has been made in both the Westinghouse RESAR-3S large break LOCA and the BWR/4 MSIV closure ATWS studies. In addition, a RAMONA-3B nodalization study of the Peach Bottom 2 Turbine Trip Test 3 has been completed.

A best estimate TRAC-PD2 input deck has been developed for the Westinghouse RESAR-3S plant by simplifying the LANL VESSEL module and incorporating it into the INEL deck. The same input deck has then been used to perform two large break LOCA calculations using the TRAC-PD2/MOD1 code with several updates. The first calculation used the best estimate initial and boundary conditions, whereas the second calculation used the licensing type or Westinghouse-specified initial and boundary conditions. In the best estimate calculation, the peak cladding temperature was approximately 806°K and it occurred during the blowdown stage. The second calculation has been run up to $\sim$ 28 seconds, and so far the maximum clad temperature has been $\sim$ 1000°K. However, this calculation is being continued and the peak clad temperature is expected to be greater than 1000°K.

A preliminary BWR/4 MSIV closure ATWS calculation has been performed up to 200 seconds using the TRAC-BD1 code with its automatic control system, and the results look reasonable. A RAMONA-3B calculation has also been run for the same transient. Both of these calculations show the same general trend for the global parameters such as pressure, reactor power, steam discharge

rate, etc. However, RAMONA-3B calculation does indicate a significant variation in the axial power distribution during the transient, which cannot be calculated with a point-kinetics code such as TRAC-BD1. Finally, another TRAC-BD1 calculation using the RAMONA-3B reactor power and the same boundary conditions has been run up to 20 seconds. This last calculation showed that RAMONA-3B's thermal-hydraulic response is quite close to that of TRAC-BD1 for an ATWS-type event.

Thermal Reactor Code Development (RAMONA-3B)

During this reporting period, a collapsed water level tracking capability has been added to the RAMONA-3B code and significant progress has been made in implementing the feedwater and recirculation flow control systems. The work on collapsing 3-D cross sections for 1-D calculations and reactivity edits, under subcontract to Scandpower (ScP), is nearly completed.

1. HTGR Safety Evaluation

1.1 Graphite and Ceramics (B. S. Lee, J. H. Heiser, III, C. C. Finfrock, J. J. Barry and D. R. Wales)

1.1.1 Long Term Oxidation Experiments

Stackpole 2020 medium sized samples (3 inches ϕ x 6 inches long) were removed from HIL #1 for weight change measurements after 3023 hours. Average weight loss was 0.00053 W%/hr for the four samples, which is about four times slower than the one from small samples (1/2 inches ϕ) assuming a linear relationship between oxidant content and oxidation rate.

We are planning to modernize the existing HIL #1 and HIL #2 under construction. As a part of an effort to cope with the reduced manpower, a data acquisition system will be added, and the BNL computer will be utilized for data processing.

The HIL #1 and #2 are essentially identical, and the schematic drawing of the loop is shown in Figure 1.1.1.

1.1.2 Strength Loss of Graphite by Oxidation

Since we completed the oxidation experiments that had been generating strength loss data for several grades of graphite in different atmospheres, we have been analyzing the strength data and examining the oxidation morphologies to get insights on the mechanism(s) for oxidation induced strength loss. We are planning to examine as many cross sections of the oxidized specimens as possible, because a statistical approach is a must due to the inhomogeneity of graphite in impurities distribution, pore structure and so on.

The strength loss of graphite by oxidation is a complicated process in which many variables are involved as illustated in Figure 1.1.2. The degree of strength loss is determined by oxidation mode, oxidation rate, total burnoff and oxidation morphology. From the oxidation experiments, we generated oxidation rate data, and from the mechanical testings we obtained relationships between burnoff and strength loss. The examination of the surface and cross section of the oxidized specimen provides information on oxidation mode and morphology.

Previously, PGX graphite was studied (M. Eto and F. B. Growcock, 1981) and the results are summarized below for comparison. This quarter 2020 graphite was mainly studied, and some of the results are given.

a. PGX Graphite (Union Carbide, U.S.A)

The decrease in both compressive stength and tensile strength due to oxidation at a given total burnoff is greater when the oxidation is carried out in O_2 than in H_2O/He or CO_2/He. The substantial enhancement of the strength loss by O_2 at a given burnoff suggests that changes in the microstructure of PGX graphite produced by oxidation in O_2 may be different than the changes created in other atmospheres.

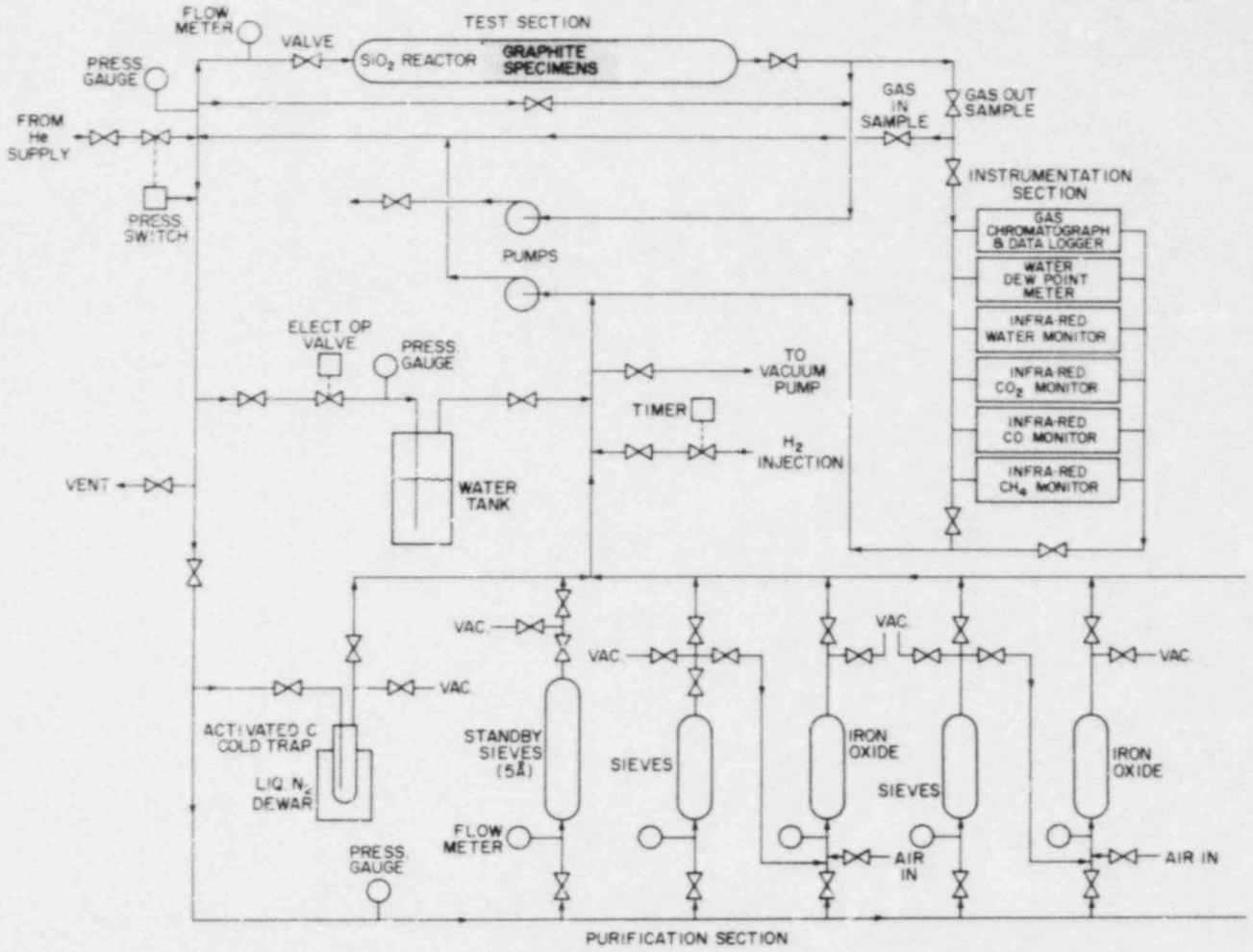

Figure 1.1.1 Schematic Diagram of HIL #1 and #2.

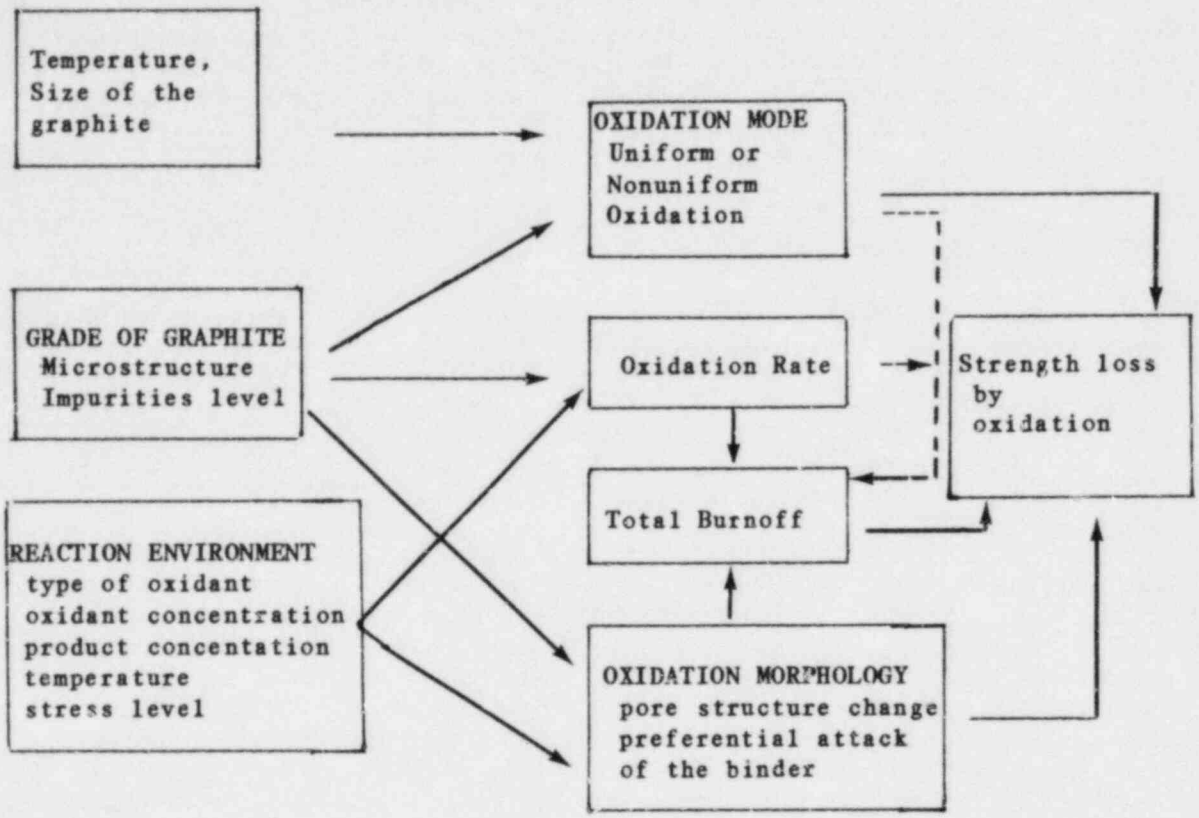

Figure 1.1.2 The Variables That Affect the Strength Loss by Oxidation.

The surface of a specimen oxidized in 2% H_2O/He at 600°C is seen to have a higher density of pits than that generated by oxidation in 2% O_2/N_2 at 500°C though the total burnoff of the former specimen was lower than that of the latter (2.77% vs. 5.05%).

X-ray maps indicated that oxidation by H_2O was localized around regions rich in iron. No clear correspondence between the distribution of iron and the surface topography was evident for O_2/N_2 oxidation.

Inspection of as-received PGX graphite surfaces by SEM and XES revealed that the impurity iron is not distributed homogeneously at all, but rather is localized in a few regions between grains, i.e., binder. Thus the proposed mechanism for strength loss may be that oxidation by H_2O would led to formation of large pits in the vicinity of iron-rich regions, whereas oxidation by O_2 primarily would led to a large number of very small pits scattered throughout the binder.

b. 2020 Graphite (Stackpole Corp., U.S.A.)

As reported in the previous quarterly (B. S. Lee et al., 1983), the major effect of adding hydrogen (10%) to a H_2O atmosphere (1%) on 2020 graphite is shown on the outer surfaces of the samples. The samples oxidized in a H_2O atmosphere (without H_2) showed little pittings on the outer surfaces, while a 1% H_2O/10% H_2 atmosphere caused severe pittings on more than half of the samples. Impurities could be detected inside the pits at higher magnification, and these were analyzed to be Ca and Fe.

The inside of the samples did not show large pits. Thus, apparently large oxidation gradient exists in these samples that show surface pitting.

The internal pore structure changes of some of the 2020 specimens oxidized in different atmospheres were studied by examining the cross sections of the specimens with SEM. This should reveal the oxidation morphology differences caused by different environments, and should give explanations for the strength test results. Once again, graphite is not a very uniform material in impurities and structure, and statistical approaches should be taken to see the trends. Therefore, it is necessary to examine as many specimens as possible.

Figures 1.1.3, 1.1.4, 1.1.5 and 1.1.6 show the typical cross sections of 2020 graphites oxidized in O_2, CO_2, H_2O and H_2O + H_2 environments, respectively.

It is too premature to draw any conclusions from these examinations, but some trends were noticed. It seems that, for 2020 graphite, CO_2 atmospheres usually do not cause pittings but attack the binder phase rather uniformly. H_2O atmospheres without H_2 added caused some pittings, but the oxidation depth is somewhat shallow, i.e., center of a specimen is usually intact. Adding H_2 to H_2O atmosphere causes more pittings on the inside and outside surface.

Deep pits are usually associated with impurities. Figure 1.1.7 shows that the distributions of different impurities are independent of each other. If we assume that active catalysts are accumulating in the pits as oxidation proceeds, probably Ca and Fe are the major catalysts.

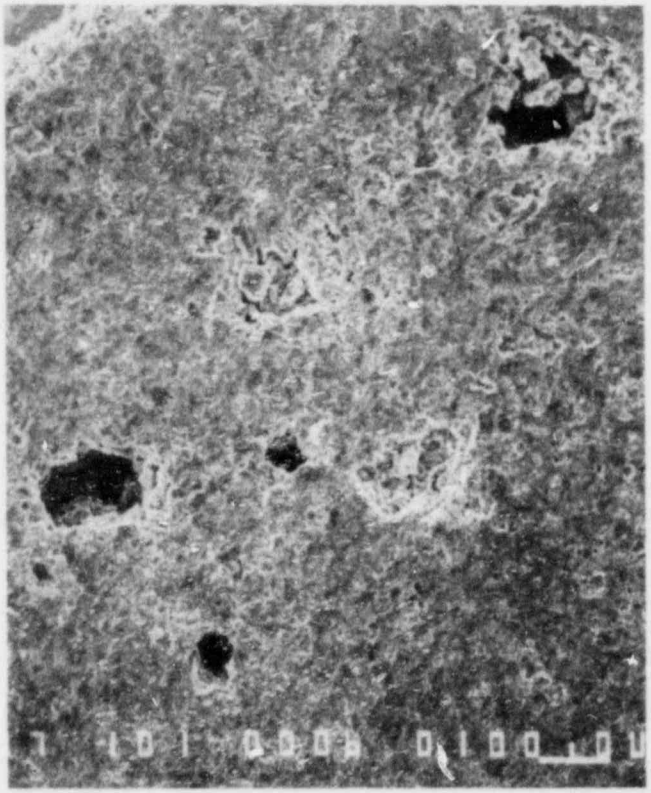

Figure 1.1.3 Cross Section of a 2020 Graphite Specimen Oxidized in 2% O_2/He at 600°C, 7.91% Burnoff (L2020,20T).

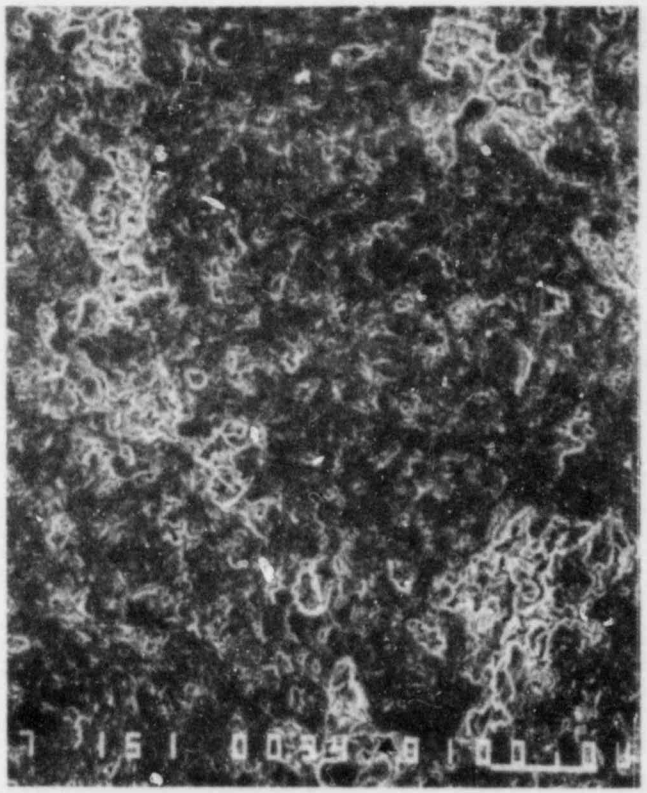

Figure 1.1.4 Cross Section of a 2020 Graphite Specimen Oxidized in 2% CO_2/He at 850°C, 5.47% Burnoff (S2020,27T).

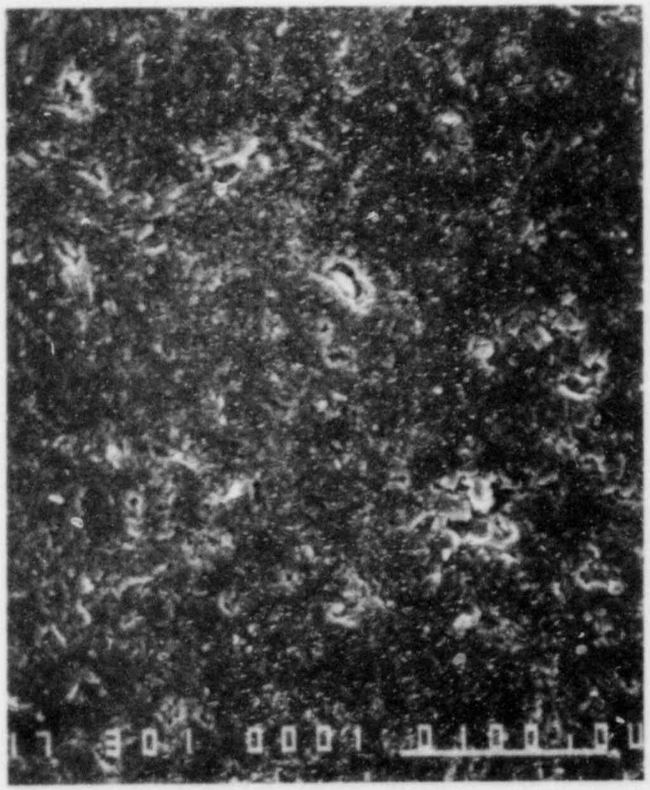

Figure 1.1.5 Cross Section of a 2020 Graphite Specimen Oxidized in 1% H_2O/He at 850°C, 7.62% Burnoff (L2020, 46T).

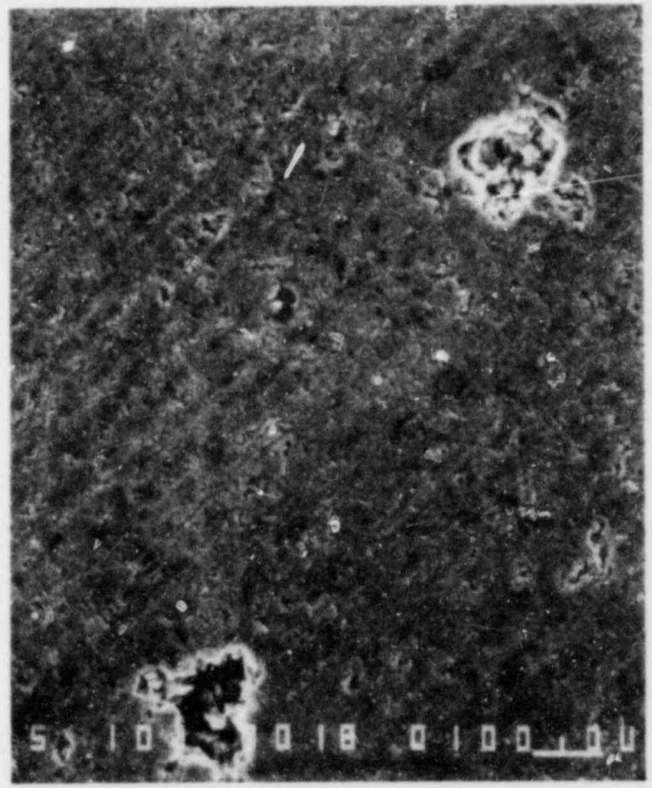

Figure 1.1.6 Cross Section of a 2020 Graphite Specimen Oxidized in 1% H_2O/He at 800°C, 6.88% Burnoff (L2020, 17C).

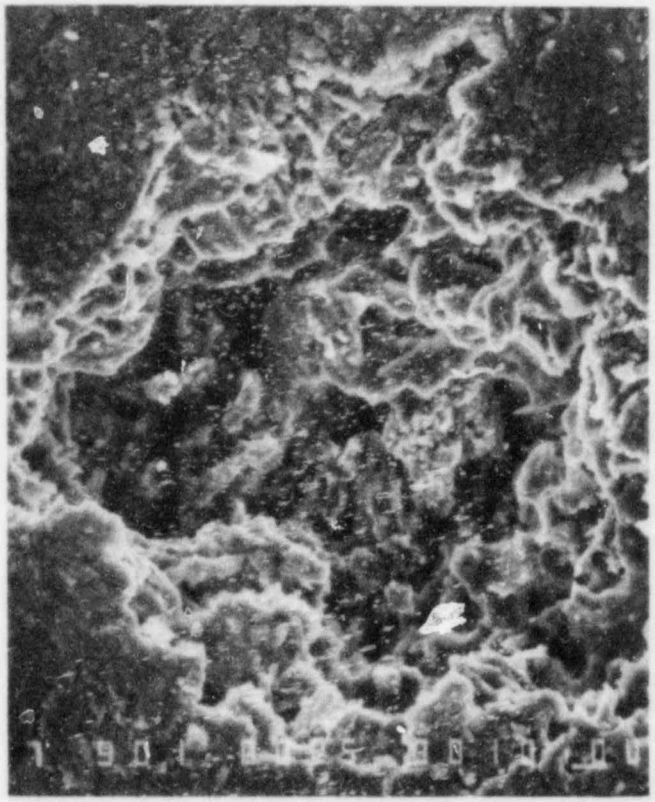

Figure 1.1.7

(a) SEM Photomicrograph of a Pit in ~2020 Specimen Oxidized in 2% O_2/He at 500°C (S2020, 20 C) Magnification 500X.

(b) Ca X-ray Dot Map from Area Shown in (a).

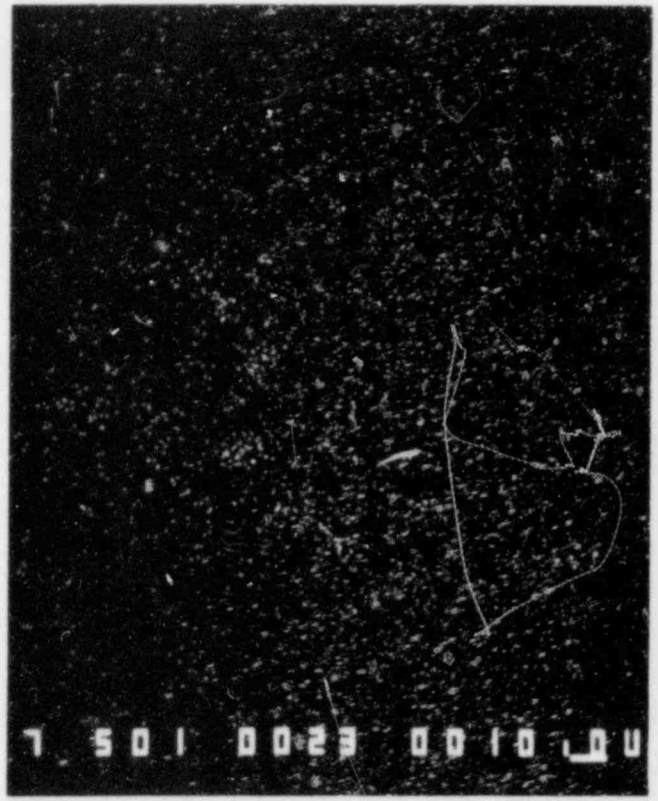

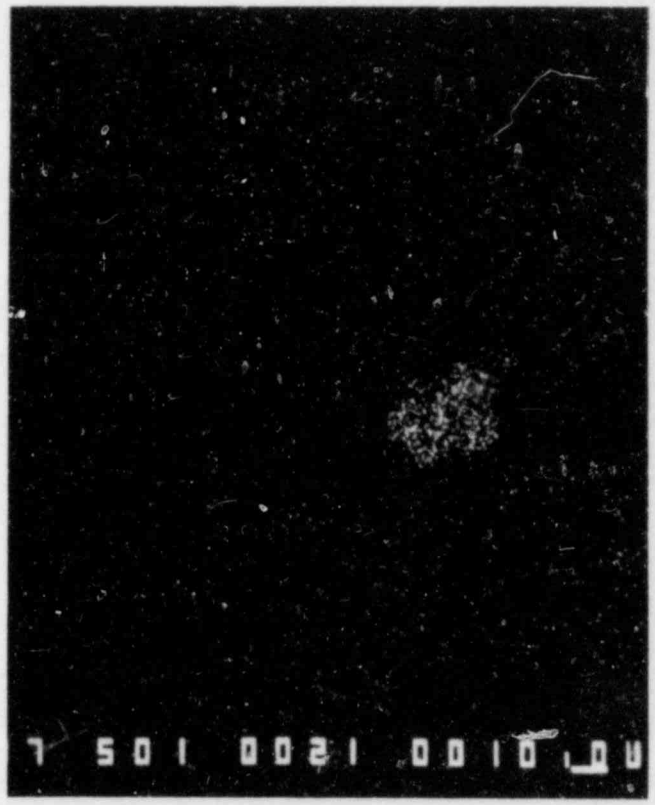

Figure 1.1.7 (Continued)

(c) Fe X-ray Dot Map from the Area Shown in (a)

(d) Ti X-ray Dot Map from the Area Shown in (a).

1.2 Fuel and Fission Product (B. S. Lee, J. H. Heiser, III, C. C. Finfrock and C. Sastre)

1.2.1 Gas Phase Fission Product Migration

This quarter, our major effort was focused on building a high temperature system to study gas phase transport of the fission products. This subject had been studied at BNL earlier (October 1, 1977 to September 30, 1982).

In order to generate the source term related data on fission product transport, we are refocusing on this subject.

The experimental results from earlier work clearly demonstrated that the formation of nuclear aerosols under certain HTGR accident conditions, by which vaporized fission products such as Ag, Sr and Ba, are transported in the gas-phase. It was also learned that, in cases of SrO and BaO, the chemical reactions of the oxide with graphite could be the controlling factor for Sr or Ba release at temperatures above 1300°C, while the release of Ag at higher temperatures is controlled either by nucleation or evaporation step. The previous work at BNL was reviewed in a recent BNL memo (B.S. Lee, 1983, Memo to File 122).

Based on the existing information and knowledge, the following works are planned. (These will be modified if necessary in the future.)

1) Expand the existing work to higher temperatures (up to 2500°C and 3000°C for system #1 and 2, respectively).

2) Ag will be studied first to get the necessary experience.

   - Different crucibles will be used for comparison; graphite and probably tungsten.
   - Nucleation step will be studied by varying the temperature gradient.
   - The effect of H_2O concentration in He will be studied.

3) For Sr and Ba study, SrO and BaO will be used directly instead of nitrates.

   - More data will be generated at higher temperatures.
   - The effect of H_2O concentration in He will be studied.

Experimental Set-up

The sources of high-frequency energy are motor-generator set, spark-gap oscillator and vacuum-tube oscillator. We have been using a motor-generator set that generates 10 kHz frequency with a maximum output of 30 KW to study migration of fission product in graphite. This apparatus has proven that it

can heat a graphite block up to 3600°C utilizing Thermax (trade name for Vanderbilt Co.) as an insulation. Thus no problem is expected in converting this system to conduct experiments to integrate the aerosol and diffusion work.

In addition to this motor-generator set, we have a vacuum-tube oscillator type high-frequency generator. The radio frequency generated from this set is in the range of 200 ~ 450 kHz which is much higher than that from the motor generator set. The output from this machine is 10KW.

At first we attempted to heat a large graphite block (3 1/4'' ϕ x 7'' L) inside an alumina tube (8'' ϕ) with thermax as an insulator in between. The maximum temperature reached was ~1500°C, and it was found that Thermax was generating heat. The reason why Thermax works as good insulating material for the other system we have (10 kHz system) while it fails to be an insulator for this high frequency system is being studied.

Thermax was replaced with zirconium oxide (ZrO_2), and the maximum temperature was reached at ~2500°C. However, the ZrO_2 was reacting with the graphite producing orange colored particles (probably some zirconium oxicarbides). Thus this plan to heat a big block with the 10KW machine was abandoned, and it was decided to go for a small system without insulation. Because the system will be clean, the measurements of the vapor pressures of some of the fission product and other materials of interest are possible in addition to the aerosol formation study.

When a 1'' ϕ x 2'' L graphite specimen was heated with a double helix solenoid coil of 40 mm ϕ (inside coil), the maximum temperature was ~2300°C. However, the softening point for fused quartz is 1670°C and the melting point is 1800°C, and heating the graphite specimen inside fused quartz tube caused formation of SiC on the surface of the graphite. Yellow fumes were also observed during the heating. Thus, it was clear that some form of cooling for the fused quartz reactor tube was necessary.

With a water jacket (O.D. 70 mm) and silver mirror on the outer surface of the inner tube, the maximum temperature reached was ~1750°C. Without the water jacket, with the same size coil as above, the maximum temperature was about the same. Thus, water or the mirror is not taking a significant amount of energy. Apparently, the distance increase between the specimen and the coil due to the water jacket is the major cause of the poor coupling.

The silver mirror (<30μin) deposited on the surface of a quartz tube was reducing radiation heat loss, but the boiling of the water inside the pores of the coating caused peeling off of the mirror after several runs.

The silver mirror was replaced with thin platinum foil (0.001 in), but because of the coupling of the platinum the actual work temperature was lower than the system without a platinum mirror.

With a water jacket only (O.D. 50 mm, without a mirror), the maximum work temperature is ~2100°C. This temperature limitation is from the low power output of the machine (10KW). However, we will attempt to change the system design drastically so that we can reach higher temperatures than 2100°C. For the time being, this system will be utilized to conduct experiments that require clean and controllable atmospheres.

Preliminary Experiments

Two preliminary runs at 1500°C and 2000°C with silver have been completed. The schematic diagram of the set-up is shown in Figure 1.2.1. The filter was purchased from Millipore Corp., and the pore size is 0.2μm.

Figure 1.2.2 shows the silver aerosol particles from the 1500°C run, and the average particle size is ~1000 Å. The particles from higher temperatures, 2000°C, were smaller (500 ~ 700 Å).

These preliminary results show that vaporization temperature and homogeneous nucleation temperature may be the major factors determining the particle size. Future study will include investigation of the effects of major parameters.

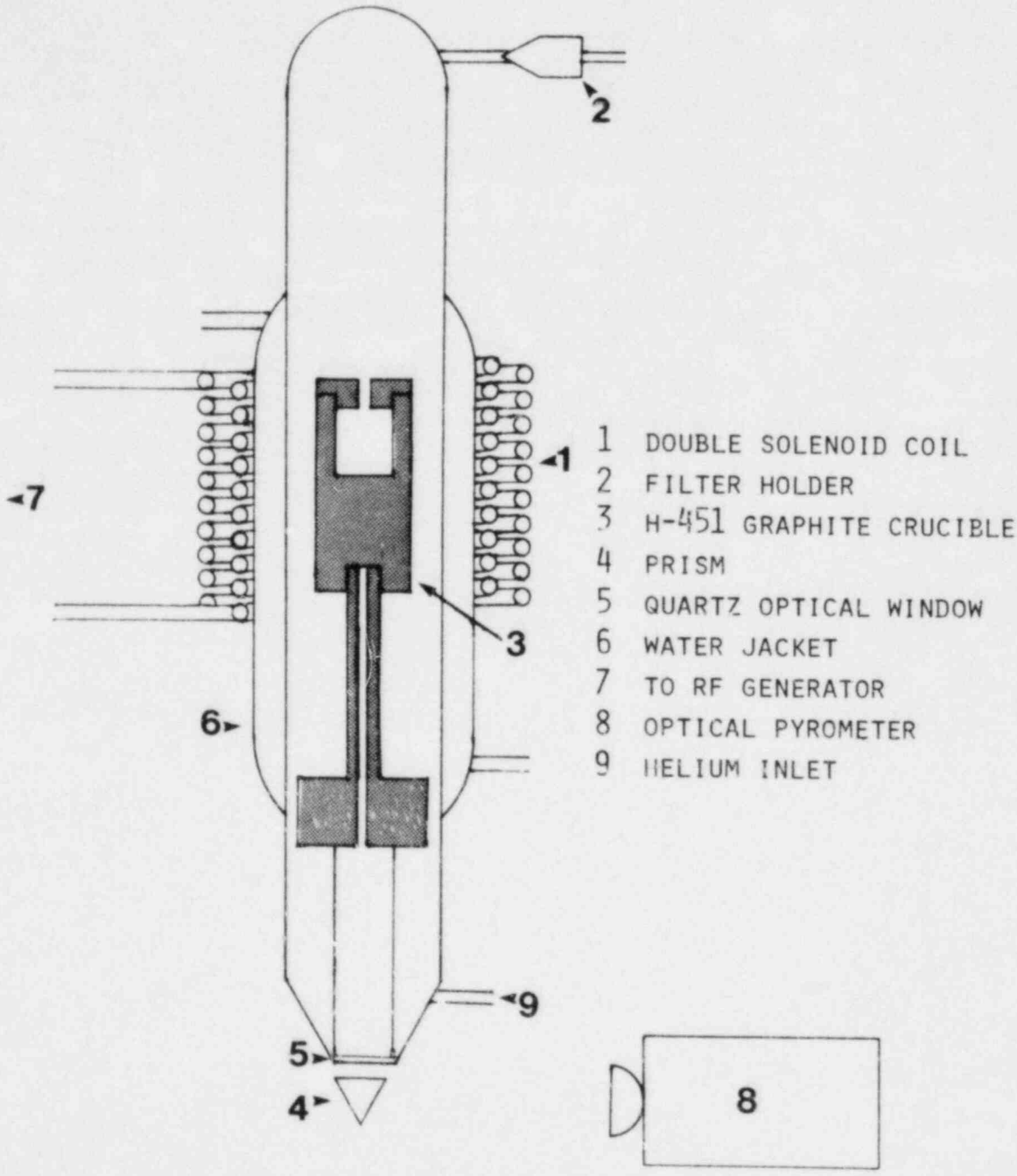

Figure 1.2.1 Schematic Drawing of High Temperature System for Aerosol Formation Study.

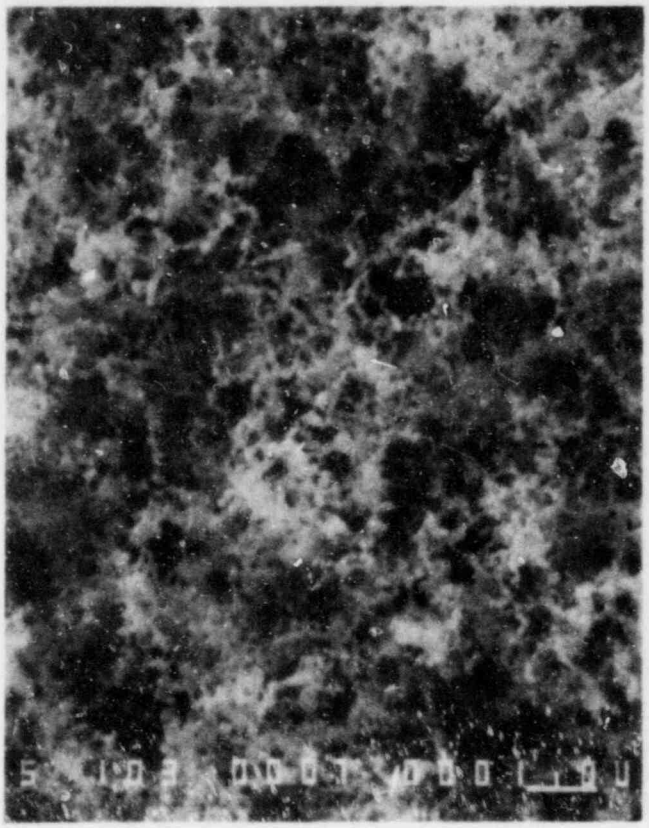

Figure 1.2.2 Silver Aerosol Particles Formed From Silver Vapor Evaporated from a H-451 Graphite Crucible Heated at 1500°C.

1.3 Analytical

1.3.1 HTGR Code Library (J. Colman)

Table 1.3.1

HTGR Code Library - Alphabetic Code Order

Program	Origin/ Code Date	BNL Status	Function
BLAST	ORNL/ACC 8/76 (BNL 1/80)	OP	A dynamic simulation of the HTGR reheater-steam generator module.
BLOOST/ BLOOST-7	GA/SAI 1/70	OP	Performs zero-dimensional reactor kinetics calculations.
CHAP-1 (Jan. 1978)	LASL 2/77	OP	Simulates the overall HTGR plant with both steady state and transient solution capabilities.
CIRC (JETS)	BNL 4/78	OP	Calculates fluid dynamics in an HTGR containment vessel following a depressurization accident.
CNTB-7	GA 7/79	OP	Analysis of Partially mixed containment atmospheres during depressurization events.

ACC = Argonne Code Center.
BAW = Babcock and Wilcox.
BNL = Brookhaven Nat. Lab.
BPNW = Battelle Pacific N.W.
GA = General Atomic.
LASL = Los Alamos Scientific Lab.
NOP = Non-Operational.
OP = Operational
ORNL = Oak Ridge National Lab.
P = Proprietary.
SAI = Science Applications, Inc.

Program	Origin/ Code Date	BNL Status	Function
CONTEMP-G (CONTEMPT-G)	GA-BAW 2/74	OP (P)	Simulates temperature-pressure response of an HTGR containment atmosphere to postulated coolant circuit depressurization.
CORCON	GA 7/74	OP (P)	Computes the temperature history and fission product redistribution following a loss of all convective cooling of the core.
CORTAP	ORNL ACC 1/77 (BNL 1/80)	OP	A coupled neutron kinetics - heat transfer program for the dynamics simulation of the HTGR core.
DECAYREM	ORNL 5/74	OP	RSIC Data Library Collection.
DIFFTA	BNL 11/75	OP	Finite element method code for Steady State Heat Conduction, Fission Product Migration and Neutron Diffusion Calculations.
ENDFB and Satellite Codes	BNL	OP	Evaluated Nuclear Data File/B and file manipulation codes.
EVAP	BNL 5/78	OP	A model for the Migration of Fission Products along the coolant channels of an HTGR following a hypothetical accident of complete loss of cooling.
EXPEM	ORNL 2/75	OP	Calculates external radiation doses.
FENG	LASL 2/77	OP	One of three codes which create or add to the reactions data library for QUIL and QUIC codes. Reactions added are of type Free Energy.
FEVER-7	GA	OP	Performs one-dimensional, diffusion theory, burnup and reload calculations.

Program	Origin/ Code Date	BNL Status	Function
FLAC	GA	OP	Calculates steady state flow distributions in arbitrary networks with heat addition.
FPPROD	BNL 3/78	OP	Performs simplified fission product production analysis.
FYSMOD	LASL 9/76	NOP	Calculates the two-dimensional solution of HTGR core blocks subjected to external motion.
GAKIT	GA 9/68	OP	Performs one-dimensional multigroup kinetics calculations with temperature feedback.
GAMBLE	GA	OP	A program for the solution of the multigroup neutron-diffusion equations in two dimensions, with arbitrary group scattering.
GGC4	GA/ACC	OP	Prepares broad thermal cross sections from the tape produced by WTFC and MAKE.
GOPTWO/ GOP-3	BPNW 6/75 BPNW 10/76	OP NOP	Graphite Oxidation Program. Analyzes the steady state graphite burnoff and the primary circuit levels of impurities.
HAZARD	BNL 3/77	OP	Analyzes gas layering and flammability in an HTGR containment vessel following a depressurization accident.
H-CON1	BNL 5/76	OP	Calculates one-dimensional heat conduction for an HTGR fuel pin by finite difference method.
HYDRA-1	BNL 5/76	OP	A program for calculating changes in enthalpy single phase liquid due to external heat source.
INREM	ORNL 2/75	OP	Calculates internal radiation doses.

Program	Origin/ Code Date	BNL Status	Function
INTERP	GA MICROX LIBRARY	OP	Prepares broad group cross sections from MICROX output data tapes.
JANAF	Dow Chemical Company 11/78	OP	JANAF Thermochemical Tables.
LARC-1	LASL 11/76	NOP	Calculates fission product release from BISO and TRISO fuel particles of an HTGR during the LOFC accident for single isotopes.
LARC-2	LASL	NOP	Similar to LARC-1; in addition, handles release from isotope chains.
LASAN-BNL LASAN-LASL	LASL/BNL 4/78	OP	A general systems analysis code consisting of a model independent systems analysis framework with steady state, transient and frequency response solution capabilities. There are two versions of the code available - the original LASL version and the converted BNL version.
LEAF	LASL 11/76	NOP	Calculates fission product release from a reactor containment building.
MAKE	SAI	OP	Prepares fine group fast cross section tape from GFE2 for spectrum codes.
NONSAP-C	LASL 10/78	NOP	Calculates static and dynamic response of three-dimensional reinforced concrete structures, in addition to creep behavior.
ORECA-1	ORNL-ACC 4/76	OP	Simulates the dynamics of HTGR cores for emergency cooling analyses. (Ft. St. Vrain)

Program	Origin/ Code Date	BNL Status	Function
ORIGEN	ORNL 4/75	OP	Solves the equation of radioactive growth and decay for large numbers of isotopes with arbitrary coupling.
ORTAP	ORNL-ACC 9/77	OP	A nuclear steam supply system simulation for the dynamic analysis of HTGR transients.
OXIDE-3	GA 1/74	OP (P)	Analyzes the transient response of the HTGR fuel and moderator to an oxidizing environment.
POKE	GA 7/70	OP (P)	Calculates steady state 1-D flow distributions and fuel and coolant temperatures in a gas cooled reactor.
PREPRO	GA	OP (P)	Prepares input data and source code revisions for RECA code.
PRINT	SAI	OP	Reads the fast cross section tape produced by MAKE.
QUIC	LASL 2/77	OP	Solves complex equilibrium distribution in chemical environments.
QUIL	LASL 2/77	OP	Solves complex equilibrium distribution in chemical environments.
RATE	LASL 7/78	OP	One of three codes which create or add to the reactions data library for QUIL and QUIC codes. Reactions added are of type Rate.
RATSAM-6	GA 5/77	OP	Analyses the transient behavior of the HTGR primary coolant system during accidents.
RECA	GA 8/70	NOP (P)	Calculates time dependent flow distributions and fuel and coolent temperatures in the primary system.
RICE	LASL 3/75	OP	Solves transient Navier-Stokes equations in chemically reactive flows.

Program	Origin/ Code Date	BNL Status	Function
SODEMME	BNL 8/77	OP	Calculates transient thermal hydraulic aspects of circulating gas systems.
SOLGASMIX	ORNL 4/77	OP	Calculates equilibrium relationships in complex chemical systems.
SORS	GA 4/74	OP (P)	
SORSD	GA	OP (P)	Computes the release of volatile fission products from an HTGR core during thermal transients.
SORSG	GA	OP (P)	Computes the release of non-volatile gaseous fission products from an HTGR core during thermal transients.
SPRINT	GA/SAI	OP	Reads the thermal cross section tape produced by WTFG.
SURF	LASL 2/77	OP	One of three codes which create or add to the reactions data library for QUIL and QUIC codes. Reactions added are of type Surface.
SUVIUS	LASL	NOP	Solves the behavior of fission gases in the primary coolant of a gas-cooled reactor.
TAC2D	GA 9/69	OP	Performs two-dimensional, transient conduction analyses.
TAP	GA	OP (P)	Calculates the transient behavior of the integrated HTGR power plant.
TEMCO/TEMCO7	GA	OP	Computes reactor temperature coefficients from input cross section data.

Program	Origin/ Code Date	BNL Status	Function
THGRAF	BNL 11/77	OP	Calculates position and velocity of the thermo-chromatograph as a function of time for various models.
WTFG	GA	OP	Prepares fine group thermal cross section tape from GAND2 or FLANGE for spectrum codes.
1-DX		OP	Performs one-dimensional, diffusion theory, steady state calculations.

1.3.2 Liner Cooling System Performance under Accident Conditions (P. G. Kroeger)

The review and revision of the liner cooling system (LCS) performance assessment was completed, including an evaluation of the flow reductions to be anticipated as boiling may occur in some tubes under transient peak heat fluxes subsequent to thermal barrier failures. Figures 1.3.1 and 1.3.2 show some typical results of our assessment. Figure 1.3.1 gives the peak heat fluxes (per square foot of liner outside surface) that can be accomodated at the side barrel for specific exit qualities. Figure 1.3.2 gives the resulting flow reductions. Both results are given for two potential designs of 125 ft or 250 ft tube lengths for each of the parallel tube passes.

None of the previously arrived at conclusions, (Appendix F, Siting Study) were affected by the current review, except that the current work more clearly establishes the conservatism used in our work and thus provides an even firmer base for this work. The results are given in detail in an informal report (BNL-NUREG-33073) which is currently being circulated in draft form and is expected to be published in November 1983.

1.3.3 Primary Loop Thermal Analysis under UCHA Conditions (P. G. Kroeger and J. Colman)

The independent core and primary loop thermal analysis code for UCHA scenarios (THATCH code) has been fully debugged and was applied successfully to several test transients, comparing it to previous results obtained with the CORCON code, to demonstrate that equivalent results can be obtained, and to establish confidence in our models. In these test applications with operating LCS the code was applied as closely as possible to previous CORCON runs, using an almost identical nodalization, the same time steps, and the same material property and decay heat functions. Under these conditions many of its improved modeling capabilities could not be utilized, and the resulting differences were predominantly due to a more accurate treatment of temperature dependent properties at boundaries, in particular at the thermal barrier.

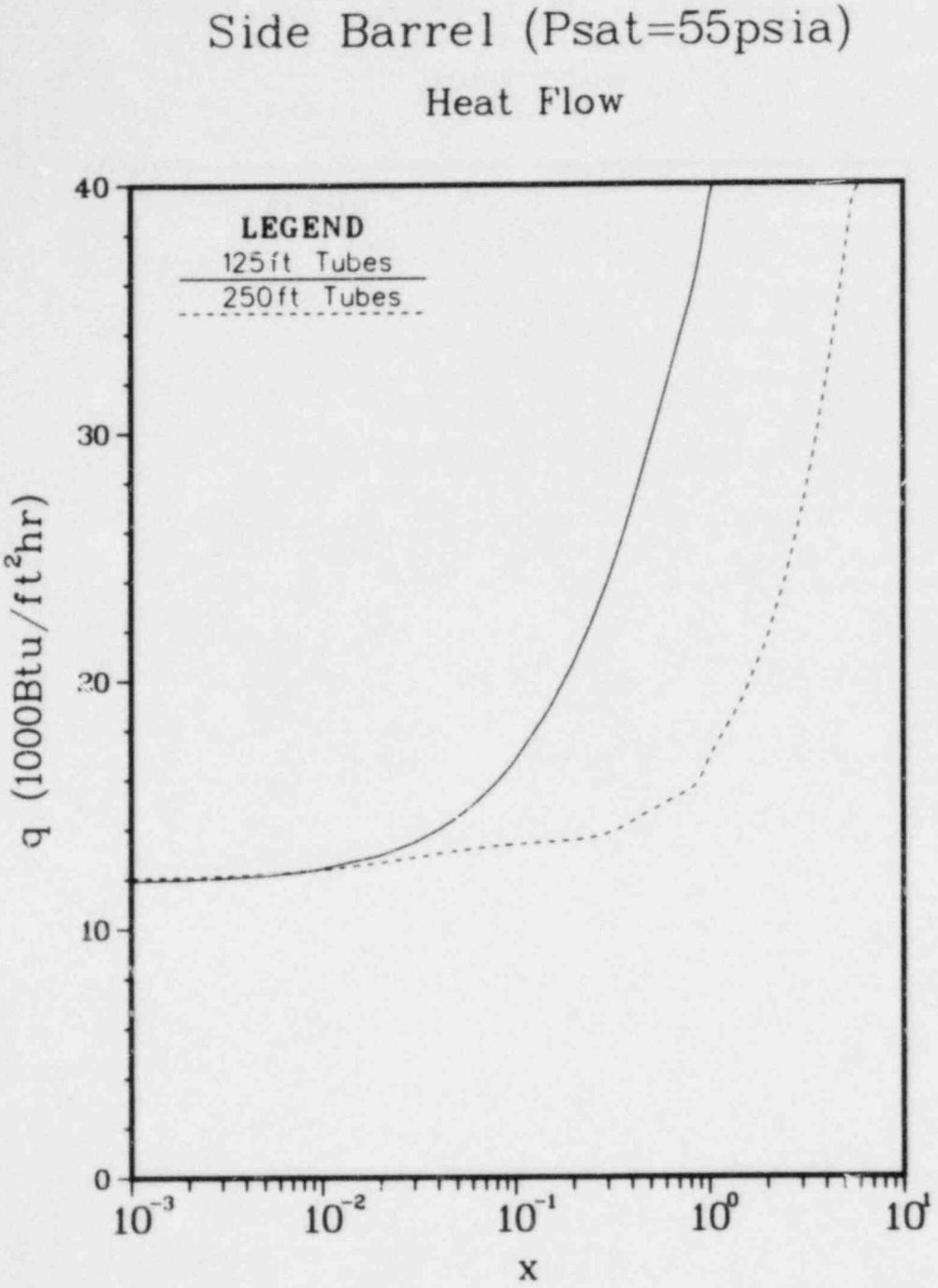

Figure 1.3.1 Side Barrel Tube to Coolant Heat Load per Square Foot of Liner Surface as Function of Coolant Exit Quality (results beyond x=1 are extrapolations and should not be used beyond $x \approx 1.2$).

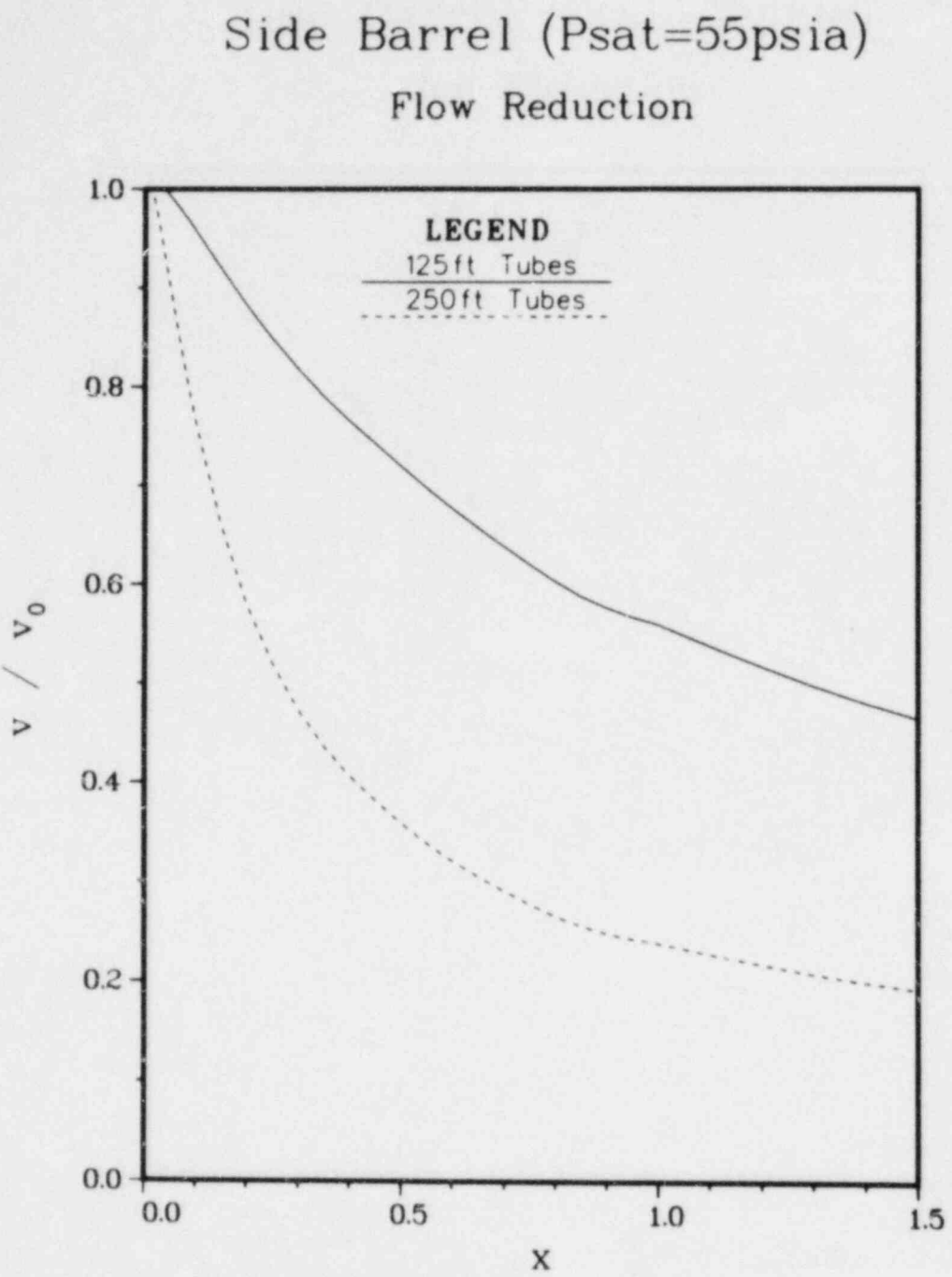

Figure 1.3.2 Coolant Flow Reductions at Side Barrel as Function of Coolant Exit Quality (results beyond x=1 are extrapolations and should not be used beyond x ≈1.2).

In these comparisons the peak core temperatures of the THATCH predictions ran about 50°F higher than those of the CORCON predictions, and the thermal coverplate temperatures in the upper plenum were about 30°F lower resulting in slightly less or later thermal barrier failures.

With this check against CORCON as well as with numerious other debug checks, we are now certain that the code can model thermal transients of the core and PCRV accurately. It will be applied in all future UCHA modeling requirements.

Its primary advantages at this time are improved plena radiation computations, better side shield and thermal barrier models and greater flexibility in changing material property and decay heat functions, with complete control and knowledge over all phases of the code. Various input and output options significantly ease its application. A preliminary documentation for the input requirements has been drafted.

Currently coverplate failure modeling is being added, and we are proceeding to include improved material property routines, providing options for best estimates is conservative data. Concrete water migration, melting and spalling of components and decay heat redistribution will be added thereafter to complete the code, resulting in significantly improved capabilities for the analysis of UCHA core and PCRV thermal transients.

1.3.4 Containment Atmosphere Response (P. G. Kroeger)

A report reviewing previous containment atmosphere response work and assessing the potential for more remote combustion scenarios in the Base Line Zero 2240 MWth design as well as in the Fort St. Vrain reactor is currently being drafted.

REFERENCES

KROEGER, P. G., COLMAN, J, HSU, C. J. and ARAJ, K., Appendix F, Siting Study, ''Thermal Analysis of Core Heatup Accidents,'' Brookhaven National Laboratory, 1983.

KROEGER, P. G., ''Assessment of HTGR Liner Cooling System Performance under Accident Conditions,'' Brookhaven National Laboratory, BNL-NUREG-33073, February 1983.

CABLE, J.W., Induction and Dielectric Heating , p. 19, Reinhold Publishing Co., N.Y. 1954.

ETO, M. and GROWCOCK F.B., ''Effect of Oxidizing Environment on the Strength and Oxidation Kinetics of HTGR Graphites,'' BNL-NUREG-51493, Sept. 1981.

LEE, B. S., HEISER, J. H., III, FINFROCK, C. C., BARRY, J. J., and WALES, D. R., Quarterly Progress Report, BNL-NUREG-2331, April - June 1983

2. SSC Development, Validation and Application (J.G. Guppy)

The Super System Code (SSC) Development, Validation and Application Program deals with advanced thermohydraulic codes to simulate transients in LMFBRs. During this reporting period, work continued on three codes in the SSC series. These codes are: (1) SSC-L for simulating short-term transients in loop-type LMFBRs; (2) SSC-P which is analogous to SSC-L except that it is applicable to pool-type designs and (3) SSC-S for long-term (shutdown) transients occurring in either loop- or pool-type LMFBRs. In addition to these code development and application efforts, validation of these codes is an on-going task. Reference is made to the previous quarterly progress report (Guppy, 1983a) for a summary of accomplishments prior to the start of the current period.

2.1 SSC-L Code (M. Khatib-Rahbar)

2.1.1 Intra-Subassembly Heat and Flow Redistribution (M. Khatib-Rahbar, E. G. Cazzoli)

A transient model based upon the previously developed parabolic flow model has been developed. The model solves the equations of

Continuity

$$\frac{\partial(\rho u)}{\partial x} + \frac{\partial(\rho v)}{\partial y} = 0 \tag{2.1}$$

Energy

$$\frac{\partial T}{\partial t} + u \frac{\partial T}{\partial x} + v \frac{\partial T}{\partial y} = \alpha_e \frac{\partial^2 T}{\partial y^2} + \frac{Q\ (x,y)}{\rho c_p} \tag{2.2}$$

and

Axial Momentum

$$\frac{\partial u}{\partial t} + u \frac{\partial u}{\partial x} + v \frac{\partial u}{\partial y} = -\frac{1}{\rho} \frac{\partial P}{\partial x} - g \frac{\rho^*}{\rho} [1 - \beta (T - T^*)] + \frac{f}{2D_e \lambda^2} u^2 + \nu \frac{\partial^2 u}{\partial y^2} \tag{2.3}$$

together with the energy equations for the duct walls and interstitial sodium.

Numerically, the spatial differencing is identical to the earlier steady-state parabolic method; however an implicit time differencing procedure is adopted.

The code has been applied to the Westinghouse 61-rod pin bundle experiments and good agreement is observed for both an undercooling and an overcooling event. Figures 2.1 through 2.3 show the transient power, flow and subsequent power-to-flow ratio as measured in test run 613. Figures 2.4 through 2.6 illustrate the comparison between calculated and measured transverse coolant temperature profiles at various times into the transient.

Figure 2.7 shows the comparison between measured and calculated sodium temperatures corresponding to thermocouple locations 230 and 324 in the bundle. Again, excellent agreement between the model predictions and test data is demonstrated.

A detailed report describing various models and numerical techniques that have been developed is being prepared. The code input and user's manual also will be included.

2.1.2 Modeling of German KNK-II Reactor System (B. Schubert, GKSS/Germany, M. Khatib-Rahbar, R.J. Kennett)

As part of its work for LMFBR safety analysis, the GKSS-Forschungszentrum Geesthacht (Germany) plans the calculation of natural circulation transients for the German reactor KNK-II using SSC (Guppy, et al., 1983b). Special features of this reactor system include: 1) a Dump Heat Exchanger (DHX) in the secondary loop, which removes the decay heat after reactor scram and 2) control valves in both primary and secondary loops, which control the sodium flow rates under natural circulation conditions to keep loop temperatures constant and to prevent the structures against thermal shocks. These features are also being discussed or partly used for other reactors, such as the SNR-300 or Superphenix II. Figure 2.8 shows schematically the KNK-II reactor plant. If scram occurs, all pumps are tripped and the DHX flaps open. At the same time, controllers and their associated control valves are activated. The steam generator is bypassed on the sodium side. The DHX sodium outlet temperature is controlled to a constant pre-scram value by adjusting the air flow rate (KNK-II, 1977). Because the present SSC version cannot simulate these KNK-II plant specific DHX and associated controls, models have been separately developed and are discussed here.

2.1.2.1 Heat Exchanger Model

The heat exchanger configuration used in the model is shown in Figure 2.9. The heat exchanger is of the single pass, cross-flow design using finned tubes. Heat can be removed by either natural or forced convection. Since the sodium outlet temperature has to remain approximately constant, the air flow rate is controlled: 1) by flaps and/or adjustable blade angle, keeping the fan speed constant or 2) by variable fan speed, keeping the blade angle constant.

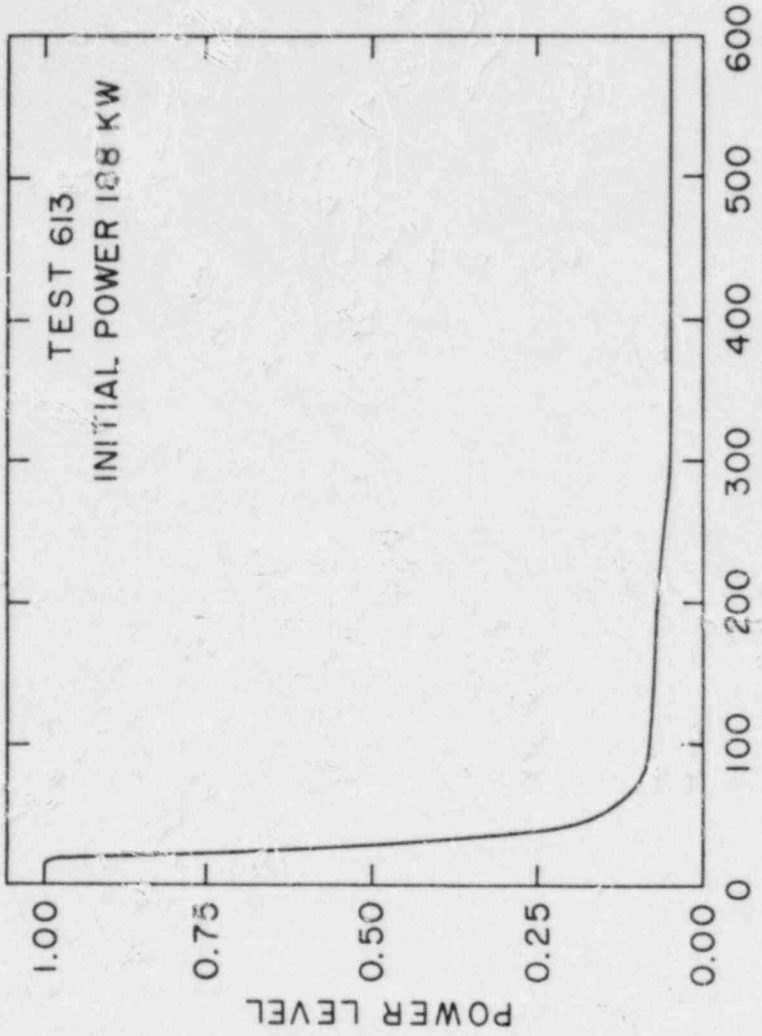

Figure 2.1 Test Section Power Level

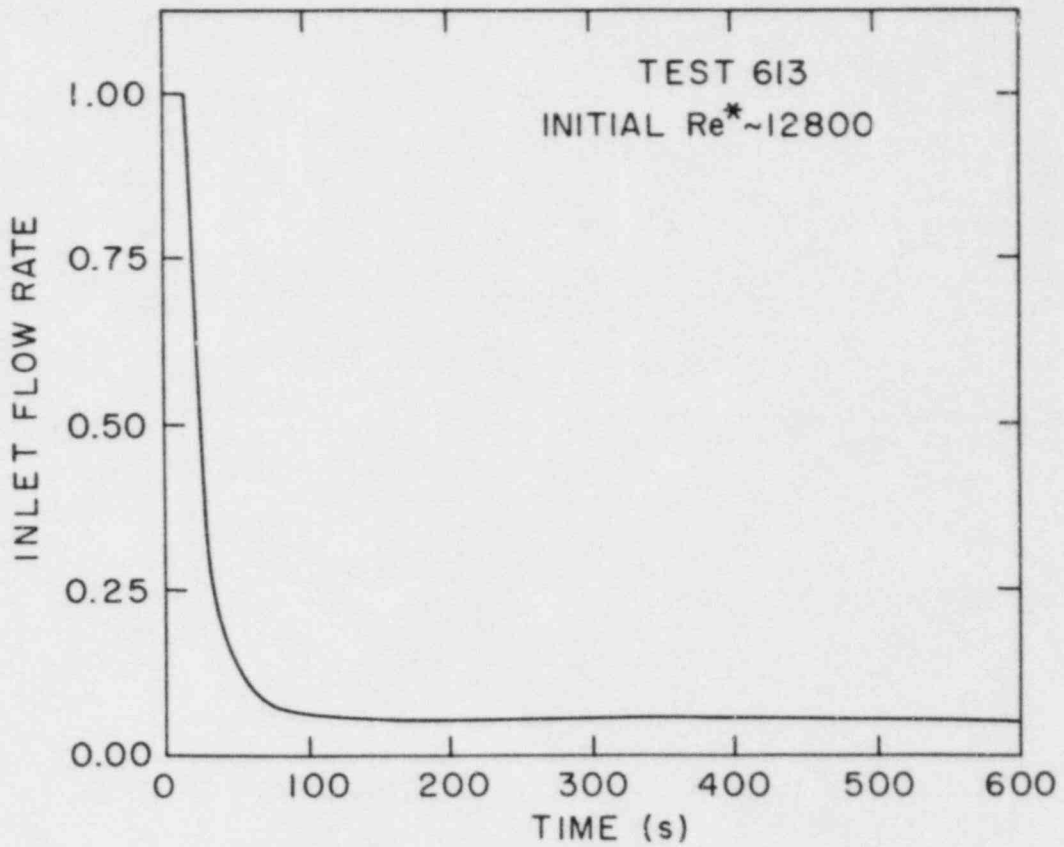

Figure 2.2 Test Section Flow Rate

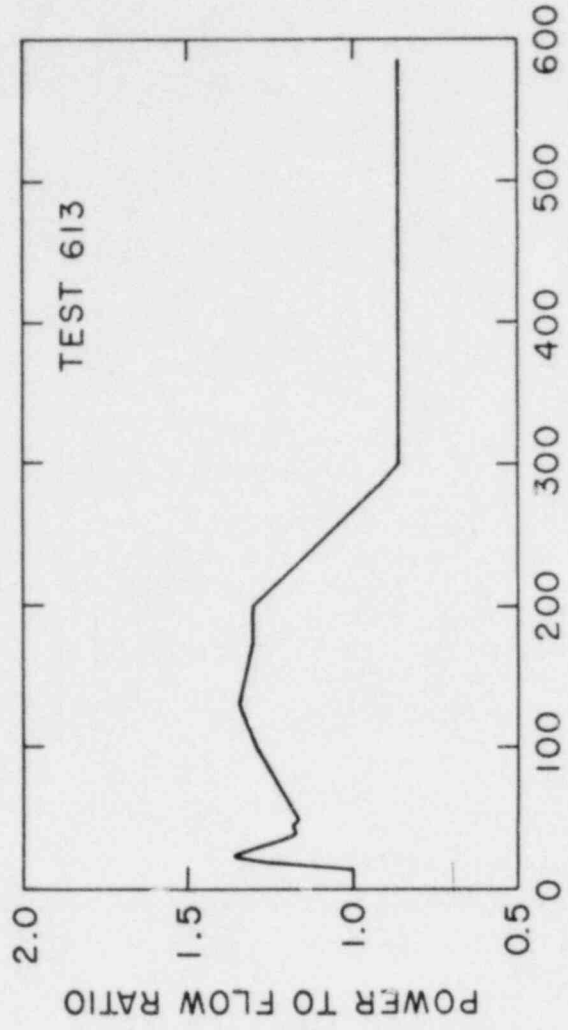

Figure 2.3 Power-To-Flow Ratio

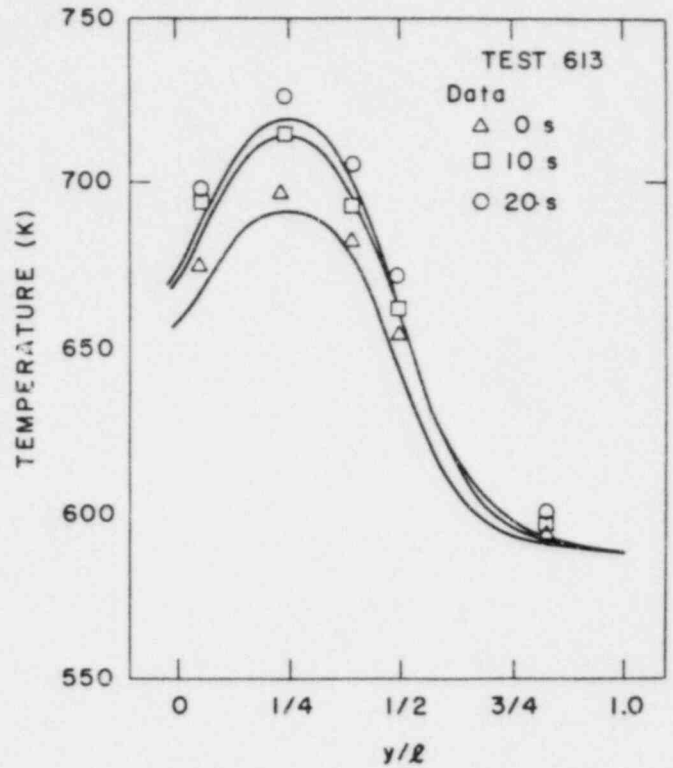

Figure 2.4 Test Section (Sodium) Transverse Temperature Profile

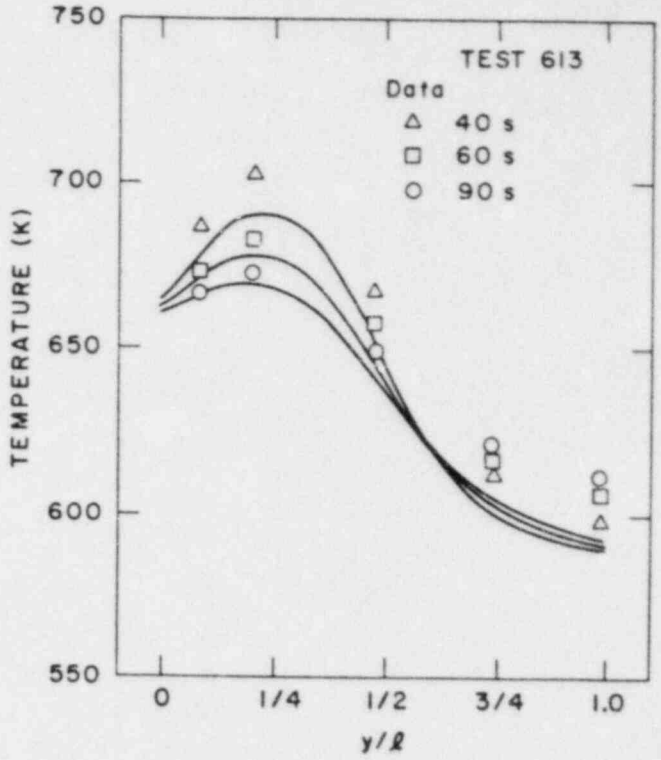

Figure 2.5 Test Section (Sodium) Transverse Temperature Profile

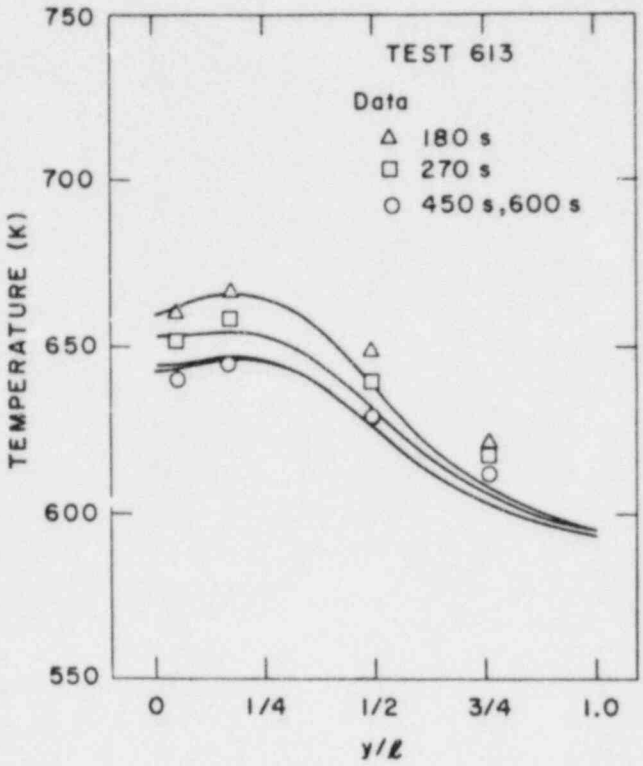

Figure 2.6 Test Section (Sodium) Transverse Temperature Profile

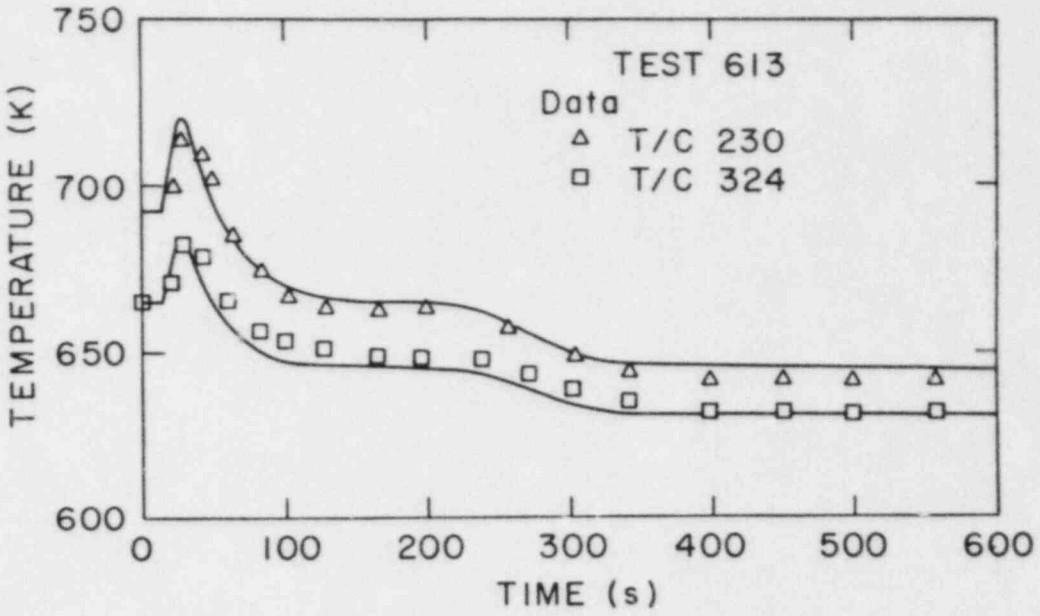

Figure 2.7 Comparison of Measured and Calculated Sodium Temperature at the Exit of the Heat Section

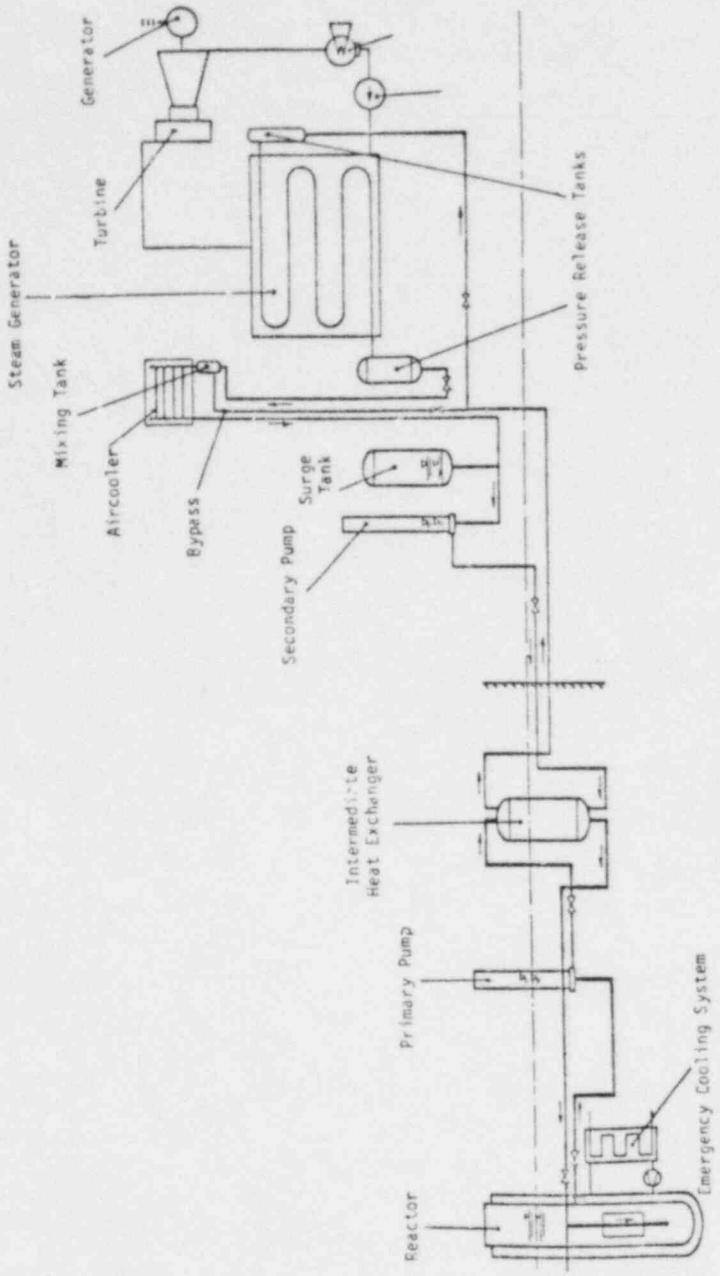

Figure 2.8 KNK-II Plant Layout

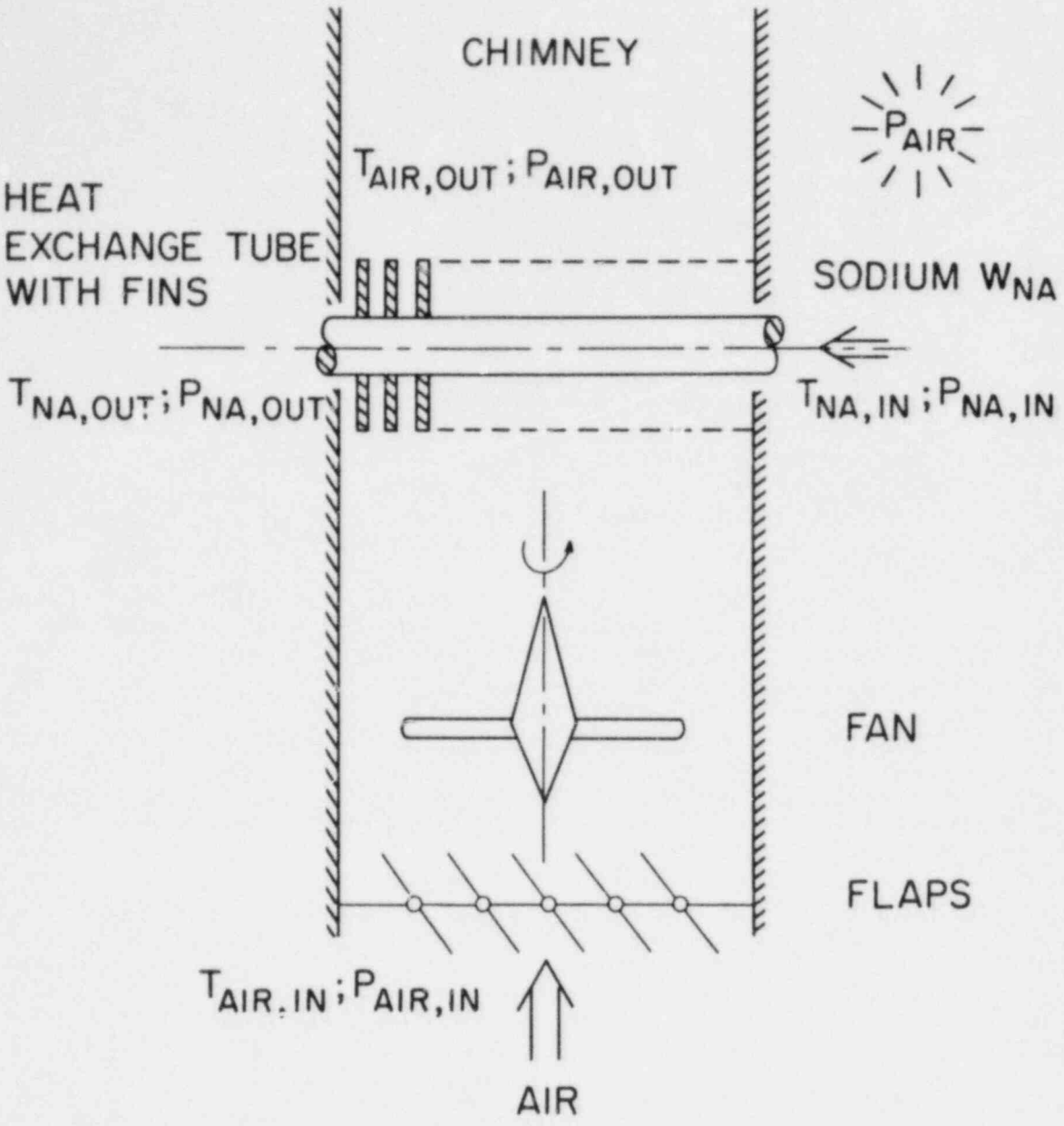

Figure 2.9 Dump Heat Exchanger Model Arrangement

For the modeling of the heat exchanger and the hydraulic response, the following assumptions apply:

- one dimensional flow
- no axial heat conduction
- incompressible fluids
- the logarithmic mean temperature is valid
- the heat transfer mechanism of the air-side dominates the whole heat transfer process
- air is treated as ideal gas,
- thermal and hydraulic inertias of air are neglected.

The energy equation for the DHX sodium side is written using the log mean temperature difference (LMTD) approach. The use of the LMTD is exactly valid only in the case of counter-current flow. The application here to a cross-flow heat exchanger is done by introducing a correction factor, which considers the reduced heat transfer rate under these conditions.

2.1.2.2 Fan Model

In order to be able to simulate the fan behavior under accident conditions, e.g. station blackout, or air flow control with variable fan speed instead of variable blade angle, fan curves are described by polynomials as obtained by the homologeous theory (Street and Wylie, 1967). The polynomial coefficients are based on values given by (Cady, 1979). These values were obtained from FFTF measurements. They do not necessarily fit those measured in KNK-II, but because of the lack of sufficient KNK-II data and because the general behavior of fans should not be much different, these values are used in the present model. In addition, the adjustable fan blade angle is modeled by a given function multiplied with polynomial results.

The dynamic behavior of the fan is expressed by an angular momentum equation. The momentum loss due to friction is modeled by the following relations as proposed by (Cady, 1979). Because the momentum loss due to friction only becomes important under low pump speed conditions, the equation is limited to low pump speeds. For the motor torque it is assumed that the pump shaft and the impeller are accelerated until they reach design speed at the full design torque. After pump trip, the pump torque becomes zero.

During normal operation, the air cooler chimney is closed by flaps which cause the heat exchanger pipes to remain in an almost adiabatic condition, as assumed in the previously described model. However, after scram occurs, these flaps open automatically and air circulates through the chimney. It has been found that during air cooler start-up transients, air flow caused only by natural convection can become high enough to drop the sodium outlet temperature

substantially below the set point. To avoid such behavior, the flaps are incorporated in the control process and act as a control device via the pressure drop, as well as the adjustable fan blade.

2.1.2.3 Controller Model

A controller is used to adjust the air cooler sodium outlet temperature to its pre-scram value. Figure 2.10 shows the principal arrangement. The controller chain consists of two cascades, where the second cascade uses a proportional-integral-differential controller. Controlled variables are the air cooler sodium inlet and outlet temperatures. To obtain better control behavior, the error signal of the inlet temperature is added via a differential controller to the main controller inlet. The assigned temperatures before scram serve as set point values. The models used to describe the controlling chain are those suggested by (Khatib-Rahbar, 1980) and explained in more detail therein. A block diagram of a unit controller is shown in Figure 2.11.

The dynamics of the power element flaps and fan blades are described by first order differential equations with higher order influences neglected.

2.1.2.4 Numerical Considerations

The assumption that both fluids can be treated as incompressible, simplifies the numerical solution significantly. Because the hydraulic equations depend only slightly on the energy equations, whereas on the other hand the temperature field is strongly coupled to the flow rate, the hydraulics is solved first, using the temperatures of the last time step. The energy equation is then solved utilizing the updated flow rate.

The sodium energy equation is transformed into a finite-difference equation for the numerical solution. For further numerical simplification, the source term in the energy equation uses the temperatures of the previous time step. The assumption made here is that the source term should vary only slightly during a transient, which is certainly the case in slow decay heat removal transients.

Because of the non-linearity of the source term and the small amount of mass on the air side (causing a small heat capacity), the air side energy equation is highly unstable when solved directly. Hence, this equation is solved iteratively for each time step with a Newton-Raphson procedure.

During operational transients, only the sodium equations must be solved and the source term (q) is equal to zero. At the beginning of a DHX start-up transient, q is indefinite. Hence, a steady-state solution is first provided for the entire system where both energy equations are solved iteratively by Newton-Raphson.

The air side hydraulic equation provides, explicitly, the air mass flow rate. However, for the sodium side hydraulics, the respective pressure terms are calculated and added to the overall secondary loop pressure loss, and the SSC integrator package calculates the advanced sodium flow rate.

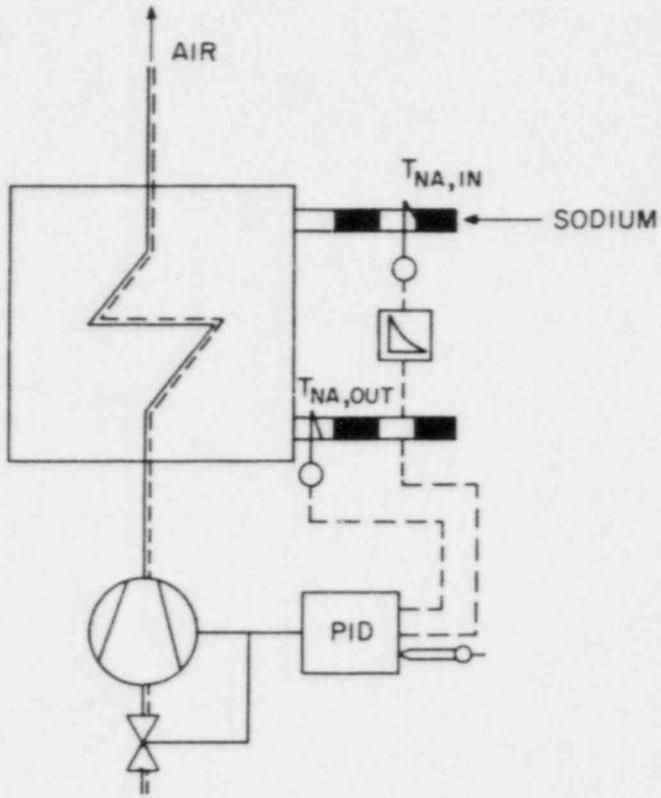

Figure 2.10 Principal Controller Arrangement

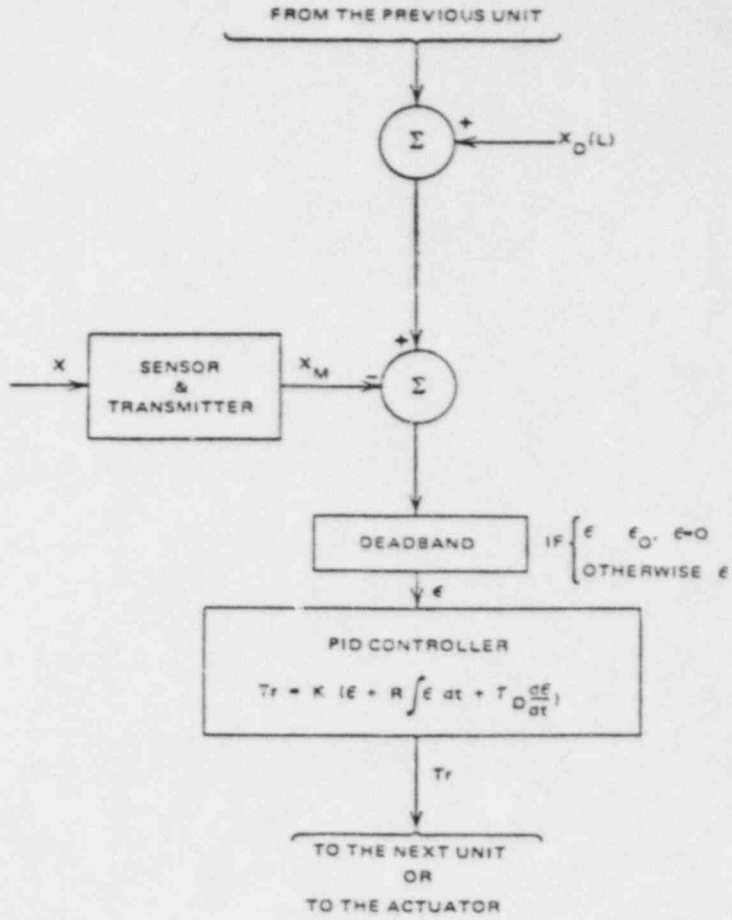

Figure 2.11 Block Diagram Representation of the Unit Controller

In order to be sure that no numerical instabilities are caused by the sodium energy equation, several stability criteria, as given by Courant (Roache, 1972) and (Madni, 1980), have been checked for different cases over their expected ranges. The results are depicted in Table 2.1. Comparing the most restrictive characteristic time constants with the SSC time steps calculated during test runs, it can be stated that these values are well within the range of values calculated by SSC. Therefore, an additional time step control for the model was not incorporated into the code.

The interface between SSC and the DHX model is easily done by providing the sodium mass flow rate, the sodium inlet temperature and a scram flag, which indicates whether scram occurred or not for the DHX. The DHX itself delivers the sodium outlet temperature back to SSC.

2.1.2.5 Post Shutdown Control System

During post scram conditions the reactor power usually drops much faster than the core flow rate in the first few seconds. This results in a large and rapid temperature variation at the core outlet which may lead to thermal stress on the structures, thus eventually influencing the long term reliability of the plant. In order to reduce thermal stress, German plant designs use motor operated valves in the primary and intermediate loops to decrease and adjust the flow rate more rapidly to match the relative power and to minimize large temperature variations in the reactor circuits.

The typical controller circuit for the flow control under natural circulation conditions is shown in Figure 2.12. The controlled variable is the flow rate in either the primary or secondary loop. This value is compared to the demanded flow rate which is a function of the produced power and, compared to the level before scram, the stored power in the system. A three point switch (on-off-on controller) uses the signal from the comparator to drive a valve motor.

The impact of the valve is felt through its pressure loss. The valve position dependent pressure loss is introduced by the drag coefficient (C_v) which is a function of the valve stem position. Because the function is highly dependent on the valve design, no function is given here, but values can be found in (Hutchinson, 1976).

2.1.2.6 Results

The models described previously have been coded and tested on a stand-alone basis in order to assess model features and limitations, as well as the controller settings. As a reference transient, a sodium inlet temperature ramp of 3 K/s has been used, with the sodium flow rate kept constant at 9.5 kg/s. These values are within the expected range of the KNK-II experiments and the SSC-DHX calculations. The results are presented in Figures 2.13 - 2.16.

In Figure 2.16, the behavior of the air-flow controller actuator elements is shown. After reactor scram, the DHX fan is started at once, whereas the

Table 2.1 Comparison of Characteristic Time Constants
Using Different Criteria

$T_{NA} = 700^{o}$ $\rho_{NA} = 850^{o}$ $c_{pN4} = 1270$	$\frac{\Delta X \cdot \rho \cdot A}{W_{NA}}$	$\frac{2m\ c_p}{h\ A_{AIR}}$	$\frac{W_{NA}\ c_p}{W_{NA}\ c_p + 0.5\ hA_{AIR}}$
$h = 0$ $W_{NA} = 125$	0.1	-	0.1
$h = 0$ $W_{NA} = 8.75$	1.5	-	1.5
$h = 4.5$ $W_{NA} = 8.75$	1.5	165	1.47
$h = 65.$ $W_{NA} = 8.75$	1.5	11.5	1.3
$h = 65.$ $W_{NA} = 25.$	0.52	11.5	0.5

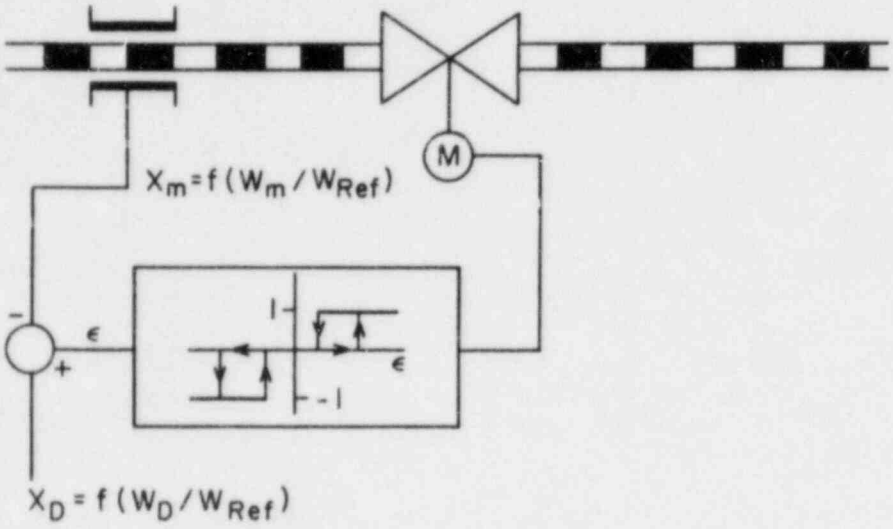

Figure 2.12 Controller Circuit for After Scram Flow Control

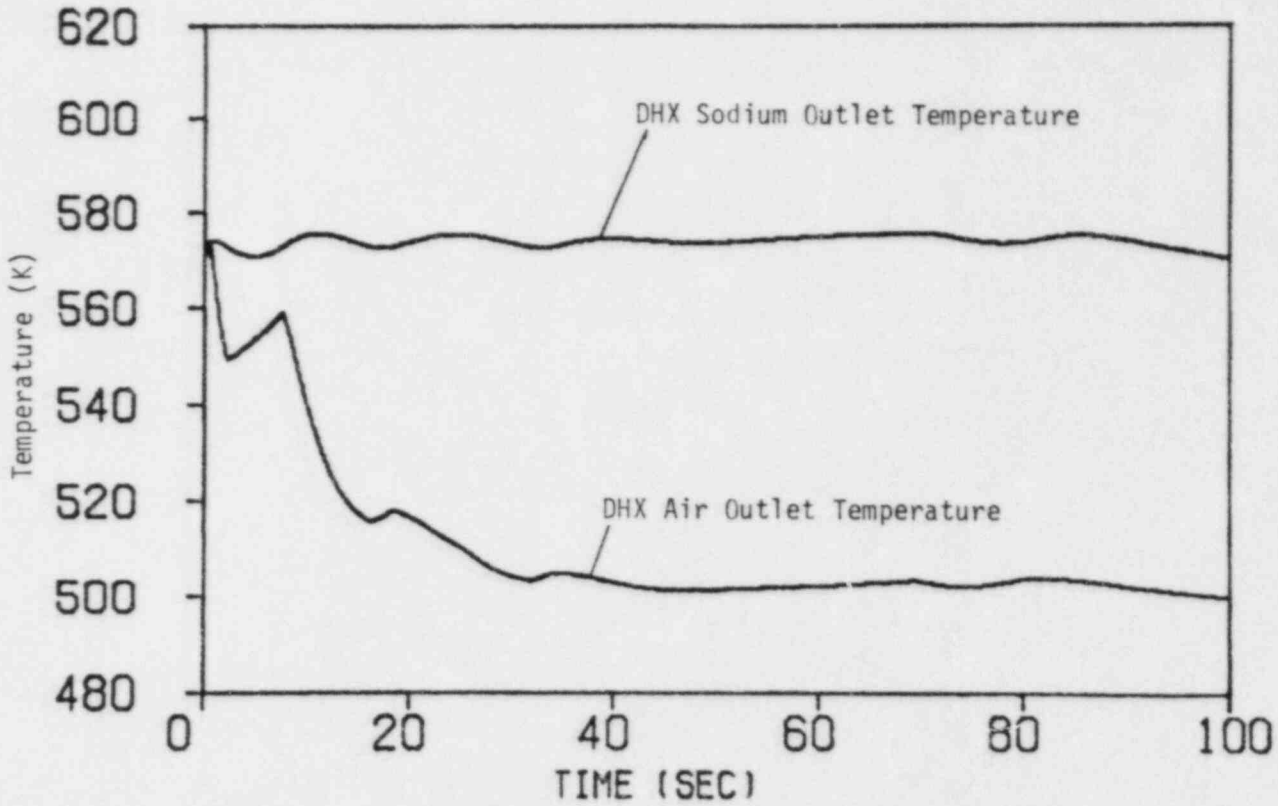

Figure 2.13 DHX - Outlet Temperatures (Ref. Case)

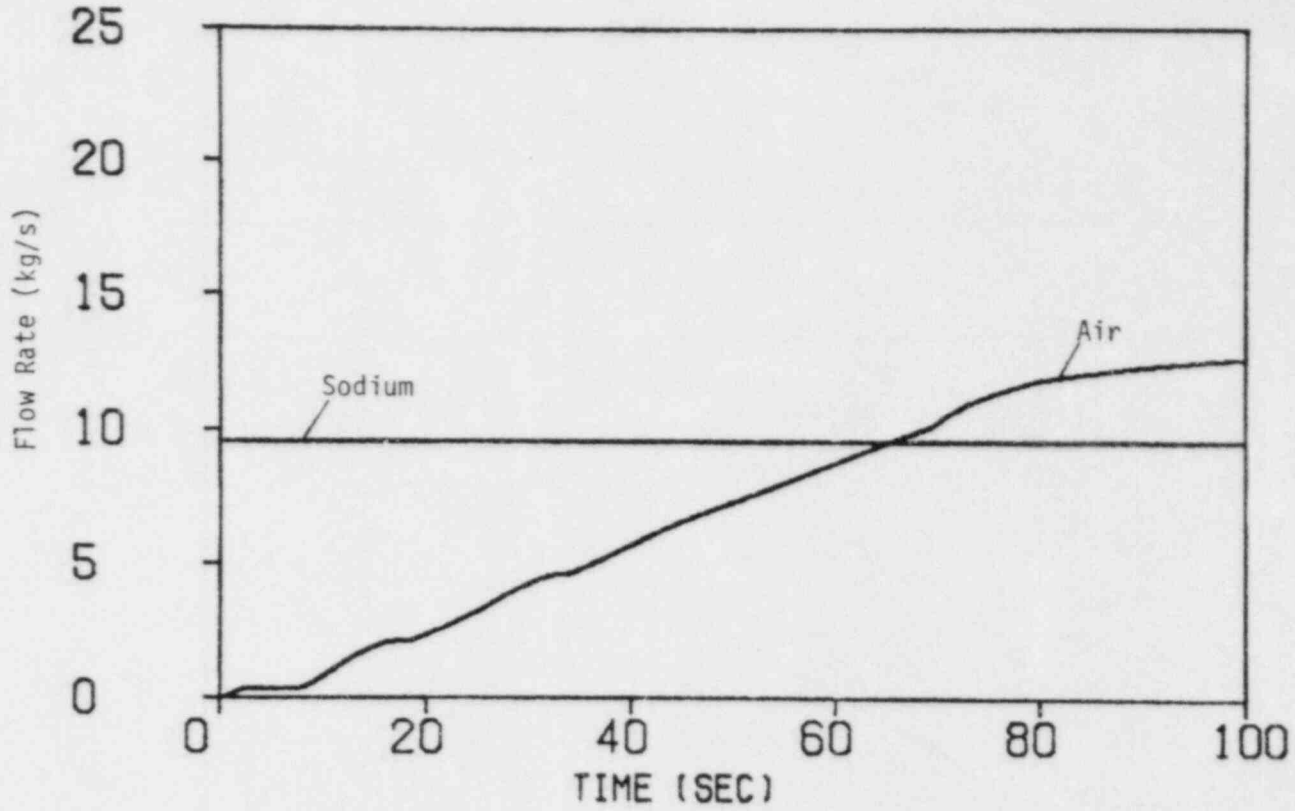

Figure 2.14 DHX - Flow Rates (Ref. Case)

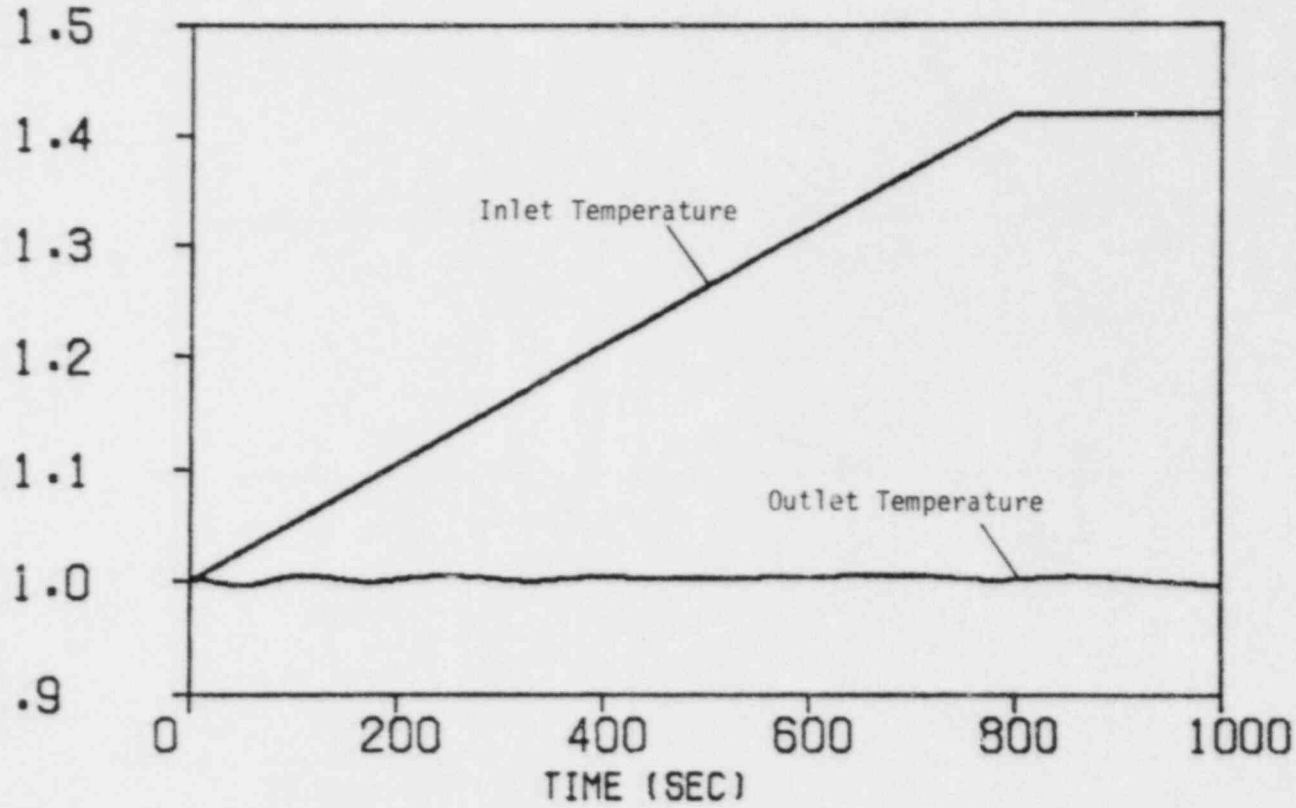

Figure 2.15 Normalized DHX Sodium Temperatures (Ref. Case)

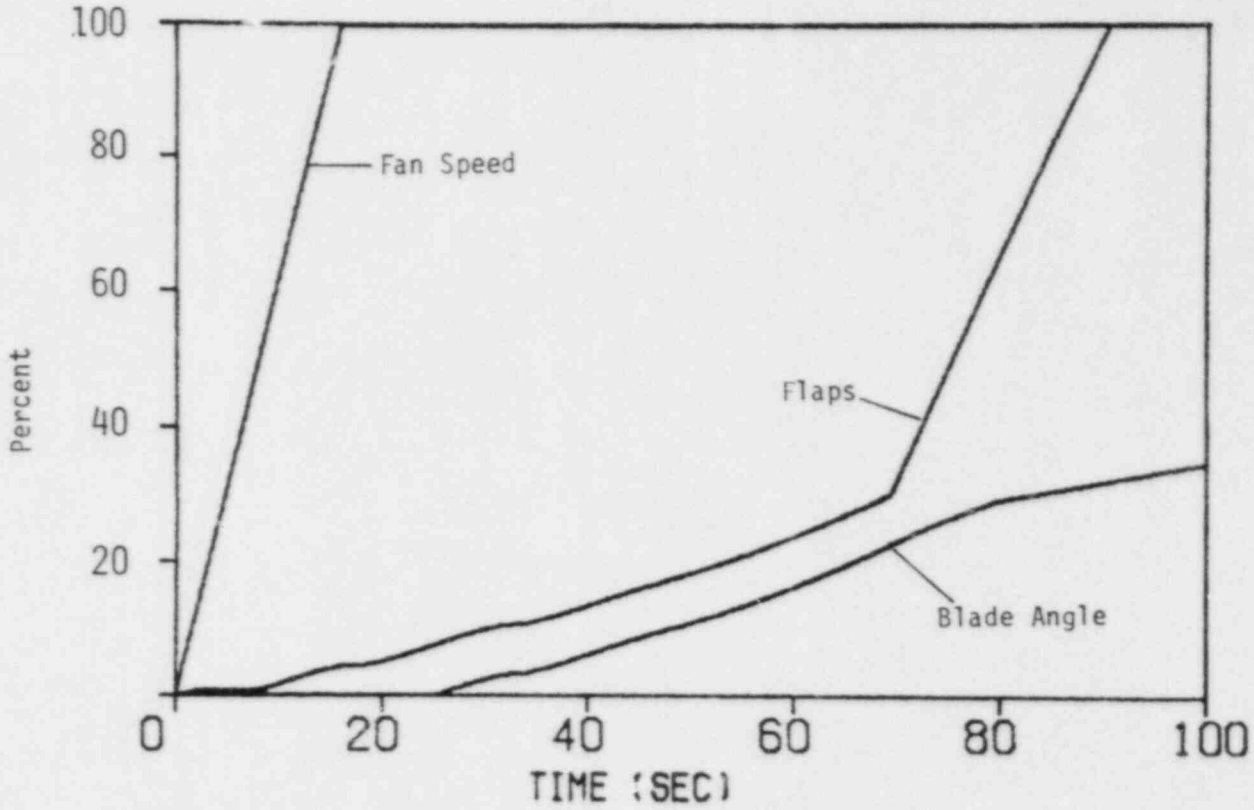

Figure 2.16 Behavior of Air Flow Controller Actuator Elements
(Ref. Case, normalized)

blade angle is still kept at zero. When the sodium temperatures exceed the controller deadband, the flaps open. The DHX air outlet temperature drops immediately (Figure 2.13), causing the sodium outlet temperature to fall under the controller set point temperature. Thus, the flaps stop opening and the air flow rate remains almost constant for several seconds (Figure 2.14). Then the flaps continue to open. After 25(s) the flap opening reaches 7.5% of full open and the blade angle adjustment provides additional support for the air flow delivery.

The movement of the blade angle was initiated on the basis of the flap position of 7.5% in order to satisfy the air flow demand signal in a reasonable time scale. The influence of the flap motion on the air flow rate becomes less important after exceeding a value of 30% open and, hence, the flaps are decoupled from the controller signal and open at a higher constant rate.

Figure 2.15 illustrates that the DHX inlet sodium temperature stabilizes at about 813°K which corresponds to a 240°K desired ΔT across the heat exchanger. The system then starts to settle down to steady conditions as is indicated by the slow decrease of the air flow rate.

Because the scram conditions for the DHX are not accurately known at present, several other transients were calculated with varying sodium flow rates (0.5 to 3.0 x W_{Ref}) and inlet temperature gradients (1.5 to 4.5 K/s). It was found that in all cases the system behaves adequately, although the controller settings may need to be readjusted at a later time when the code is coupled with SSC and/or actual parameters are known.

2.2 SSC-P Code (E.G. Cazzoli)

2.2.1 Code Maintenance (E.G. Cazzoli)

The pool version of SSC is under review and is being modified to upgrade it to the latest cycle of the program library, in order to take advantage of recent improvements in SSC-L. In order to establish that the revision is performed consistently, we plan to analyze plant test transients for the PHENIX reactor, simulated previously, and compare results.

Because of the existence of only one base program library, which contains all the subroutines and coding for all versions of SSC, much unnecessary work has been very carefully avoided. Wherever there is over-lapping use of a subroutine from one version to another, the programming need not be duplicated. Likewise with code validation, once a code module or model has been validated for one version, it is automatically validated for all SSC versions to which it is common.

2.2.2 Modeling of Reactivity Feedback Effects for the EBR-II Reactor (C. McAndrews, W.C. Horak, R.J. Kennett)

In order to simulate reactivity transients for the EBR-II reactor (a cold-pool design), modifications were made to SSC to handle the input of overall reactivity coefficients. The modifications were made to three subroutines: DOPP5T, VOID5T, GROW5T.

A. DOPP5T

The Doppler contribution is calculated by averaging the temperatures over the active fuel regions and applying Eq. 2.4.

$$R5DOPP = \sum_{n=1}^{n_{last}} F5BDOP(n) \star ALOG\ (AVGTEMP/T85REF) \qquad (2.4)$$

where,

R5DOPP = Doppler feedback reactivity

F5BDOP = Average Doppler coefficient for channel n

AVGTEMP = Average temperature of active fuel

T85REF = Cold shutdown reference temperature.

B. VOID5T

The sodium void contribution was calculated for the average fuel channel and average reflector assembly. The original subroutine considered a change in density with respect to a reference density, with a mass difference subsequently calculated. The sodium void coefficient was to be supplied with units of reactivity per kilogram. However, the information received from ANL was in units of reactivity per degree Fahrenheit. Therefore, the original subroutine was extensively modified.

The changes included calculating an average nodal temperature, taking its difference from a reference temperature and computing the sodium void reactivity feedback (Eqs. 2.5 - 2.6).

$$DELTEMP = (T6NODE(J) + T6NODE(J+1))/2.0 - T85REF \qquad (2.5)$$

$$R5VOID = \sum_{n=1}^{n_{last}} \sum_{J=1}^{J_{last}} F5VWGT(n,J) \star DELTEMP \qquad (2.6)$$

where, T6NODE = Coolant temperature at each axial nodal interface of each channel

F5VWGT = Sodium void reactivity coefficient for each node of each channel.

The input of F5VWGT is on an axial basis so that the coefficient pertaining to the particular slice of a channel is the total coefficient for that subinterval divided by the number of nodes in the subinterval. The sodium regions considered are the driver Na region, upper reflector Na region, and radial reflector Na region. The coefficients for the driver and upper reflector Na region are applied to the average fuel assembly while the radial reflector Na region coefficient is applied to the average reflector assembly.

C. GROW5T

The calculations of the effects of fuel radial expansion and control rod bank extension on reactivity are made through GROW5T. This routine was modified greatly so as to handle the data given by ANL. The channels considered were the average fuel assembly and the average control rod assembly.

The contribution is calculated by obtaining a change in temperature on a nodal basis due to fuel radial expansion in the average fuel assembly, with respect to a reference temperature, and then multiplying by the appropriate expansion coefficient (Eqs. 2.7 - 2.8).

$$\text{DELTEMP} = \text{T5DPAV(J)} - \text{T85REF} \tag{2.7}$$

$$\text{R5GROW} = \text{R5GROW} + \text{F5AWG6T(J)} \star \text{DELTEMP} \tag{2.8}$$

where, T5DPAV(J) = Volume-average fuel temperature in each axial slice

F5AWGT(J) = Fuel axial expansion reactivity coefficient for each axial slice J of channel K.

The input of F5AWGT is again on an axial basis and found from the overall coefficient in the same manner as in VOID5T. Since the input data were supplied in this form, no special consideration was given to the fact that a change in temperature was calculated for a non-fueled region, i.e., lower blanket.

The control rod bank expansion reactivity coefficient is given in units of reactivity per foot. Therefore, in calculating the reactivity contribution, the linear expansion of the control rod due to a change in temperature must be determined. Equation 5-7 of the SSC manual (Guppy, et al., 1983b), was used to find α, the average linear coefficient of thermal expansion. This was then used to find the reactivity contribution due to linear expansion (Eq. 2.6).

$$\text{R5GROW} = \text{ALPHA} \star \text{Z5AFUL} \star \text{F5AWGT} \star \text{DELTEMP} \tag{2.9}$$

where, Z5AFUL = Active fuel length

DELTEMP = Average temperature of control rod - reference temperature

Since the temperature did not change much it was not necessary to calculate the contribution due to control rod bank expansion for the rod drive region. The contribution was calculated for the section of control rod inside the reactor.

2.3 SSC-S Code (B. C. Chan)

2.3.1 Improved Upper Plenum Modeling (B.C. Chan)

The transient hydro-thermal model has been completed and incorporated into

the upper plenum stand-alone code. A configuration considered to be representative of an outlet plenum, utilizing 12 x 10 mesh cells, has been run. In this transient calculation, an input inlet temperature profile was initialized to 783°K at time zero and dropped to 616°K in the first 20 seconds. The inlet velocity profile was 2.132 m/s at time zero and dropped to 0.2133 m/s in 35 seconds. Approximately 11 seconds of CDC-7600 CPU time were needed for 70.0 seconds of real time transient simulation. This included the steady state calculation, print-out at every time step and plot file creation.

A calculational procedure has also been tested for a slow transient problem. In each cycle (timestep) of operation, momentum and energy equations are calculated separately. First, the momentum equation is calculated (iterated) until the flow field converges. Then the energy equation is calculated. This procedure can save up to 20% of the computer time required for the simulation of slow transients.

A preliminary report describing the upper plenum modeling and computational techniques is being prepared.

2.4 Code Validation (W.C. Horak)

2.4.1 Pre-test Calculations Using Improved EBR-II Reactivity Modeling (C. McAndrews, W.C. Horak, R.J. Kennett)

SSC has been used to simulate the effects of reactivity feedback on plant power control during transients without scram. Two EBR-II shutdown heat removal tests (SHRT) involving flow coastdowns with no reactor scram were simulated using SSC. These tests are to be conducted at the EBR-II facility in the near future. The two tests are SHRT-A031, which has a primary pump trip with the secondary pump left at the steady-state speed, and SHRT-A032, in which the primary and secondary pumps are tripped. Both cases are initiated from a 25% power, 25% flow condition and were simulated for a total of 360(s).

Negative reactivity feedback was observed in both cases with a gradually decreasing power level (Fig. 2.17) leading to a stabilizing of the coolant temperatures well below saturation conditions. No substantial differences were noted in the peak core coolant temperature between the two cases. This was primarily due to the large thermal inertia of the sodium pool.

The highest sodium temperature in the core occurred in the hot fuel channel at 190 seconds into the transient (Fig. 2.18). The sodium was at a temperature of 982 K and at a pressure of 1.42265×10^5 Pa, well below boiling conditions. The hottest point in the fuel occurred at 136 seconds into the transient. It was again in the hot fuel channel, as expected, and the temperature was 980 K.

In terms of plant control, the net effect of the temperature increase was seen in the reactivity feedback. The Doppler, void, and growth reactivity feedbacks turned negative and continued to become more negative (Figs. 2.19 - 2.20). As seen through the accompanying graphs, the void and Doppler contributions rose to a peak negative value and then became less negative as the

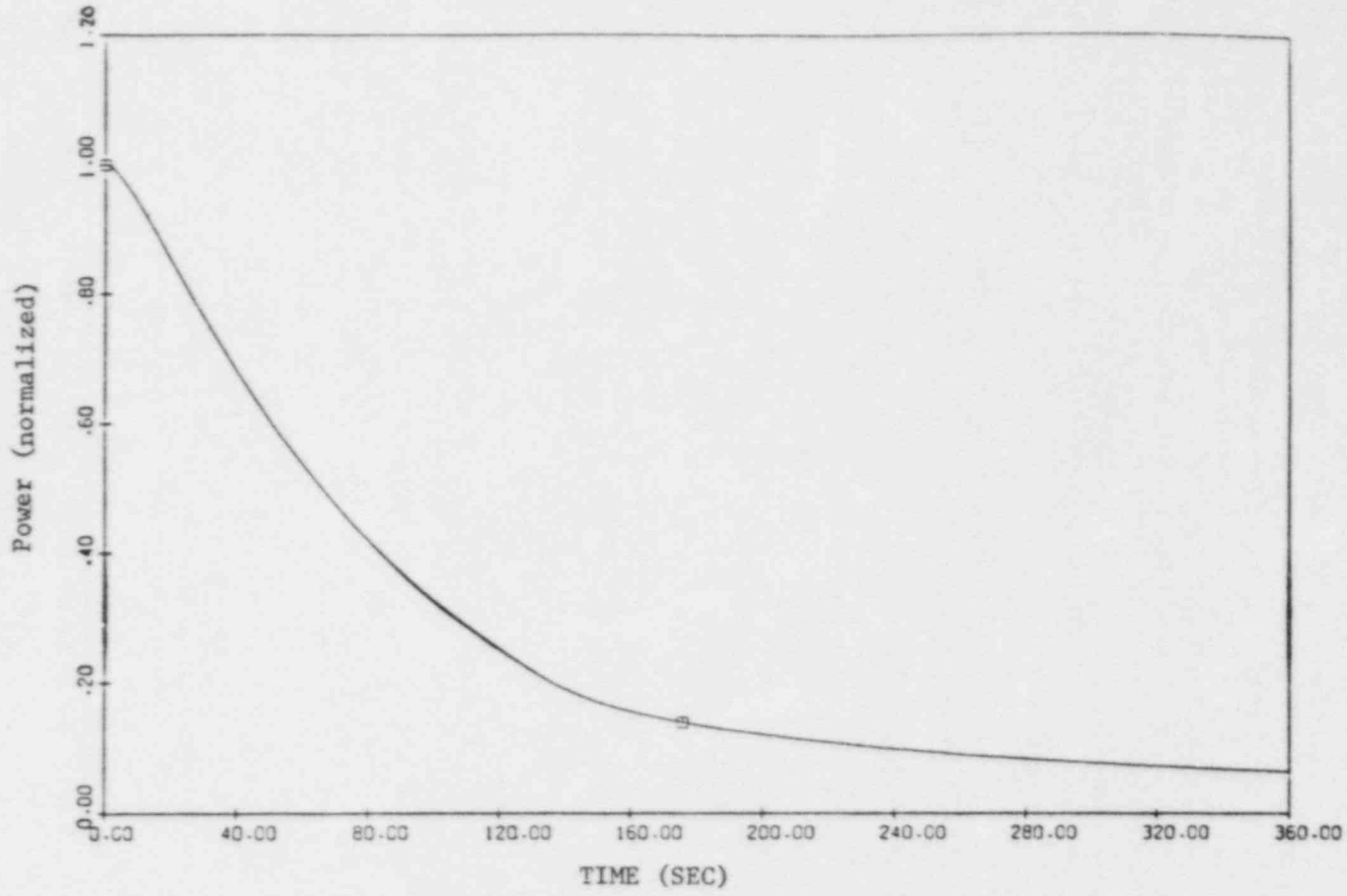

Figure 2.17 Normalized Fission Reactor Power

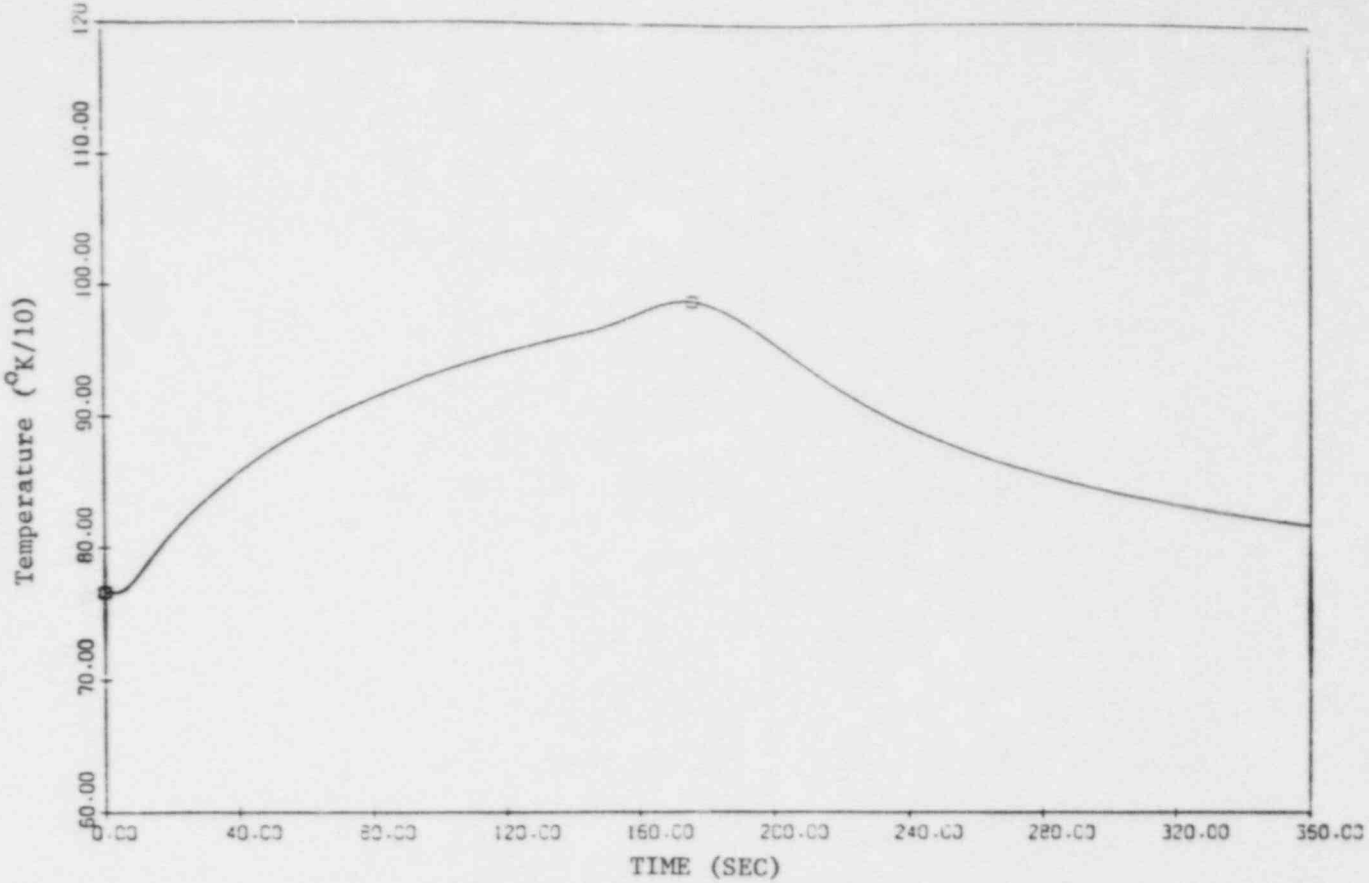

Figure 2.18 Hot Fuel Assembly
Temp (K)

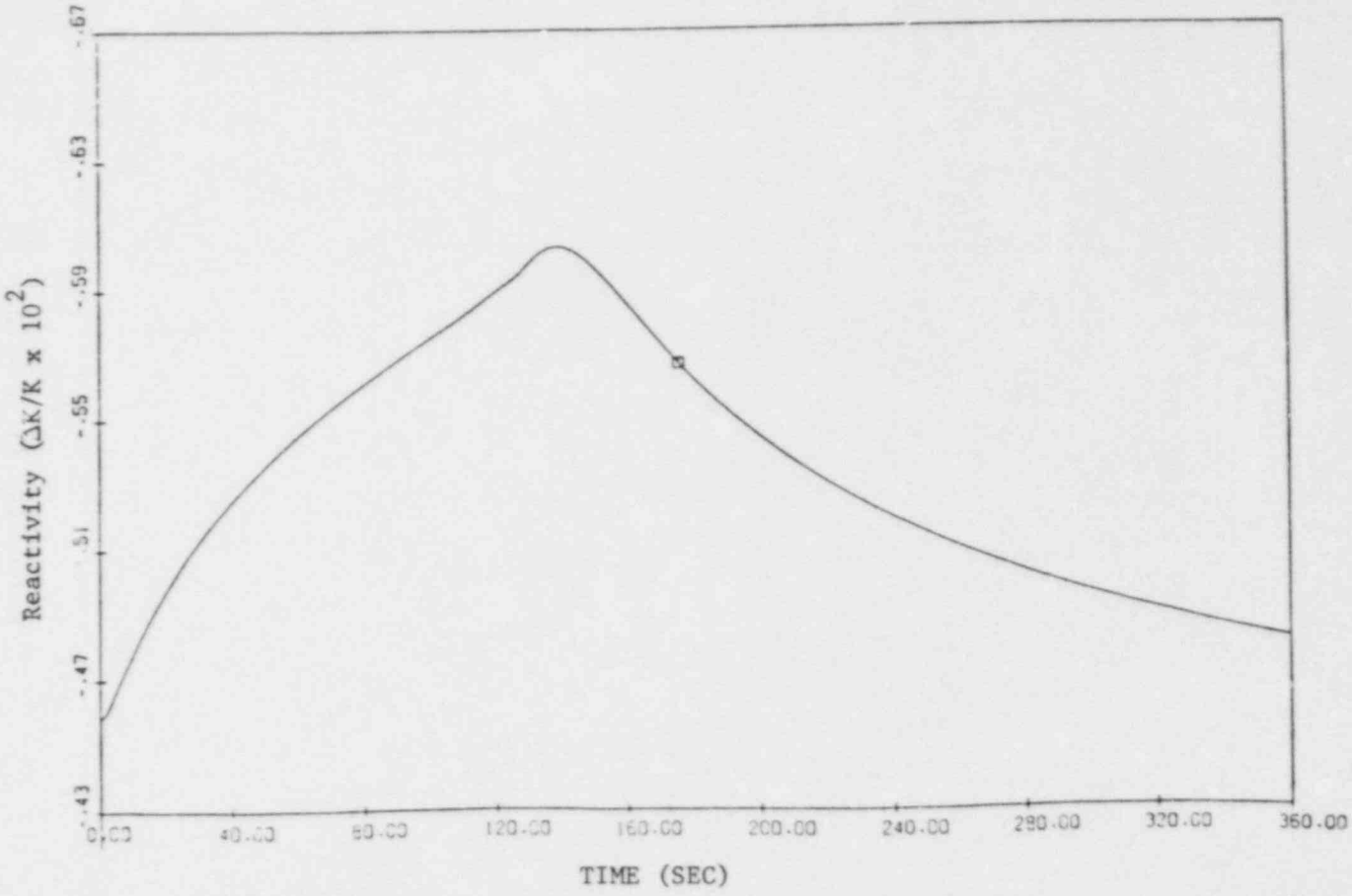

Figure 2.19 Sodium Void Feedback Reactivity

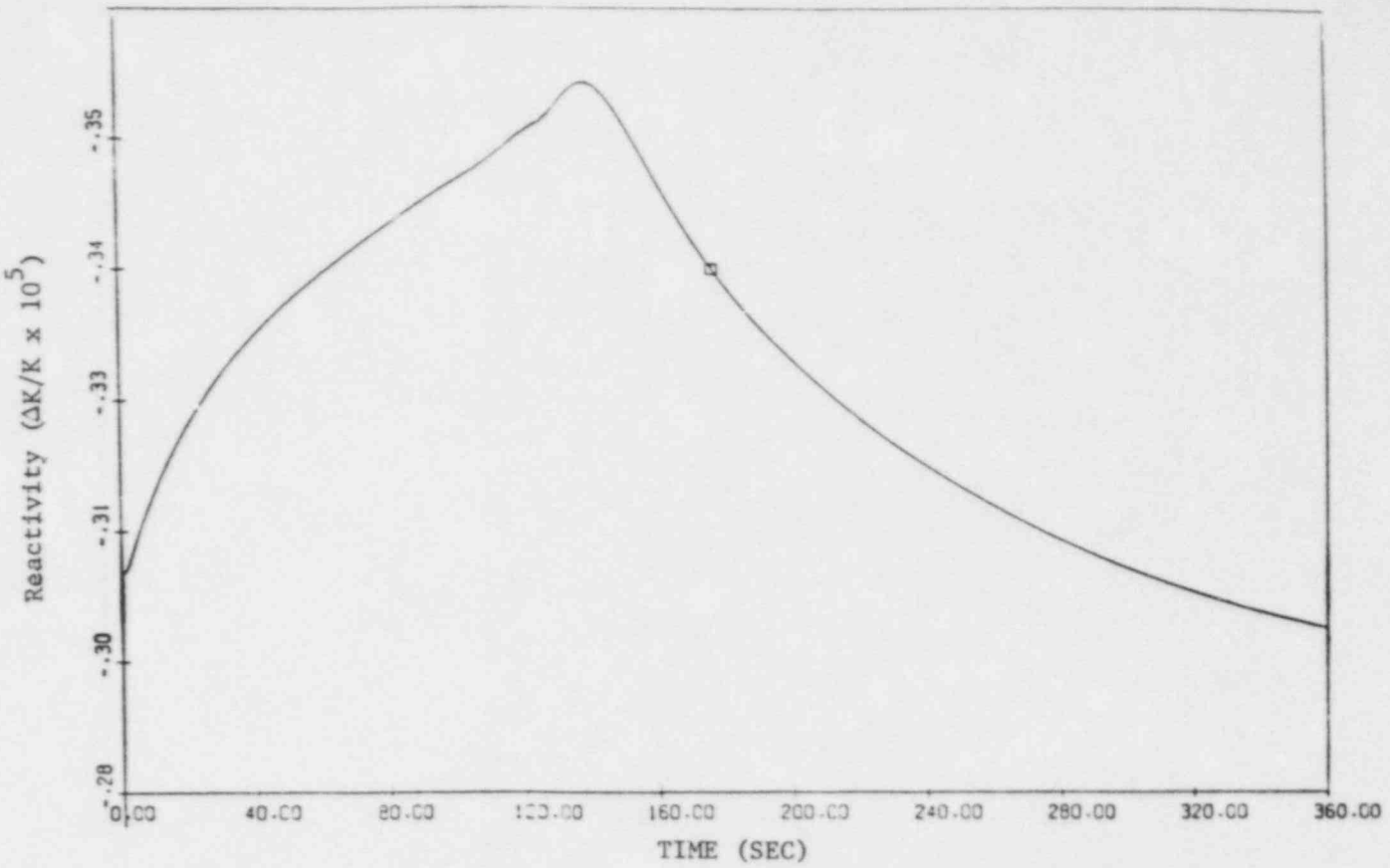

Figure 2.20 Doppler Feedback Reactivity

plant approached a new equilibrium condition. The total contribution from the three effects was 24.42¢ worth of negative reactivity at peak values. Individual contributions are summarized in Table 2.2.

Table 2.2 Feedback Reactivity at Maximum Change

Type	Δ$
Doppler	8.81×10^{-5}
Void	.226
Growth	.0184
	.2442 = Total*

*Time compared was 138 sec and 0 sec

Further testing of the reactivity modeling in SSC will be made as more information is obtained from EBR-II.

2.4.2 Upper Plenum Revision (W.C. Horak)

A change was made in the energy balance equation for the upper plenum two-region model. This change was made to correct a slight discrepancy in the temperature calculation for the upper (hotter) region when the two regions initially form.

2.4.3. IHX Plena Thermal Masses (W.C. Horak)

Long term FFTF simulations have shown a need to include the effect of the metal structure in the IHX plena in the temperature calculations for the plena. Generic changes to the code to account for this effect are now being implemented and tested.

2.4.4 FFTF Long Term Simulations (W.C. Horak, R.J. Kennett)

During this quarter, long term simulations of the four FFTF scram-to-natural circulation tests were completed. The 100%, 75%, and 35% power tests were simulated for a total of 3600(s) each. The 5% power case was simulated for a total of only 1500(s) since the actual experiment was terminated at that time by restarting the pumps. In all cases, a four channel core model with two heat transport loops was used. Computational time was approximately three to four times faster than real time. Initial analyses of the data indicate good agreement with the experimental data, but some discrepancies still exist in the secondary flow rates. The results will be analyzed more fully in the near future and a final report issued.

REFERENCES

CADY, K. B., (1979), "An Air Blast Heat Exchanger System Model," Brookhaven National Laboratory, BNL-NUREG-26237, June 1979.

GUPPY, J. G., et al., (1983a), "SSC Development, Validation and Application," Safety Research Programs Sponsored by Office of Nuclear Regulatory Research Quarterly Progress Report, April 1 - June 30, 1983, Brookhaven National Laboratory Report to be published.

GUPPY, J. G., et al., (1983b), "Super System Code (SSC, Rev. 2), An Advanced Thermohydraulic Simulation Code for Transients in LMFBRs," Brookhaven National Laboratory, BNL-NUREG-51650, April 1983.

HUTCHINSON, J. W. (1976), "ISA Handbook of Control Valves," Instrument Society of America, Pittsburgh, PA, 1976.

KHATIB-RAHBAR, M. (1980), "Modeling of Plant Protection and Control Systems for SSC," Brookhaven National Laboratory, BNL-NUREG-51241, June 1980.

KNK-II, (1977), Sicherheitsbericht KNK-II, Band 1-3, INTAT 78.7, 1977.

MADNI, I. K., (1980), "Transient Analysis of Coolant Flow and Heat Transfer in LMFBR Piping Systems," Brookhaven National Laboratory, BNL-NUREG-51179, April 1980.

ROACHE, P. J., (1972), "Computational Fluid Dynamics," Hermosa Publishers, 1972.

STREETER, V. L. and WYLIE, E. B. (1967), "Hydraulic Transients," McGraw-Hill, New York, 1967.

PUBLICATIONS

CHAN, B. C., "A Buoyancy-Dominated Model for LMFBR Upper Plenum Flows," Brookhaven National Laboratory, BNL report to be published, 1983.

GUPPY, J. G., et al., "Super System Code (SSC, Rev. 2), An Advanced Thermohydraulic Simulation Code for Transients in LMFBRs," Brookhaven National Laboratory, BNL-NUREG-51650, April 1983.

HORAK, W. C., et al., "Short Term Post Test Analysis of the FFTF Scram to Natural Circulation Transients Using SSC," Brookhaven National Laboratory, BNL report to be published.

KHATIB-RAHBAR, M., CAZZOLI, E. G., "Two-Dimensional Modeling of Intra-Subassembly Heat Transfer and Buoyancy-Induced Flow Redistribution in LMFBRs," Brookhaven National Laboratory, NUREG/CR-3498, BNL-NUREG-51713, 1983.

KHATIB-RAHBAR, M., "Core Coolability Following Loss-of-Heat Sink Accidents," Trans. Am. Nucl. Soc. 45, 365, (1983).

KHATIB-RAHBAR, M., "Intra-Assembly Flow Redistribution in LMFBRs: A Simple Computational Approach," Trans. Am. Nucl. Soc. 45, 816, (1983) also see 1st Proc. of the T&H Division, 13-20 (1983).

3. Balance of Plant Modeling (J. G. Guppy)

The Balance of Plant (BOP) Modeling Program deals with the development of safety analysis tools for system simulation of nuclear power plants. It provides for the development and validation of models to represent and link together BOP components (e.g., steam generator components, feedwater heaters, turbine/generator, condensers) that are generic to all types of nuclear power plants. This system transient analysis package is designated MINET to reflect the generality of the models and methods, which are based on a momentum integral network method. The code is to be fast-running and capable of operating as a self-standing code or to be easily interfaced to other system codes. Reference is made to the previous quarterly progress report (Guppy, 1983) for a summary of accomplishments prior to the start of the current period.

3.1 Balance of Plant Modeling (G.J. Van Tuyle, J. Guillen)

The major restructuring of MINET to model the balance of plant configurations and components has been completed. We expanded the fluids and materials properties, and extended the steam table range to allow analysis at the low operating pressure of the main condensers. Testing indicates these functions are quite accurate, i.e., 1% or less error, and they are quite acceptable for representing the low pressure portion of the balance of plant.

The MINET heat exchanger module has been modified to allow representation of a cross-flow heat exchanger. This option is expected to be useful in representing large tube-in-tank heat exchangers, including many condensers and feedwater heaters.

A turbine stage module is currently being incorporated in MINET. This module represents impulse or impulse-reaction turbine stages, and is to be used with existing valve and accumulator modules to represent the turbine, including the steam extraction for feedwater heating.

3.2 MINET Code Improvements (G.J. Van Tuyle, T.C. Nepsee)

An updated version of MINET (Version 1.3) has been constructed incorporating revisions to the input processor and computational code. All temporary coding has been removed from the input processor as of this version.

Several options for representing heat exchangers have recently been added. These will allow representation of the heat capacitance of heat exchanger structural materials, the effects of core tubes (such as those found in the EBR-II superheaters) and the behavior of cross-flow heat exchangers.

The initialization of the heat exchanger module is relatively intricate when one or both fluids pass through multiple heat transfer regimes. To aid in the iterative solution, a generalized root-finder subroutine was added, which utilized Newton-Raphson and Method of False Position schemes to provide an improved estimate of the root. The Method of False Position was only used

when the root was fully bounded, and utilized information on both sides to project an estimate of the root. After extensive applications of this root solver, it was found that the convergence is often bi-linear, i.e., discontinuities cause large differences in slope on opposite sides of the root. As a result, the Method of False Position was replaced with a bounded Newton-Raphson that projects in from whichever side the most recent point lies. Significant improvements have resulted.

A turbine stage module has recently been incorporated in MINET. Consistency tests on the new module are currently being performed.

A trial compilation of MINET was made using the CDC FTN5 compiler which implements the ANSI X3.9-1978 FORTRAN standard. The resulting diagnostic messages were reviewed to identify code revisions necessary to conform with the above standard. It is estimated that the revision process will be completed shortly.

Conceptual design has been completed for a restart capability. Implementation remains to be done.

3.3 MINET Standard Input Decks (G.J. Van Tuyle, J. Guillen)

MINET standard decks C4 and C5 are the current standard decks for one- and two-loop representations of Clinch River, using CY-41 of SSC/MINET. MINET deck E1 is the current standard deck for representing EBR-II.

The version of deck E1 for the stand-alone MINET has been used to simulate the first 10 minutes of the 8A transient, which was previously simulated with the version of MINET coupled to SSC. The results of the simulation are currently being reviewed and compared to the test data, as well as the results of the previous simulation. Results from the stand-alone MINET and from the version running with CY-41 of SSC are quite similar for deck E1, as expected.

3.4 MINET Applications (G.J. Van Tuyle, T.C. Nepsee, J. Guillen)

The version of MINET running with SSC, CY-41, is currently being used in simulating Clinch River (Decks C4 and C5) and EBR-II (Deck E1). The stand-alone version of MINET is being tested on a version of EBR-II deck E1.

We are currently considering interfacing MINET with the RAMONA code, which is used for BWR transient analysis. RAMONA contains detailed models for the thermal-hydraulic and neutronic behavior of boiling water reactors, but has no models for the portion of the plant beyond the turbine and feedwater valves. Thus, MINET would be used to extend the simulation further into the plant, much as it does when it is used with SSC. A preliminary investigation indicates that a RAMONA/MINET coupling is quite feasible. Current efforts are focused on the RAMONA code, to determine where the MINET drivers are to be called.

3.5 User Support (G.J. Van Tuyle, B. Schubert)

The version of MINET working with SSC is being used in simulating the German KNK-II facility. In this system, the steam generators can be bypassed during the transient, with heat removed (instead) through sodium to air heat exchangers. The piping and valves facilitating this bypass were incorporated into the MINET input deck and the new representation appears to be working correctly.

Work has begun on the MINET documentation. A single, major document is planned, containing model and code descriptions, a user's guide, and validation summaries. A notebook format is planned, so that the documentation can be updated whenever the code is revised.

3.6 MINET Validation (G.J. Van Tuyle)

Transient test data have been used in validation studies performed using both versions of MINET, including Version 0 (coupled to SSC, CY-41), and Version 1 (the stand-alone code). Both versions of MINET performed well, and gave nearly identical results. Figures shown here actually contain results from Version 1, as it is likely to eventually replace Version 0 in support of the SSC calculations.

The EBR-II facility is a 62.5 MW sodium cooled breeder reactor and power plant. While features of the primary system are quite different, the steam generator system is very similar to the Clinch River Plant. The EBR-II system is shown schematically in Figure 3.1.

The MINET representation is shown schematically in Figure 3.2. "MINET Standard Deck E1" is the name of the input deck that creates the component configuration as shown. The intermediate heat exchanger (IHX) shown at the left side of the drawing is not represented by MINET, but is included in the drawing as a reference point. The dashed line extending from the IHX represents a pipe that is included in MINET when it is executed in stand-alone mode so that the transient can be driven with the IHX outlet temperature. When MINET is run with SSC, in order to model the whole system, this pipe is removed from the MINET representation and is represented in the SSC calculations.

The EBR-II test transient analyzed involved a coastdown to natural circulation from 36% full power and 39% full primary flow. This test was chosen because of its reliance on decay heat removal via the natural circulation mode, a type of transient of particular significance in LMFBR systems. Test data from this transient for comparison against computer code results were made available by ANL staff.

In simulating the transient, initial conditions and boundary conditions reportedly measured at the facility were used. These include such information as the flow and temperature coming from the IHX, the feedwater flow and temperature, and the blowdown flow rate. The turbine throttle valve was closed,

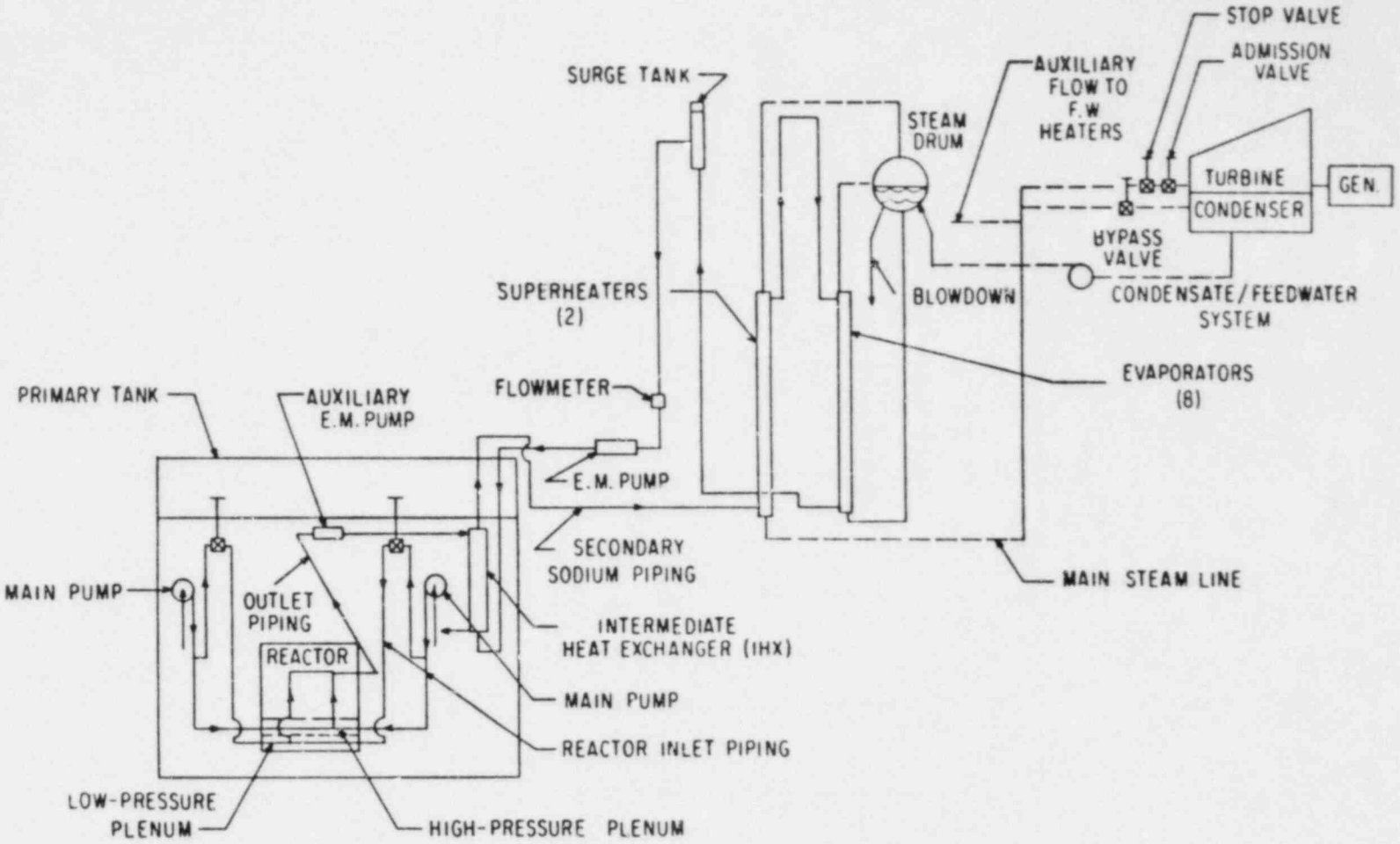

Figure 3.1 Schematic of EBR-II Plant

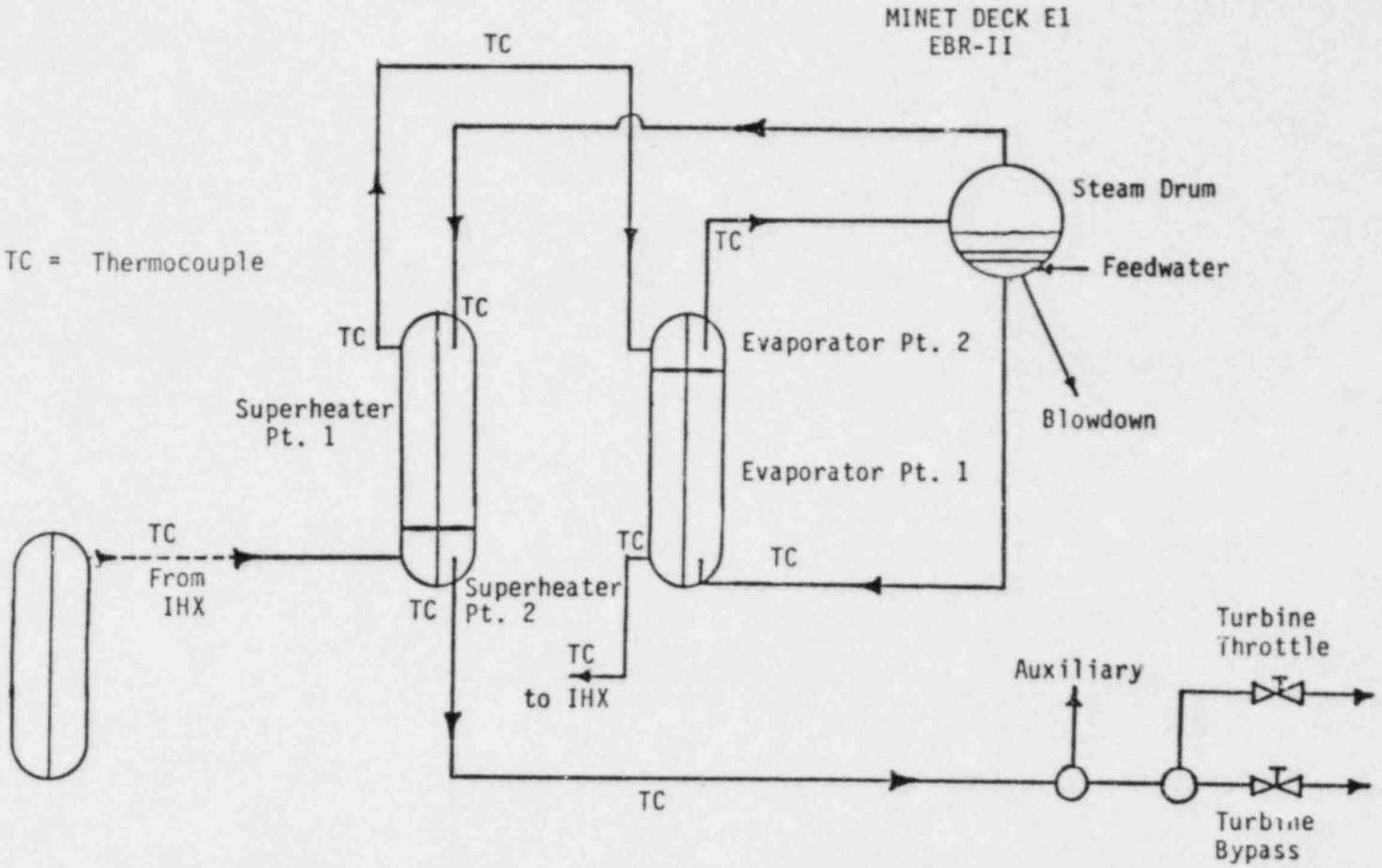

Figure 3.2 MINET Standard Deck E1. A One Loop EBR-II Deck

and the actions of the turbine bypass valve could be approximated by a simpler controller equation. The flow rate out of the auxiliary line was unknown, and could only be inferred from independent calculations that left some uncertainty remaining.

This study is discussed in detail in a formal BNL report currently being published. Two of the more interesting results are shown in Figures 3.3 and 3.4, which are the sodium temperatures entering and leaving the superheaters and evaporators, respectively. It can be seen that the MINET calculated temperatures lead those measured through the transient, which was expected because of instrumentation time constants between 10 seconds and one minute. These figures are typical of results from this comparison, where MINET accurately determined trends, but precise agreements were impossible due to uncertainty in transient boundary conditions and instrumentation response. Despite this limitation, the MINET results were consistently close to the experimental results.

REFERENCE

GUPPY, J. G., et al., (1983) "Balance of Plant Modeling," Safety Research Programs Sponsored by Office of Nuclear Regulatory Research Quarterly Progress Report, April 1 - June 30, 1983, Brookhaven National Laboratory Report to be published.

PUBLICATIONS

VAN TUYLE, G. J., GUPPY, J. G. and NEPSEE, T. C., "MINET - Transient Analysis of Fluid Flow and Heat Transfer Networks," 1983 ASME International Computers in Engineering Conference and Exhibit, Vol. 1 (Bk. No. G00230), August 1983, BNL-NUREG-32858.

VAN TUYLE, G. J., "MINET, Validation Study Using EBR-II Test Data," Brookhaven National Laboratory Report to be published.

VAN TUYLE, G. J., et al., "MINET, Balance of Plant Modeling, Code Description and User's Manual," Brookhaven National Laboratory Report to be published.

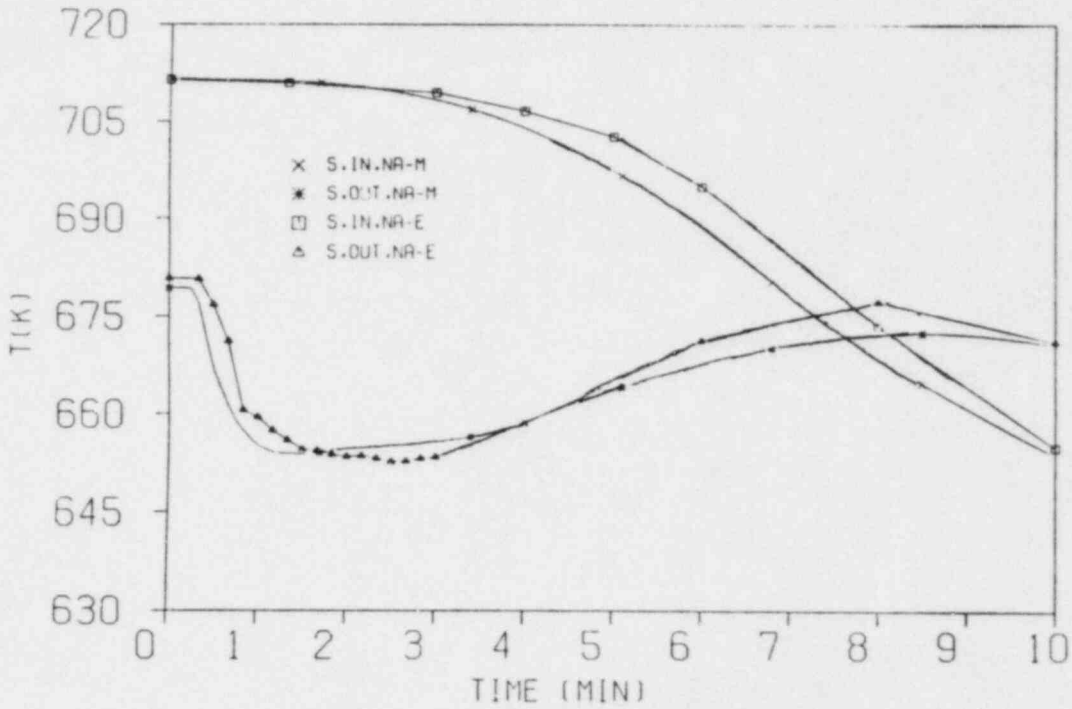

Figure 3.3 Superheater Sodium Temperatures, Inlet & Outlet
EBR-II and MINET

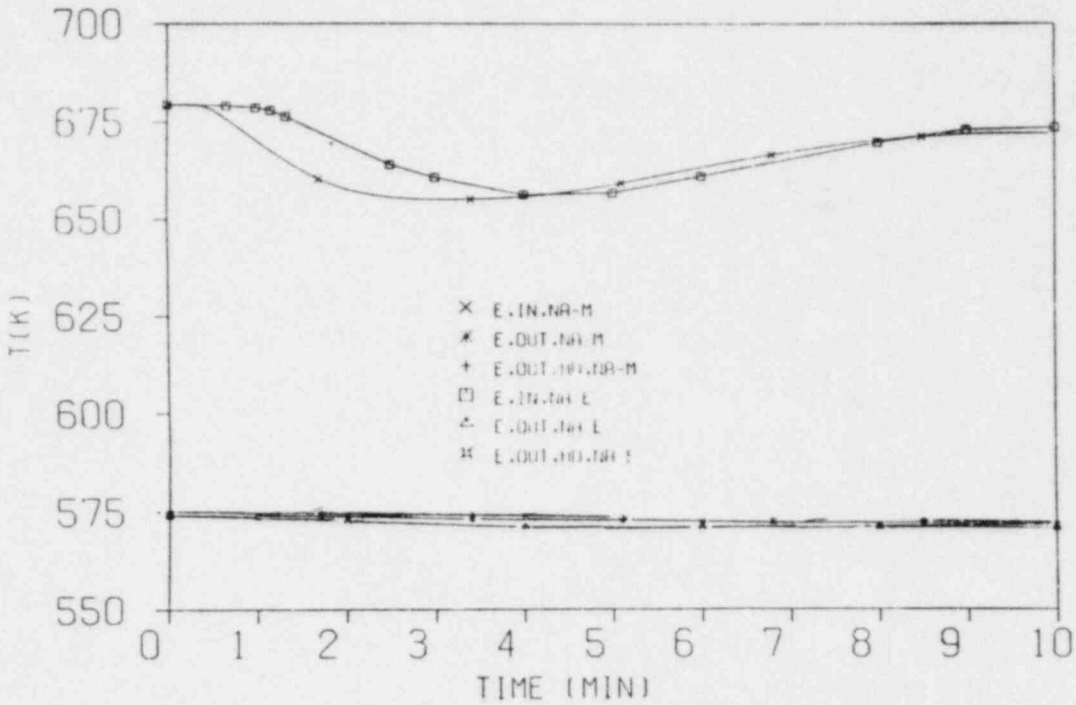

Figure 3.4 Evaporator Sodium Temperatures, Inlet, Outlet, Outlet Header EBR-II and MINET

4. Thermal Hydraulic Reactor Safety Experiments

4.1 Core Debris Thermal Hydraulic Phenomenology: Ex-Vessel Debris Quenching

(T. Ginsberg, J. Klein, J. Klages, and C. E. Schwarz)

This task is directed towards development and experimental evaluation of analytical models for prediction of the rate of steam generation during quenching of core debris under postulated LWR core meltdown accident conditions. This program is designed to support development of LWR containment codes.

4.1.1 Experimental Results

Lipinski (1983) has recently modified his model for dryout heat flux from a heated debris bed. This new version has been compared with the heat removal rates observed in the BNL debris bed quench experiments (Ginsberg, 1983).

Steam flow rate traces are shown in Figures 4.1 and 4.2. The results are compared with predictions based upon Lipinski (1980, 1983) dryout heat flux models. It is observed that the most recent version of the model provides a good estimate of the quasi-steady heat transfer during the bed quench period. The bed quench heat transfer data are shown in Figure 4.3 together with predictions based upon several models. It is observed that the data agree reasonably well with the Lipinski (1983) heat transfer prediction for all the particle sizes investigated, 0.89 mm-12.7 mm.

4.1.2 Analytical Modeling and Results

A model to characterize the debris bed quench process has been described previously (Ginsberg, 1983).

Calculations have been performed for the case of negligible steam cooling of the debris. It was assumed in this calculation that 40% of the stored energy is removed during the downward frontal propagation period. The positions of the two quench fronts vs. time are presented as consecutive line segments. The downward particle quench front is characterized by the negative slope; the upward final quench front has the positive slope. Results shown are for 1-m deep beds of 1-, 3-, and 6-mm particles which transfer heat to water at 5 bars. The initial sphere temperature is assumed to be 1723 K. Note that an "average" bed decay heat is approximately 1.5-2.0 MW/m^3 at 1% of steady-state power for a 1000 MWe power plant. Results are shown in Figures 4.4 through 4.6.

Figures 4.4 and 4.5 present the quench front propagation results based upon the Lipinski (1980) and Ostensen (1981) debris bed heat transfer models, respectively, for beds of particles of diameters 1-, 3- and 6-mm. The decay heat generation rate is assumed here to be $Q''' = 1.5\ MW/m^3$. Significant differences in quench times are observed based upon the two models, attributable to the difference in predicted bed heat flux. For 3-mm particles, for example, the calculation using the Lipinski model predicts that the downward quench front reaches the base of the bed at approximately 600 s, while the

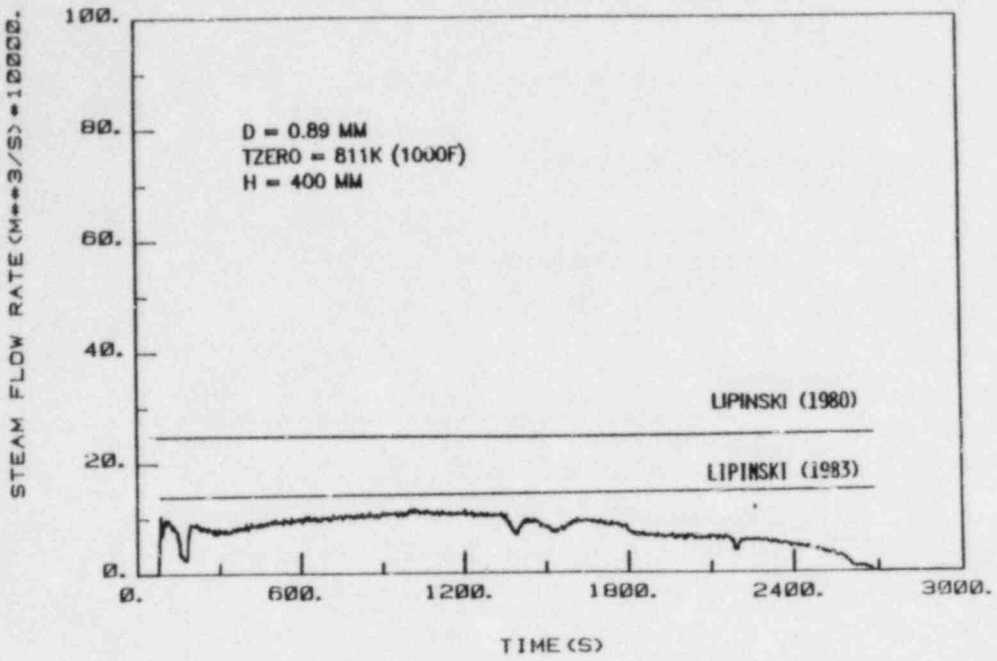

Figure 4.1 Debris Bed Quench Period Steam Flow Rate Trace.

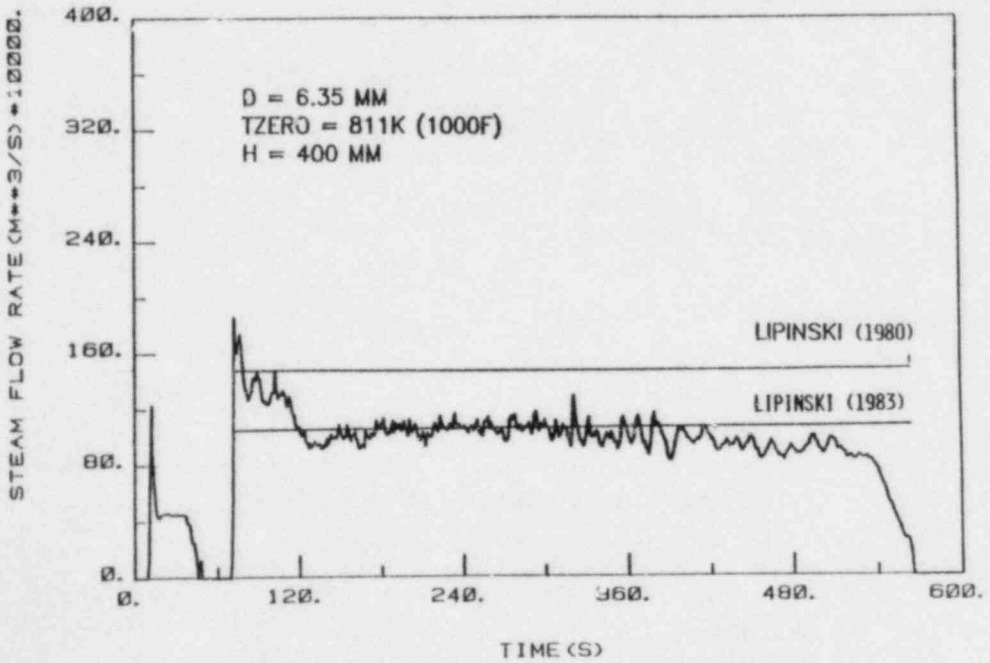

Figure 4.2 Debris Bed Quench Period Steam Flow Rate Trace.

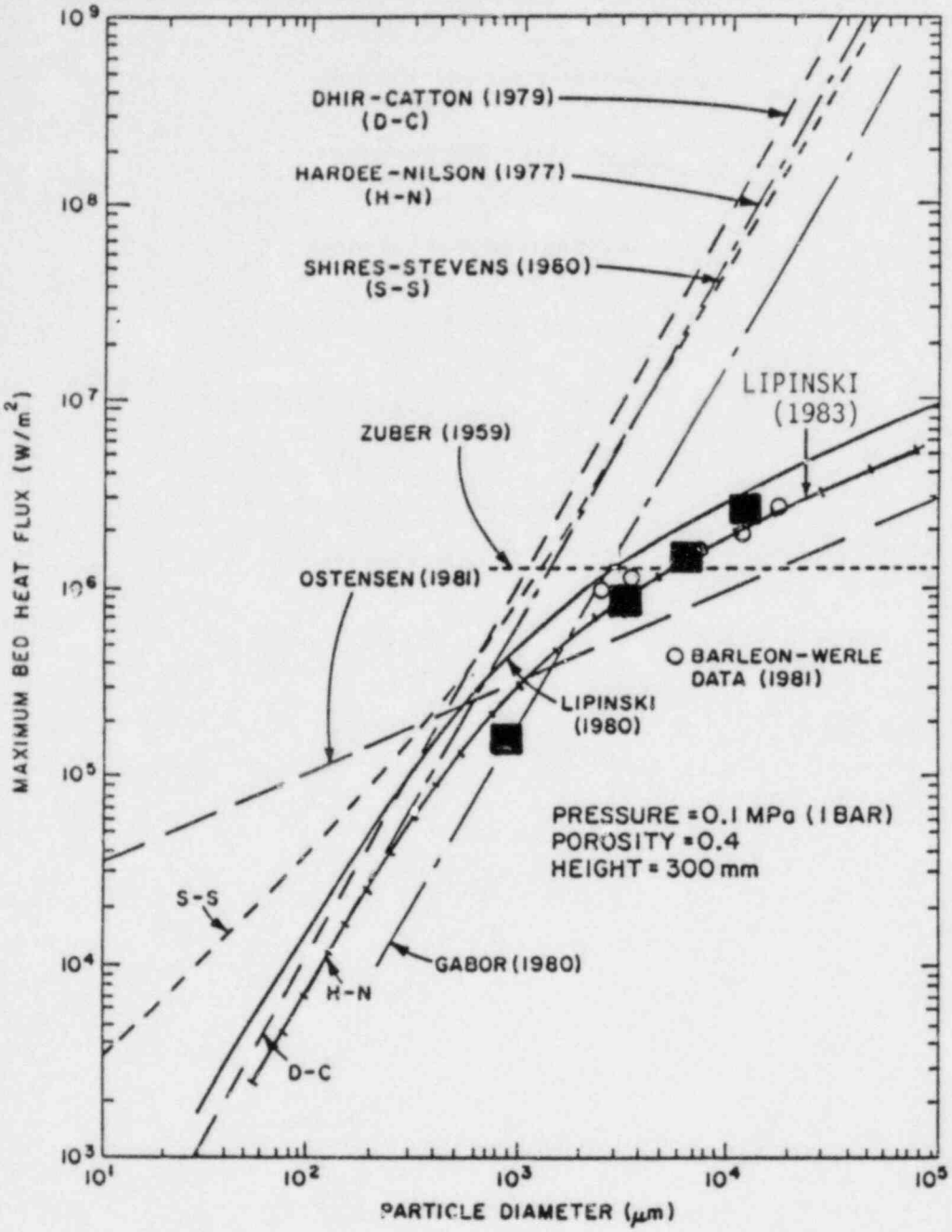

Figure 4.3 Debris Bed Quench Heat Transfer Data Compared with Dryout Heat Flux Data and Models (■ - BNL Bed Quench Data).

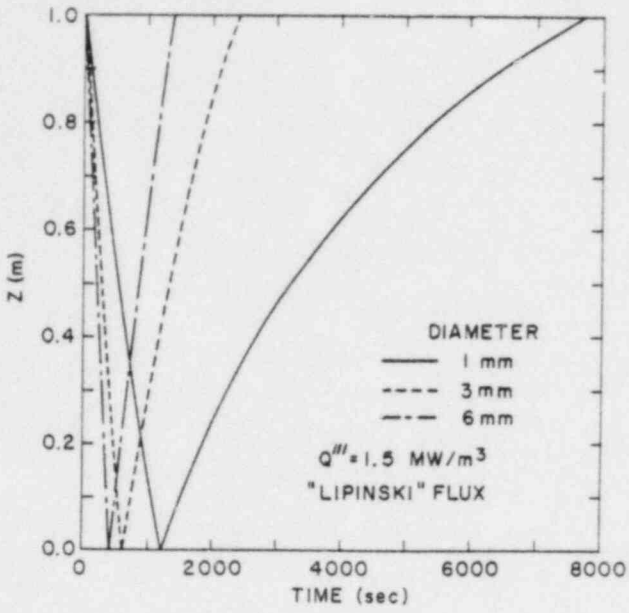

Figure 4.4 Quench Front Location vs Time Based on Lipinski Debris Bed Heat Flux; $Q''' = 1.5\ MW/m^3$; $T_o = 1723\ K$.

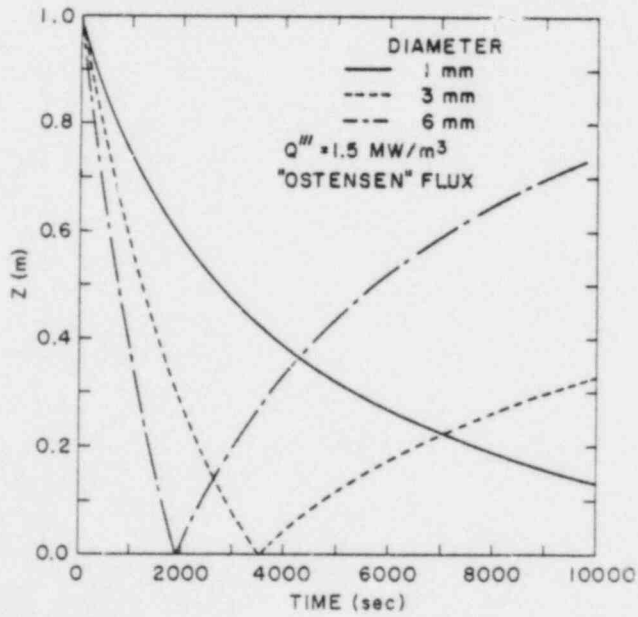

Figure 4.5 Quench Front Location vs Time Based on Ostensen Debris Bed Heat Flux, $Q''' = 1.5\ MW/m^3$; $T_o = 1723\ K$.

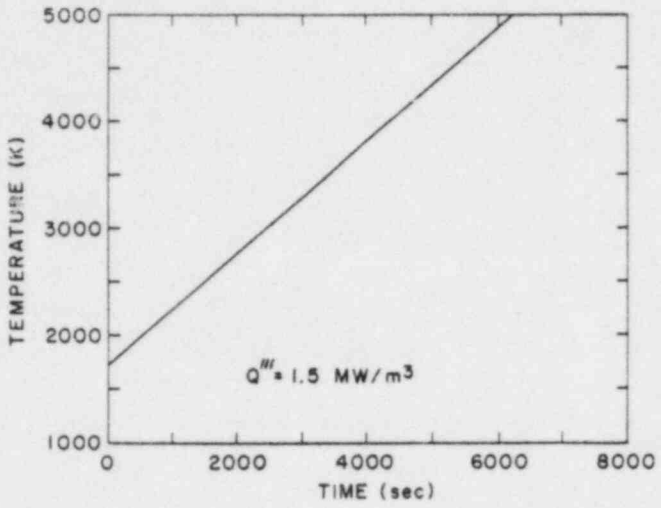

Figure 4.6 Unquenched Particle Temperature vs Time, $Q''' = 1.5\ MW/m^3$.

Ostensen calculation predicts approximately 3500 s. Similarly, the upward-directed front for the 3-mm particles advances extremely slowly based upon the Ostensen heat flux prediction as compared with the Lipinski prediction. This large difference in results is attributable partially to the smaller heat flux predicted by the Ostensen model, which leads to a longer bed quench time. The longer quench time, in turn, leads to increased stored energy due to decay heat generation which then feeds back to slow the bed quench. The temperature-time history of the unquenched particles within the bed is shown in Figure 4.6. Note that the adiabatic temperature rise rate of the debris is 0.52 K/s. It is apparent, therefore, from Figures 4.4 and 4.5 that quench times on the order of 1000 s can have significant impact on the debris bed stored energy.

The results suggest that remelting of the debris is possible during the quench process in the yet-unquenched regions of the bed. This possibility is strongly dependent on particle size, on the limiting bed heat flux, and on the decay heat generation rate. Remelting would also depend on the initial debris temperature.

4.2 Core Debris Thermal Hydraulic Phenomenology: In-Vessel Debris Quenching

(N. K. Tutu, T. Ginsberg, J. Klein, J. Klages, and C. E. Schwarz)

The purpose of this task is to develop an understanding of the transient quenching of in-vessel debris beds (formed in the reactor core region) when the coolant is injected from below. The experiments proposed would, in addition, serve as a data base for verifying the transient 1D thermal hydraulic models for the quenching process.

4.2.1 Experimental Program

A debris bed consisting of stainless steel spheres is formed in a test vessel and heated to an initial temperature. The quench is initiated by injecting water at saturation temperature through the bottom of the bed (currently at a constant flow rate).

The first series of experimental runs using 3.18 mm stainless steel spheres and constant rate injection of the coolant (water) at saturation temperature was begun and completed. A few of the results from these experiments are presented below.

Figure 4.7 shows the schematic of the experimental facility designed to perform the debris bed quenching experiments. The test section consists of a 108-mm inside diameter stainless steel tube in which the debris bed is constrained between two fixed screens to prevent fluidization. Before beginning an experimental run, the two butterfly valves are closed. The debris bed is then brought to its initial temperature by circulating hot air through it and by energizing the heater coils surrounding test section. The details of the test section instrumentation are shown in Figure 4.8. A constant displacement pump was used to inject water at a constant flow rate and at saturation temperature. The experimental parameters are listed in Table 4.1.

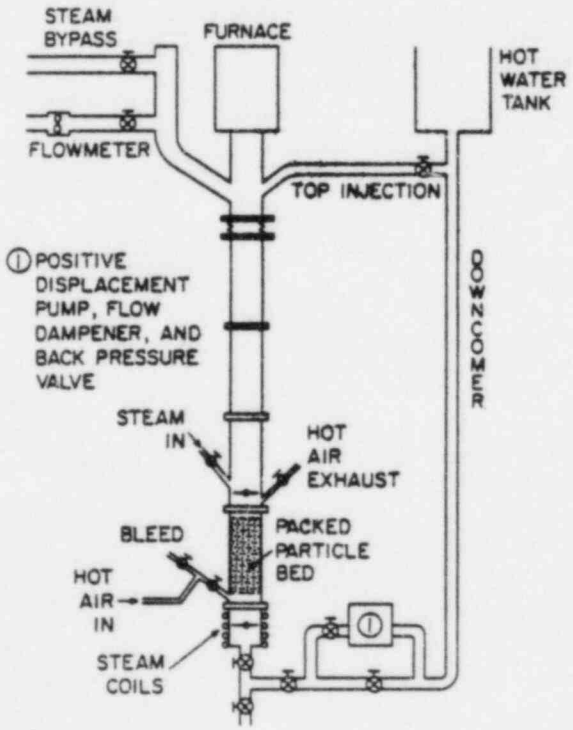

Figure 4.7 Schematic of the Core-Debris Heat Transfer Facility.

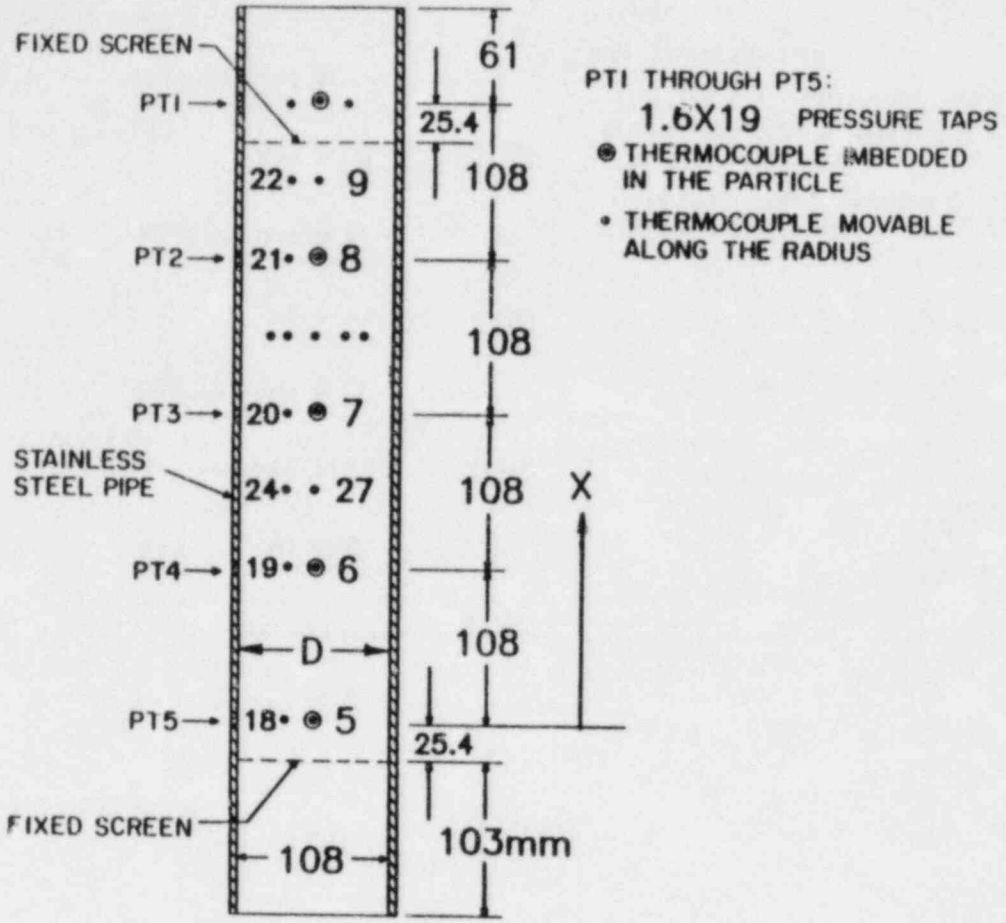

Figure 4.8 Schematic of the Test Section.

Table 4.1

Experimental Parameters

Particle material	stainless steel 302
Particle diameter	3.18 mm
Bed height	422 mm
Bed Porosity	0.4
Vessel diameter	108 mm
Initial bed temperature	770 K
Water supply temperature	373 K
System pressure	0.1 MPa
Water inlet superficial velocity (J_ℓ)	1.0 to 7.4 mm/s

During an experimental run, temperature signals from various pressure transducers and thermocouples within the bed, as well as a signal proportional to the steam flow rate at the top of the debris bed, were recorded. For small water injection rates, a typical temperature trace within the bed shows the following behavior during the quenching process. The temperature remains constant for some time, decreases slowly for a few seconds (~10 seconds), then drops sharply to the saturation temperature and remains constant thereafter. The time at which the temperature is reduced to the saturation temperature is defined as the "quench time," and it is assumed that this is also the time when a small neighborhood of the debris bed surrounding the thermocouple is quenched. For experiments conducted with a water injection superficial velocity (J_ℓ) of 1.0 mm/s at the bottom of the debris bed, it was found that the debris bed quenched in sequence from bottom to top. Thus a quench front can be assumed to travel up the bed. Figure 4.9 shows the quench front propagation plot for two experimental runs. The time to quench T_q is measured with respect to the time of arrival of the quench front at the bottom thermocouple (18 in Figure 4.8). Here H is the distance between the top and bottom thermocouple within the debris bed (22 and 18 in Figure 4.8), x is the vertical distance as measured from the bottom thermocouple location, and d is the diameter of particles in the debris bed. It is seen that the quench front travels with a reasonably uniform velocity.

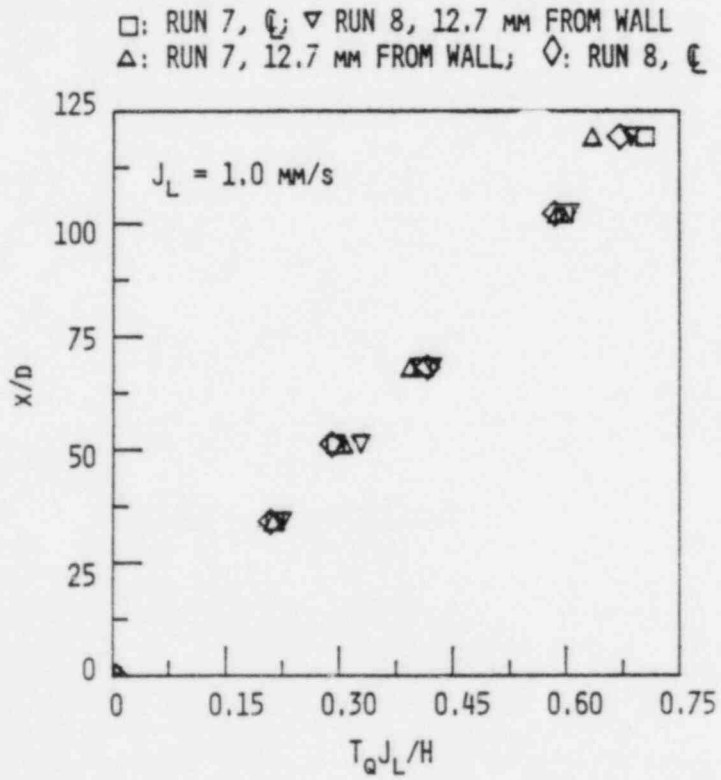

Figure 4.9 Dimensionless Quench Front Propagation Plot for J_ℓ = 1.0 mm/s.

Figure 4.10 shows the instantaneous heat flux (based on the bed cross-sectional area) leaving the top of the debris bed in the form of superheated steam as a function of time during the quenching process for two experiments conducted with identical initial conditions but with different water injection rates. For comparison, the two-phase countercurrent limit that would occur in a top flooding situation is also indicated in this figure. It is clear that the heat flux is a strong function of the water injection rate. For the case with J_ℓ = 1.0 mm/s, heat flux remains relatively constant for most of the duration of quench. However, this is not the case at the higher water injection rate corresponding to J_ℓ = 7.4 mm/s. In this case the peak heat flux (18.7 MW/m^2) is about twice the average heat flux (9.37 MW/m^2).

A detailed analysis of all the experiments conducted with 3.18 mm stainless steel spheres and constant rate injection is in progress. The results will be used for analytical modeling of the quenching process. Future plans include experiments with particles of different size and material as well as experiments with constant head injection.

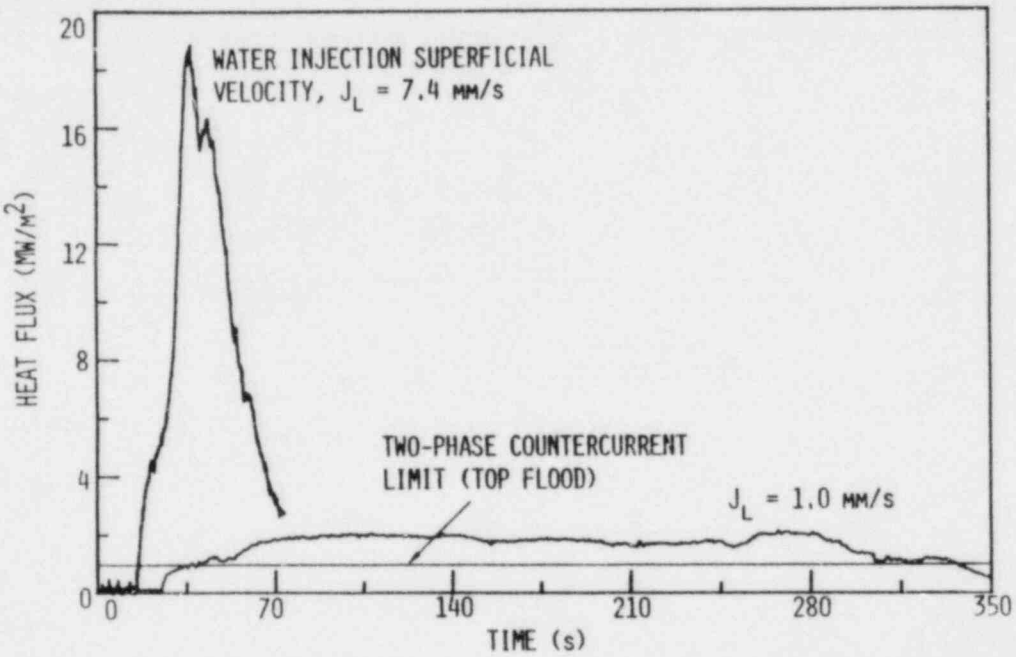

Figure 4.10 Instantaneous Heat Flux Leaving the Top of the Debris Bed with Bottom Injection of Coolant at Saturation Temperature.

4.3 Core-Concrete Heat Transfer Studies: Coolant Layer Heat Transfer (G. A. Greene and T. F. Irvine (SUSB))

The purpose of this task is to study the mechanisms of liquid-liquid boiling heat transfer and its effect on the ex-vessel attack of molten core debris on concrete. This effort is in support of the CORCON development program at Sandia National Laboratories.

4.3.1 Experimental Apparatus and Parameters

The experimental apparatus in which the liquid-liquid film boiling experiments are performed is shown in Figure 4.11. It consists of a six-inch schedule 10 stainless steel vessel, 45 centimeters high, in which to hold the high temperature melt and boiling coolant. The test section is mounted over a movable track which holds the bottom calrod heater. The heater can be slid away and a four-inch-thick base of Fibrefrax insulation can be moved into its place to insulate the test section base. The entire test section is insulated

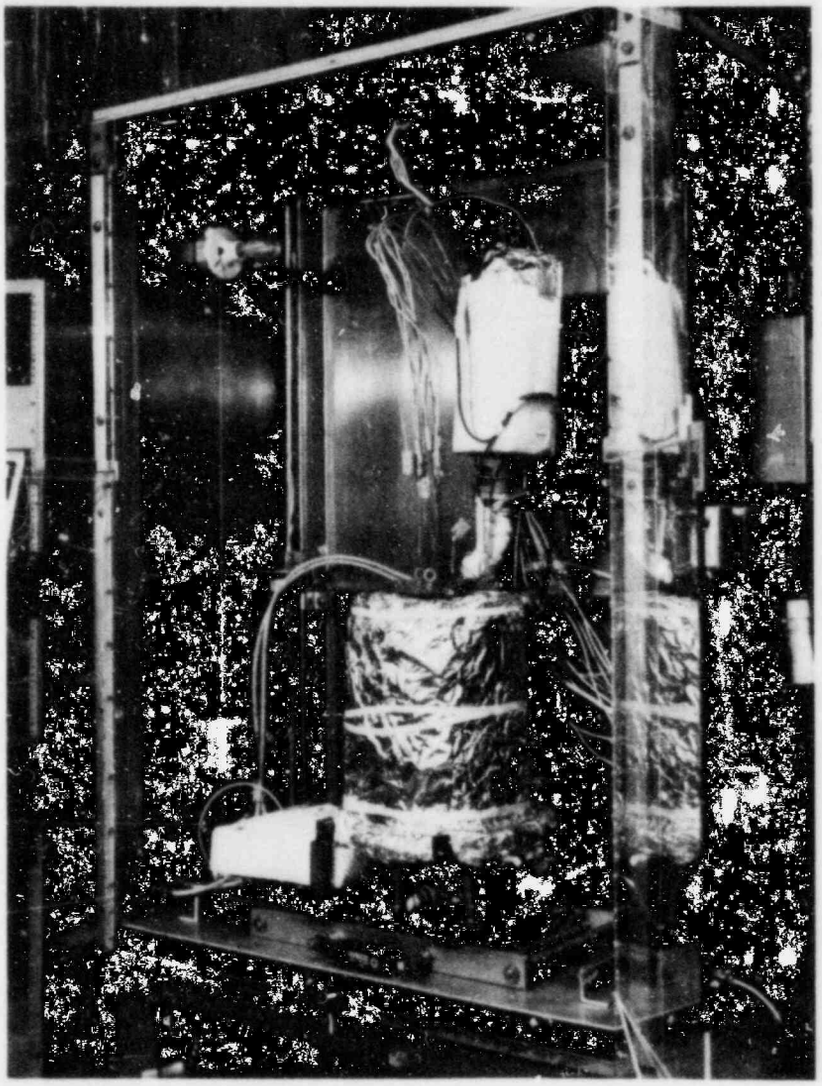

Figure 4.11 Experimental Apparatus for Liquid-Liquid Film Boiling Studies.

with a two-inch-thick blanket of similar insulation. Coolant is stored in a large capacity tank and is introduced at a controlled rate into the test section through a downcomer during the transient boiling quench to maintain a constant coolant level. A separate reservoir holds an initial coolant inventory of two liters which is dumped at the beginning of the experiment to create the initial boiling coolant pool. Both reservoirs and their piping are insulated and trace heated.

A thermocouple probe is mounted vertically inside the test section and is lowered into the liquid metal pool until an attached continuity probe detects the pool surface. The probe contains eight thermocouples, one in the coolant and seven in the melt, to measure the temperature history of the melt and coolant during the transient quench experiments. Four thermocouples near the melt-coolant boiling interface are used to calculate the transient melt surface temperature; four thermocouples submerged in the melt are used to calculate the transient enthalpy change of the melt. From these, the boiling curve for the experiments can be constructed.

The major parametric ranges used in the experiments to date are shown in Table 4.2.

Table 4.2

Experimental Parameters

Melt Composition	Bismuth, lead, Wood's metal
Coolant Composition	R11, water
Melt Depth	8 cm
Coolant Depth	10 cm
Melt Temperature	Up to 1000 K
Coolant Temperature	Saturation temperature
Data Acquisition Rate	25 Hertz
Pressure	0.1 MPa
Pool Diameter	15 cm (approximate)
Non-Condensable Gas Flux	None

The results of these experiments will be discussed in detail below.

4.3.2 Experimental Results

In the experiments performed to date, two distinctly different modes of boiling heat transfer have been observed. For the case of saturated R11 boiling on a pool of liquid metal, a very stable, quiescent interface was photographically observed between the two liquids, similar to film boiling from a polished solid surface. Quantitative data for the boiling heat flux as a function of surface superheat indicate that the liquid-liquid film boiling data for this fluid are in good agreement with the Berenson (1961) film boiling model predictions.

However, for the case of water boiling on the surface of similar liquid metals, quite different behavior has been observed. Photographic investigation revealed considerable interfacial mixing between the liquid metal and the water with no stable liquid-liquid interface. Quantitative experiments demonstrated the potential for steam explosions between liquid metal and water in layered pool geometry, with bismuth, lead, and Wood's metal. For experiments in which no steam explosion occurred and the boiling heat flux could be measured, the data exceeded the Berenson film boiling model prediction by a substantial margin.

4.3.3 R11/Liquid Metal Liquid-Liquid Film Boiling Data

A series of transient boiling experiments were performed with three different liquid metal melts and R11 as the boiling coolant. The liquid metal superheat achieved in the tests was in the range 100-600 K. The R11 (Freon 11) coolant was saturated (297 K). The data are shown in Figure 4.12. The calculated boiling heat flux from the classical Berenson flat plate film boiling is shown for reference. Excellent agreement was achieved in these tests between the measured boiling heat flux and the Berenson model predictions for flat plate film boiling. The data in Figure 4.12 represent a composite overlay of data from four separate experiments. The tendency of the data to deviate from the model in the vicinity of 300 K superheat and then return to agreement should be attributed to experimental uncertainty and not to a physical process. The observation of stable liquid-liquid film boiling (in the absence of a non-condensable gas flux from below) from the data is further substantiated by visual photographic evidence of the actual boiling interface behavior. It was observed that the liquid metal surface was perfectly flat with no waves or ripples, in spite of the active boiling-induced hydrodynamic activity in the R11 layer above. This indicates that for the case of R11 boiling on a liquid metal pool, the vapor film between the two fluids is hydrodynamically stable with no interference or feedback from the boiling layer above. No liquid-liquid contacts were observed.

Under these circumstances, it can be concluded that film boiling of R11 can be characterized by stable film boiling correlations even in the presence of a liquid surface below. Experiments to be performed in the near future will investigate the effect of blowing a non-condensable gas through the boiling interface. This will simulate the action of concrete decomposition gases during a core-concrete interaction.

4.3.4 H_2O/Liquid Metal Liquid-Liquid Film Boiling

Recently, experiments have begun with water as the boiling coolant instead of R11. The same liquid metal melts were employed. Frequently during these transient film boiling experiments, pool-geometry steam explosions occurred which would terminate the quench experiment. In all cases, these steam explosions occurred after some variable time delay with no premixing or triggering. Subcooling of the water was found to promote these events; however steam explosions did occur with saturated water as well. It was postulated that natural film boiling instabilities were promoting spontaneous film collapse and partial mixing, resulting in these pool-geometry steam explosions.

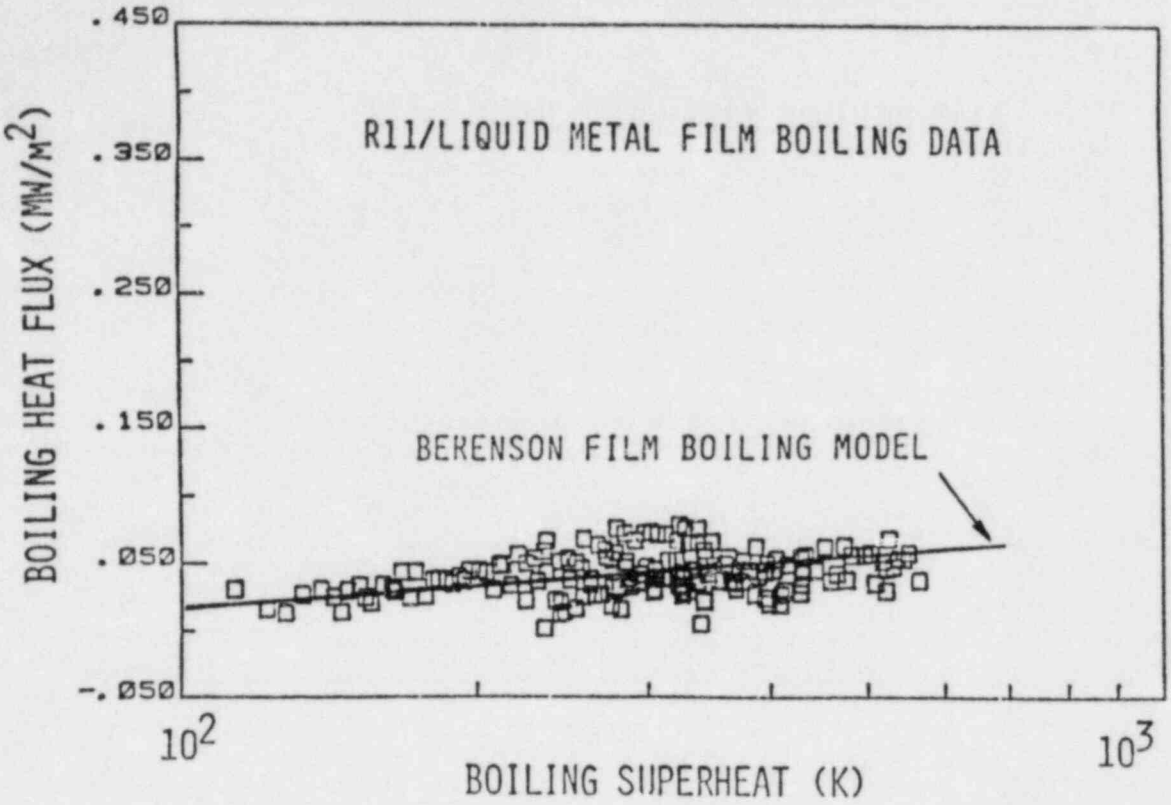

Figure 4.12 R11/Liquid Metal Liquid-Liquid Film Boiling Data.

To investigate this hypothesis, photographic visualization studies were again performed at the liquid-liquid boiling interface. What was observed was a region of intense mixing and agitation at the liquid-liquid interface with large amplitude spikes of metal splashing upwards into the water layer as much as several centimeters. No stable surface was observed between the water and liquid metal as was observed in the case of R11. This disturbed interface was evidence of spontaneous liquid-liquid contact and enhanced film boiling.

Quantitative film boiling experiments with water coolant were performed which did not result in a steam explosion. In most cases, a minor explosive "pop" still would occur which would disrupt the melt layer and disperse it. In several cases, the film boiling continued through the quench without disruption, enabling a quantitative measure of the magnitude of the unstable film boiling heat flux, similar to what was measured for R11. One such set of data is shown in Figure 4.13. Here it is evident that the boiling heat flux is significantly higher than that predicted by the Berenson film boiling model by a factor of three to five. This is also in the absence of a non-condensable gas flux through the interface which would simulate gas release from a core-concrete interaction. This deviation of the data from the Berenson film

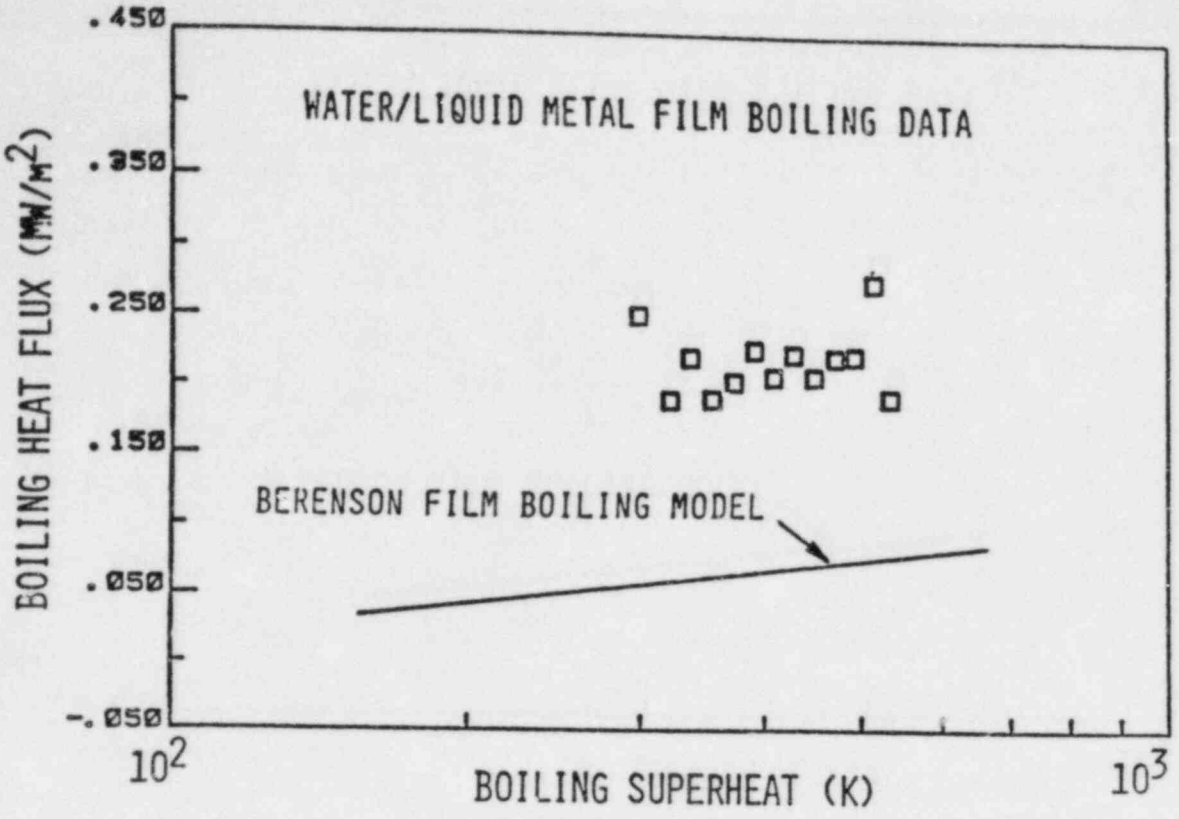

Figure 4.13 Water/Lead Liquid-Liquid Film Boiling Data.

boiling model is direct evidence of the enhancement of the heat flux by spontaneous film instability and liquid-liquid contact, the mechanism that frequently escalated into a steam explosion.

It can be concluded that film boiling of water on a molten substrate is inherently unstable, characterized by liquid-liquid contacts which enhance the boiling heat flux and frequently escalate into pool-wide steam explosions. Experiments to be performed will investigate both aspects of this mode of film boiling further.

REFERENCES

BERENSON, P. J. (1961), "Film Boiling Heat Transfer From a Horizontal Surface," J. Heat Transfer, 83, pp. 351-358 (1961).

GINSBERG, T., et al., "Measurements and Analysis of Steam Generation Rate From Quenching of Superheated Debris Beds," Trans. Am. Nucl. Soc., 44, 375 (1983).

LIPINSKI, R., et al., "Advanced Reactor Safety Research Quarterly Report, January-March 1980," Sandia National Laboratories, NUREG/CR-1594, 13, 1, 88 (April 1981).

LIPINSKI, R. J., "A Review of Debris Coolability Models," Proceedings of International Meeting on Light Water Reactor Severe Accident Evaluation, Volume 2, TS-18.2, Cambridge, MA (August 1983).

5. LWR Plant Analyzer Development
(W. Wulff)

5.1 Introduction

This program is being conducted to develop an engineering plant analyzer, capable of performing accurate, real-time and faster than real-time simulations of plant transients and Small-Break Loss of Coolant Accidents (SBLOCAs) in LWR power plants. The engineering plant analyzer is being developed by utilizing a modern, interactive, high-speed, special-purpose peripheral processor, which is designed for time-critical systems simulations. The engineering plant analyzer supports primarily safety analyses and serves also as the basis of technology development for nuclear power plant monitoring, for on-line accident diagnosis and mitigation, and for upgrading operator training programs and existing training simulators.

There were three activities started in the LWR Plant Analyzer Development Program; namely, (1) the assessment of the capabilities and limitations in existing simulators for nuclear power plants, (2) the acquisition of a special-purpose, high-speed peripheral processor suitable for real-time and faster than real-time simulation of power plant transients and (3) the development of the software for this peripheral processor.

(1) One each of operating PWR and BWR power plants and their simulators had been selected to establish the status of current real-time simulations with respect to modeling fidelity for the thermohydraulics in the Nuclear Steam Supply System (NSSS). The assessment consisted of establishing the modeling assumptions in the process descriptions for the NSSS, and of comparing NSSS-related simulator results with results from RETRAN calculations. The evaluation was performed to determine the current simulator capabilities and limitations of providing engineering predictions for operational transients and for transients caused by loss of coolant injection, by a loss of feedwater or feedwater heaters, by a loss of heat sink (steam generator failure), or by a mismatch between fission power and cooling rate.

(2) The AD10 of Applied Dynamics International (ADI) of Ann Arbor, Michigan, had been selected earlier as the special-purpose, high-speed peripheral processor on the basis of its capacity to execute faster and more efficiently the operations which are currently being performed in training simulators by general-purpose computers. Specifically, the special-purpose processor was selected for efficient, high-speed integration of ordinary differential equations and for direct, on-line interactions with the user, with instrumentation, with both digital and analog signals from other computers and with graphic devices for continuous, on-line display of a large number of computed parameters.

(3) The software development for the new peripheral processor is carried out in two phases. One phase was the implementation of an existing thermohydraulics model for a BWR system to simulate operational transients on the new processor. This phase served to compare the computing speed and accuracy of

the AD10 processor with those of the CDC-7600 main-frame computer, and thereby to demonstrate in principle the feasibility of computing realistic transients at faster than real-time computing speeds. The second phase is the modeling of the primary loop outside of the vessel and its controls, neutron kinetics and thermal conduction for the complete BWR simulation and the formulation and implementation of a thermohydraulic model for the faster than real-time analysis of operational and SBLOCA transients in PWR power plants. This is supplemented by implementation of multicolor graphics displays.

Below is a brief summary of progress made previously and a detailed summary of achievements during the current reporting period.

5.2 Assessment of Existing Simulators (W. Wulff and H. S. Cheng)

The assessment of current simulator capabilities consisted of evaluating qualitatively the thermohydraulic modeling assumptions in the simulator and of comparing quantitatively the predictions from the simulator with results from the detailed systems code RETRAN.

The results of the assessment have been published earlier in three reports (Wulff, 1980; Wulff, 1981a; Cheng and Wulff, 1981). It had been found that existing training simulators were limited to the simulation of steady-state conditions and quasi-steady transients within the parameter range of normal operations. Most currently used PWR simulators cannot simulate two-phase flow conditions in the primary reactor coolant loops, nor the motion of the two-phase mixture level beyond the narrow controls range in the steam generator secondary side. Most currently used BWR simulators cannot simulate two-phase flow conditions in the recirculation loops or in the downcomer and lower plenum, nor can they simulate coolant level motions in the steam dome, the lower regions of the downcomer (below the separators), or in the riser and core regions. These limitations arise from the lack of thermohydraulic models for phase separation and mixture level tracking (Wulff, 1980; 1981a).

The comparison between PWR simulator and corresponding RETRAN results, carried out for a reactor scram from full power, showed significant discrepancies for primary and secondary system pressures and for mean coolant temperatures of the primary side. The discrepancies were found even after the elimination of differences in fission power, feedwater flow and rate of vapor discharge from the steam dome. Good agreement was obtained between simulator and RETRAN calculations for only the early part (narrow control range) of the water level motion in the steam generator. The differences between simulator and RETRAN calculations have been explained in terms of modeling differences (Cheng and Wulff, 1981).

5.3 Acquisition of Special-Purpose Peripheral Processor (A. N. Mallen and R. J. Cerbone)

The AD10 had been selected earlier as the special-purpose peripheral processor for high-speed, interactive systems simulation. A brief description of the processor has been published in a previous Quarterly Progress Report (Wulff, 1981b). A PDP-11/34 DEC computer serves as the host computer.

Two AD10 units, coupled directly to each other by a bus-to-bus interface and equipped with a total of one megaword of memory, have been installed with the PDP-11/34 host computer, two sixty-seven megabyte disc drives, a tape drive and a line printer. On-line access is facilitated by a model 4012 Tektronix oscilloscope terminal and a six-channel signal generator. The system is accessed remotely via four ADDS CRT terminals and two DEC Writer terminals, one also equipped with a line printer. An IBM personal computer is also used to access the PDP-11/34 host computer and to generate multicolored graphs from AD10 results. An advanced multicolor graphics terminal is needed, however, for extensive on-line display of simulated parameters generated by the AD10 at real-time or faster computing speeds.

5.4 Software Implementation on AD10 Processor

A four-equation model for nonhomogeneous, nonequilibrium two-phase flow had been formulated and supplemented by constitutive relations from an existing BWR reference code, then scaled and adapted to the AD10 processor to simulate the Peach Bottom-2 BWR power plant (Wulff, 1982a). The resulting High-Speed Interactive Plant Analyzer code (HIPA-PB2) has been programmed in the high-level language MPS-10 (Modular Programming System) of the AD10. After implementing the thermohydraulics of HIPA-PB2 on the AD10, we compared the computed results and the computing speed of the AD10 with the results and the computing speed of the CDC-7600 main-frame computer, to demonstrate the feasibility of achieving engineering accuracy at high simulation speeds with the low-cost AD10 minicomputer (Wulff, 1982b).

It has been demonstrated (Wulff, 1982b) that (i) the high-level, state equation-oriented systems simulation language MPS-10 compressed 9,950 active FORTRAN statements into 1,555 calling statements to MPS-10 modules, (ii) the hydraulics simulation occupies one fourth of available program memory, (iii) the difference between AD10 and CDC-7600 results is only approximately $\pm$ 5% of total parameter variations during the simulation of a severe licensing base transient, (iv) the AD10 is 110 times faster than the CDC-7600 for the same transient, and (v) the AD10 simulates the BWR hydraulics transients ten times faster than they progress in real-time. It has been demonstrated now that even after the inclusion of models for neutron kinetics, conduction, balance of plant dynamics and controls, the AD10 still achieves ten times real-time simulation speed for all transients listed in Table 5.1 of Section 5.4.2.

The HIPA-PB2 hydraulics program used earlier for the feasibility demonstration is now being expanded to simulate neutron kinetics (point kinetics), thermal conduction in fuel elements and the thermohydraulics of the components shown in Figure 5.1.

The stand-alone program modules for neutron kinetics with feedback simulation and scram control, for thermal conduction in fuel elements, for compressible flows in the steam line and for the control logic for operating the safety and relief valves tested earlier (Wulff, 1982c; 1983) have been implemented in HIPA-PB2.

Specific accomplishments of the current reporting period are described below.

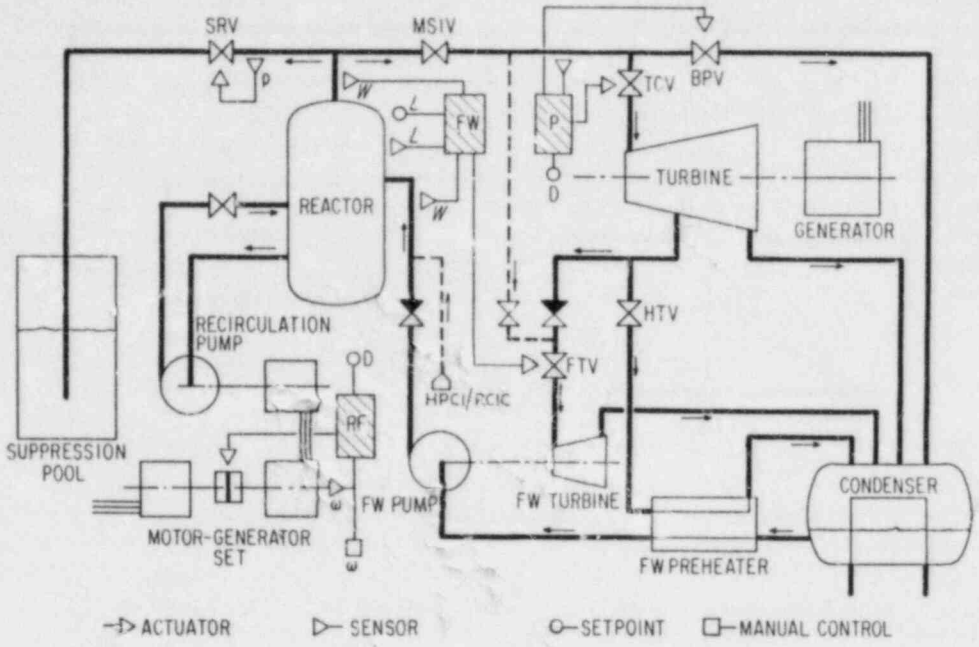

Figure 5.1 Flow Schematic and Control Blocks for BWR Simulation; FW - Feedwater Controller, P - Pressure Regulator, RF - Recirculation Flow Controller

5.4.1 Model Development (W. Wulff)

Control Systems

Models have been formulated, scaled, programmed and tested in stand-alone mode for the feedwater controller, the pressure regulator and the recirculation flow controller. The description of the control system for the BWR Power Plant, and the specification of its parameters, have been taken from the report by J. D. Milton (1982). The control system diagrams are shown in Figures 5.2, 5.3 and 5.4 for the feedwater controller, the pressure regulator and the recirculation flow controller, respectively.

The feedwater controller (Figure 5.2) receives four input signals: the level set point signal, the signal of the actual narrow-range mixture level (LEVEL) in the downcomer and the actual signals of mass flow rate from the steam just upstream of the main steam isolation valve (W_{SL}) and from the feedwater entering the pressure vessel (W_{FW}). The signal transmission delays for level and mass flow rates are simulated by three lag compensators. A change in level set point is introduced by selecting the rate of change of level (RLSP) and the time span during which this rate of change is imposed. The output of the feedwater controller, consisting of a lead-lag compensator,

a proportional-integrating controller and a lag compensator, is the control signal to the valve actuator (shaded block in Figure 5.2) which determines the stem position (SP_{FTV}) of the valve admitting steam to the feedwater pump drive turbine. The rate of change of level set point (RLSP), the signal SFWCF for initiation of feedwater controller failure (at full demand or no demand) and the signal SFTVF for initiation of feedwater turbine valve failure (wide open or stuck closed), are all entered as analog signals from the control panel. All the gains and time constants shown in the transfer function of each control block can be changed interactively from the keyboard during program execution.

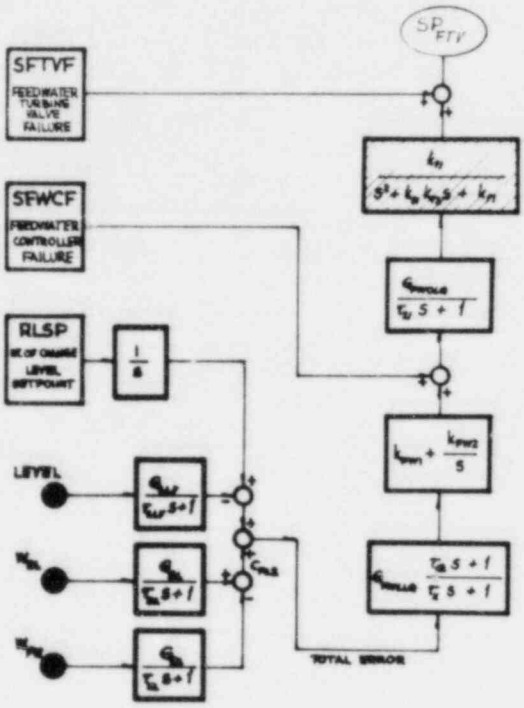

FEEDWATER CONTROL

Figure 5.2 Feedwater Controller Diagram

The pressure regulator (Figure 5.3) receives one internally computed input signal which is the turbine inlet pressure. The regulator produces three outputs, namely the two stem positions $SP_{TCV/TSV}$ and SP_{BPV} of the turbine control/stop valve and the bypass valve, respectively, and the demand error signal which is transmitted to the recirculation flow controller (Figure 5.4). There are eight analog signals accepted by the pressure regulator, as shown along the left-hand margin and in the lower right-hand corner of Figure

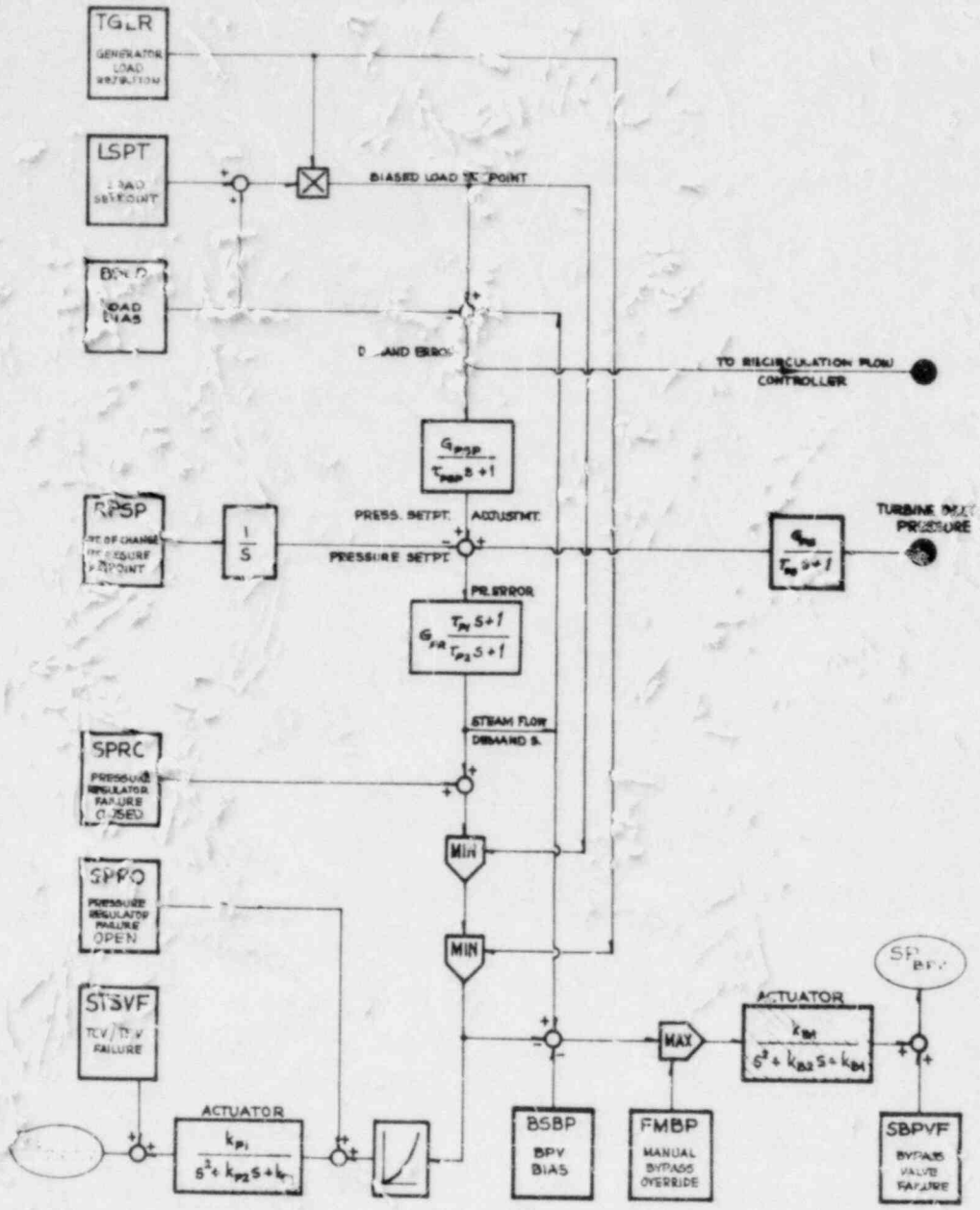

PRESSURE REGULATOR

Figure 5.3 Pressure Regulator Diagram

5.3. Two of the signals serve to change set points, five signals serve to trip failure conditions and one serves to operate the bypass valves manually. Specifically, the TGLR signal trips the condition of turbine-generator load rejection, LSPT is the load set point, RPSP defines the rate of change for the pressure set point, SPRC and SPRO, respectively, trigger pressure regulator failures at zero and full steam demand, while STSVF is used to simulate a stuck open or stuck closed turbine control/stop valve. Any negative FMBP signal maintains automatic bypass control; a positive FMBP signal overrides automatic control if FMBP exceeds the automatically called demand for bypass flow. The SBPVF signal trips bypass valve failure in wide open or closed positions. All gains (G) and time constants (τ) shown in Figure 5.3, as well as the load bias BSLD, can be changed interactively from the keyboard during program executions.

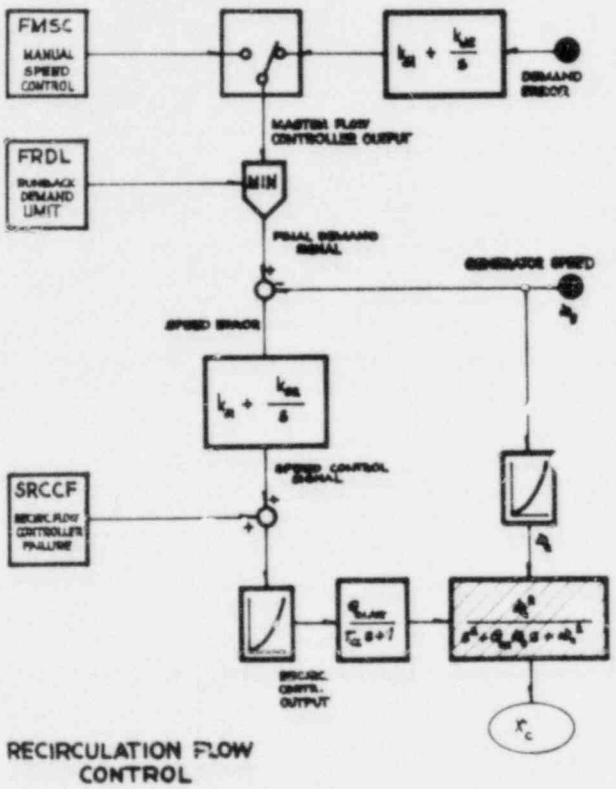

Figure 5.4 Recirculation Flow Controller Diagram

The recirculation flow controller (Figure 5.4) receives two internally computed input signals and five manual input signals. It produces one output signal, namely the scoop-tube position x_c in the fluid coupler between the drive motor and generator. The slip in the coupler depends upon this scoop tube position and determines the frequency and voltage supplied by the generator to the pump drive motor, thereby controlling the recirculation flow rate, whence the core flow rate and the coolant subcooling temperature. The subcooling temperature of the coolant affects the core void fraction and, via void feedback, the fission power in the core. The two internally computed input signals are the demand error, computed by the pressure regulator (see Figure 5.3) and the generator speed (ω_g). The three manual input signals are FMSC for manual override of the demand error, FRDL for limiting the runback demand and SRCCF for tripping the recirculation controller failure. All gains k and G, as well as the time constants τ, can be changed via keyboard commands. The coupler frequency ω_c is a specified function of the angular frequency ω_g of the generator.

When comparing the control system models of HIPA-PB2 and TRAC (Milton, 1982), notice that the HIPA control system models contain no hydraulic component models. The interface between plant components and control systems in HIPA is consistently at the actuator output for valves and for the coupler scoop tube. Plant component models have been developed separately as described below.

Plant Components

The recirculation system consists, besides the earlier simulated recirculation loop with jet pump, centrifugal pump and drive motor, of a motor-generator set and a fluid coupler. Models have been developed for predicting the rotational speeds of the generator drive motor and of the generator, respectively:

$$\frac{d\omega_{dm}}{d\tau} = \frac{(M_{el})_{dm} \cdot C_{DMG} - M_{c,l}}{I_{dm+c}} \tag{5.1}$$

Here $(M_{el})_{dm} = (M^o_{el})_{dm} \cdot f_M(\xi_{dm})$ is the electrical torque and

$$(M^o_{el})_{dm} = 48.633\ 48\ \text{kNm}, \tag{5.2}$$

is the reference torque, while

$$f_M(\xi_{dm}) = \xi_{dm}/[2.6\ \xi^2_{dm} + 0.019] \tag{5.3}$$

represents the torque characteristics of an induction motor as a function of motor slip

$$\xi_{dm} = 1 - \omega_{dm}/\omega_o \tag{5.4}$$

at constant net frequency $\omega_o = 125.6673\ s^{-1}$. The symbol C_{DMG} designates the trip signal, introduced as analog signal from the control panel:

$C_{DMG} = 1.0$ for normal operation, drive motor under power

$C_{DMG} = 0.0$ for drive motor tripped.

I_{dm+c} in Eq. (5.1) denotes the moment of inertia for the drive motor and the drive motor side of the fluid coupler. M_{c1} is the coupler torque acting on the drive motor:

$$M_{c,1} = M_{c,ref} \cdot x_c^3 \cdot \zeta(1 + |\zeta|^3) \tag{5.5}$$

Here

$$\zeta = (\omega_{dm} - \omega_g)/\omega_o \ , \tag{5.6}$$

where ω_g is the angular speed of the generator, x_c is the scoop-tube position generated by the recirculation flow controller and

$$M_{c,ref} = 2{,}330.345 \text{ kNm} \ . \tag{5.7}$$

The coupler torque as computed by Eq. (5.5) is delayed. The delay is simulated with a lag compensator with gain of unity and time constant of 0.1 second.

The generator speed ω_g in Eq. (5.6) is computed from the equation of motion

$$\frac{d\omega_g}{d\tau} = \frac{M_{c,2} - (M_{el})_g}{I_{g+c}} \ . \tag{5.8}$$

$M_{c,2}$ is the coupler torque acting on the generator and differs from M_{c1} by the coupler loss

$$M_{c,2} = M_{c1} - D \cdot \Delta M_{c,ref} \left[\frac{\omega_g(\tau)}{\omega_g(o)}\right]^2 \ , \tag{5.9}$$

where

$$\left.\begin{aligned} \Delta M_{c,ref} &= 4{,}709.73 \text{ Nm} \\ D &= 1 \quad \text{for } \omega_{dm} \geq \omega_g, \\ &= 7 \quad \text{else} \ . \end{aligned}\right\} \tag{5.10}$$

The electrical torque in the generator should be computed from the magnetic field intensity and the rotor current as obtained in a phase diagram. Since the necessary information for constructing the phase diagram is not available, $(M_{el})_g$ was computed from the power balance

$$(M_{el})_g = \frac{\omega_p}{\omega_g} \frac{(M_{el})_{pm}}{\eta_{pm}\eta_g} \tag{5.11}$$

where ω_p, $(M_{el})_{pm}$, η_{pm} and η_g represent, respectively, the angular speed of the pump-motor assembly, the electrical torque of the pump motor, the pump motor efficiency and the generator efficiency. The pump speed ω_p is computed from

$$\frac{d\omega_p}{d\tau} = \frac{(M_{el})_{pm} - M_{hyd}}{I_{pm+p}} \tag{5.12}$$

where J_{pm+p} is the moment of inertia for the pump-motor assembly. The hydraulic torque M_{hyd} is taken from Eq. 161 on page 2-36 of the report by Linford (1973). This equation is not reproduced here because it contains proprietary information. The electrical torque $(M_{el})_{pm}$ in Eqs. (5.11) and (5.12) is computed from

$$(M_{el})_{pm} = (M^o_{el})_{pm} \cdot f_M(\xi_{pm}) \cdot CRCP \tag{5.13}$$

where

$$(M^o_{el})_{pm} = 20{,}465.9 \text{ Nm} \tag{5.14}$$

and f_M is given by Eq. (5.3), evaluated with

$$\xi_{pm} = 1 - \frac{2}{3}\frac{\omega_p}{\omega_g} . \tag{5.15}$$

The ratio 2/3 in Eq. (5.15) accounts for the ratio of the number of magnetic poles in generator and pump motor. The efficiencies in Eq. (5.11) are approximated by

$$\eta_g = 0.9 \tag{5.16}$$

and

$$\eta_{pm} = 1.060\,321\,\xi_{pm}^{1/10}(1 - \xi_{pm})^{1/4} . \tag{5.17}$$

Equation (5.17) produces a typical maximum $(\eta_{pm})_{max} = 0.86$ at $\xi_{pm} = 1/3$ and $\eta_{pm} = 0$ for $\xi_{pm} = 0$ and $\xi_{pm} = 1$. The coefficient CRCP in Eq. (5.13) serves to trip (uncouple) the recirculation pump from the control panel (analog signal):

$$\begin{aligned} CRCP &= 1 \quad \text{normal operation} \\ &= 0 \quad \text{tripped.} \end{aligned} \tag{5.18}$$

5.4.2 Model Implementation (H. S. Cheng, W. Wulff, A. N. Mallen and S. V. Lekach)

The models for the balance of the plant (see Figure 5.1) and for the control systems have been coded, implemented and tested as stand-alone modules. A complete HIPA-PB2 code assembly has been completed and is ready for check-out. A summary of all the component trips currently implemented is shown in Figure 5.5. The systems simulated in HIPA-PB2 at this time will enable the plant analyzer to simulate all the transients shown in Table 5.1.

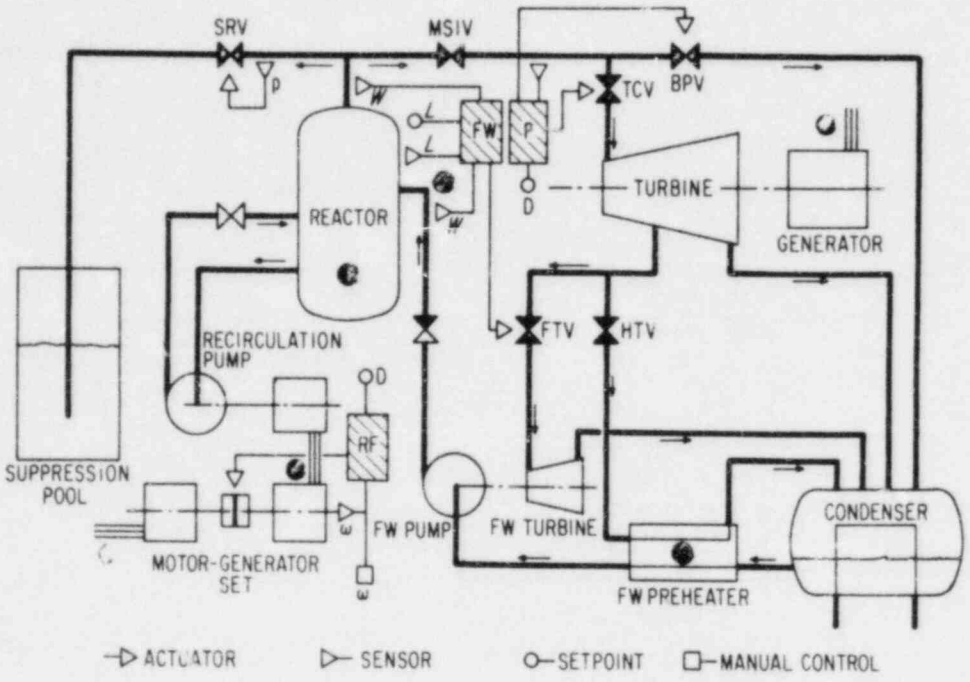

Figure 5.5 Component Trips Summary
(Shaded circles and valves)

5.4.3 Hardware Improvements (C. E. Schwarz, D. Morris and R. J. Cerbone)

A larger control panel with thirty-two channels has been constructed to manipulate or trip control systems and to change set points on-line during simulations. All channels are interrogated by the AD10 two hundred times per second. Indicator lights are being used to facilitate the recognition of control switch positions.

COP memory in the AD10 has been expanded from 1024 words to 2048 words. This expansion allows us to address now 28 input channels and 16 output channels.

Table 5.1

Simulation Capabilities

A. Transients with System Pressure Rise

1. Generator Load Rejection
2. Turbine Trip without Bypass Flow
3. Turbine Trip with Bypass Flow
4. Closure of Main Steam Isolation Valve

B. Transients with Moderator Temperature Decrease

5. Inadvertent Feedwater Pump Start-up
6. Feedwater Controller Failure, Maximum Demand
7. Feedwater Heater Loss
8. RHRS Inadvertently Started
9. HPCIS and/or RCIS Inadvertently Started

C. Transients with Reactivity Changes

10. Scram or Scram Failure
11. Control Rod Drop
12. Continuous Control Rod Removal

D. Transients with Loss of Inventory

13. Loss of Feedwater Flow
14. SRV Stuck Open, any Bank or Combination of Banks
15. Pressure Regulator Failure
16. Loss of Auxiliary Power to M/G Set

E. Transients with Change in Core Flow

17. Recirculation Pump Control Failure
18. Recirculation Pump Trip
19. Inadvertent RCP Start-up
20. RCP Seizure

5.5 Multicolor Graphic Displays (S. V. Lekach)

Work has been continued to generate labelled plots, displaying selected parameters as functions of time.

An IBM Personal Computer XT with a 10-megabyte hard disk, a four-color monitor with 640 x 200 addressable dots with associated double-capacity color graphics board, extra RAM memory and an analog to digital converter interface had been obtained earlier. The IBM Personal Computer serves to supplement the Model 4012 Tektronix storage oscilloscope, which cannot generate labelled curves and to define the specifications for later acquisitions of more powerful graphics capabilities.

The IBM Personal Computer accepts now simultaneously and on-line fifteen parameters and time from the AD10. Any set of fifteen parameters can be associated with the fifteen available output channels. Any one of the fifteen output parameters can be displayed on-line, the other fourteen afterwards from memory.

However, the IBM Personal Computer, in its current configuration, is too slow to display the high-frequency content of AD10 output at real-time simulation speed, certainly not at the possible simulation speed of ten times faster than real-time. Acceptable results can be obtained at about 1/5 of real-time speed.

Work is continuing to establish a file of frequently needed diagrams (labelled axes) which can be called for displaying selected parameters from memory. The IBM Personal Computer is programmed to accept nine parameters on-line and then to display one at a time from memory. It takes approximately forty seconds to display the first graph after the AD10 simulation is completed.

5.6 Future Plans

Work will continue to check out the overall assembly of HIPA-PB2 and to verify the systems response to the manual controls. Graphic displays will be generated for the twenty transients comprising the current simulation capabilities of the model implemented in HIPA-PB2.

REFERENCES

CHENG, H. S. and WULFF, W., (1981), "A PWR Training Simulator Comparison with RETRAN for a Reactor Trip from Full Power," Informal Report, BNL-NUREG-30602, Brookhaven National Laboratory, September 1981.

LINFORD, R. B., (1973), "Analytical Methods of Plant Transient Evaluations for the General Electric Boiling Water Reactor," NEDO-10802, General Electric Company.

MILTON, J. D., (1982), "TRAC-BWR Control Systems Model, Developmental Assessment," Internal Technical Report No. WR-CD-82-073.

VAVRA, M. H., (1960), Aero-Thermodynamics of Flows in Turbomachines, J. Wiley & Sons, New York & London, 1960.

WULFF, W., (1980), "PWR Training Simulator, An Evaluation of the Thermohydraulic Models for its Main Steam Supply System," Informal Report, BNL-NUREG-28955, September 1980.

WULFF, W., (1981a), "BWR Training Simulator, An Evaluation of the Thermohydraulic Models for its Main Steam Supply System," Informal Report, BNL-NUREG-29815, Brookhaven National Laboratory, July 1981.

WULFF, W., (1981b), "LWR Plant Analyzer Development Program," Ch. 6 in Safety Research Programs Sponsored by the Office of Nuclear Regulatory Research, Quarterly Progress Report, April 1-June 30, 1981; A. J. Romano, Editor, NUREG/CR-2231, BNL-NUREG-51454, Vol. 1, No. 1-2, 1980.

WULFF, W., (1982a), "LWR Plant Analyzer Development Program," Ch. 5 in Safety Research Programs Sponsored by the Office of Nuclear Regulatory Research, Quarterly Progress Report, January 1-March 31, 1982; A. J. Romano, Editor, NUREG/CR-2331, BNL-NUREG-51454, Vol. 2, No. 1, 1982.

WULFF, W., (1982b), "LWR Plant Analyzer Development Program," Ch. 5 in Safety Research Programs Sponsored by the Office of Nuclear Regulatory Research, Quarterly Progress Report, July 1-September 30, 1982; compiled by Allen J. Weiss, NUREG/CR-2331, BNL-NUREG-51454, Vol. 2, No. 3, 1982.

WULFF, W. (1982c), "LWR Plant Analyzer Development Program," Ch. 5 in Safety Research Programs Sponsored by the Office of Nuclear Regulatory Research, Quarterly Progress Report, October 1-December 31, 1982; compiled by Allen J. Weiss, NUREG/CR-2331, BNL-NUREG-51454, Vol. 2, No. 4, 1982.

WULFF, W., (1983), "LWR Plant Analyzer Development Program," Ch. 5 in Safety Research Programs Sponsored by the Office of Nuclear Regulatory Research, Quarterly Progress Report, January 1-March 31, 1983; compiled by Allen J. Weiss, NUREG/CR-2331, BNL-NUREG-51454, Vol. 3, No. 1, 1983.

6. LWR Code Assessment and Application

(P. Saha, U. S. Rohatgi, J. H. Jo, C. J. Hsu, H. R. Connell, C. Yuelys-Miksis, G. Slovik, L. Neymotin and J. Pu)

This project includes independent assessment of the latest released versions of the TRAC and RELAP5 codes, and application of these codes to the simulation of plant accidents and/or transients. Since no new versions of these codes have been released recently, more emphasis was placed on the code application area. Specifically, the RESAR-3S large break LOCA study and the BWR/4 MSIV closure ATWS analysis are the prime ongoing tasks under this project.

The details of the progress achieved during the reporting period of July to September 1983 are described below.

6.1 Code Assessment

6.1.1 Analysis of Oak Ridge Post-CHF Tests with TRAC-PF1 (U. S. Rohatgi and J. Pu)

A series of high pressure and high temperature steady state and transient experiments were conducted with water flowing upwards through an 8 x 8 rod bundle at Oak Ridge National Laboratory (ORNL). The details of these tests were given in an earlier quarterly report (Neymotin, 1983). A steady-state post CHF test (Run No. 3.07.9H) was selected for simulation with the TRAC-PF1 (Version 7) code. The same test was modeled earlier with the TRAC-BD1 (Version 12) and RELAP5/MOD1 (cycle 14) codes. The nodalization and initial conditions in all three simulations were identical and have been described earlier (Neymotin, 1983).

Figure 6.1 shows the comparison between the predicted rod bundle surface temperature and the experimental data averaged over a group of rods. TRAC-BD1 showed good agreement with the data. However, RELAP5/MOD1 and TRAC-PF1 both predicted early CHF which led to higher rod surface temperature downstream of the CHF point. All three codes used different correlations for the CHF point. TRAC-BD1 used the Biasi critical quality-boiling length correlation while TRAC-PF1 and RELAP5 used the Biasi local CHF correlation and the modified Zuber correlation, respectively. It should be noted that at low flow rates, significant vapor superheating develops downstream of the CHF location. This causes the rod surface temperature to continuously increase downstream of the CHF location as shown in Figure 6.1. TRAC-BD1 and TRAC-PF1 reproduce this vapor superheating phenomenon quite well. However, RELAP5/MOD1 does not predict any vapor superheating until all the droplets in the post-CHF region have completely evaporated and this explains why the RELAP5 rod surface temperature decreases in the post-CHF region. Clearly, the RELAP5/MOD1 heat transfer package including the non-equilibrium phase change rate in the post-CHF regime needs improvement. It is our understanding that the heat transfer package of RELAP5 has been changed extensively and the newer version of the code should better predict this test.

6.2 Code Application

6.2.1 LOCA Analysis of Westinghouse RESAR-3S Plants (U. S. Rohatgi and C. Yuelys-Miksis)

In the previous quarterly report (Yuelys-Miksis, 1983), it was mentioned that two input decks for the Westinghouse RESAR-3S 4-loop plant were received from LANL and INEL. The deck from LANL was for TRAC-PF1, whereas that from INEL was for TRAC-PD2. These decks were compared and some differences in the plant dimensions were found. Westinghouse engineers had helped in developing both of these decks and they conveyed to us that the plant dimensions provided to LANL were the latest and more accurate. Therefore, we decided to take the important plant information from the LANL deck and modified the INEL deck accordingly. Furthermore, it was decided to use the TRAC-PD2/MOD1 code as this was the latest released version of the TRAC-PWR codes which had been extensively assessed for large break LOCA conditions.

In the first attempt, the INEL deck was run as received and the results matched with the INEL results. However, it was found that the TRAC-PD2 generally overpredicted the subcooled choking flow rate. The code does not have a separate break flow model and the choking was predicted at the junction of the broken PIPE component and BREAK component, where an explicit numerical scheme is used. This was corrected by using a guideline recently suggested by LANL. This guideline consisted of making the diameter of the last cell three times the actual diameter of the pipe. This modification shifted the choking point from the junction of the broken PIPE component and BREAK component to the interior of the PIPE component where an implicit numerical scheme was used. This change reduced the subcooled choking flow rate by $\sim$ 20%. However, it only delayed the time of CHF slightly. The peak clad temperature (PCT) was unchanged (860°K or 1088°F) and it occurred during the blowdown phase.

In the next calculation, the fuel conditions used in the LANL deck were incorporated into the INEL deck to study the sensitivity to fuel conditions. The peak clad temperature dropped to 826°K from the original INEL prediction of 858°K. This is to be expected since the total peaking factor in the LANL deck was 1.55 in comparison to 1.65 in the INEL deck. This PCT is still different from the LANL prediction of about 811°K using the TRAC-PF1 code. This could be attributed to code differences and the way the VESSEL component was modeled in the two decks. The bypass region was simulated by a set of bypass pipes in the INEL deck while in the LANL deck, a separate annular ring was used. Furthermore, the loss coefficients and the nodalization were also different. Since incorporating the loss coefficients, which are location dependent, from the LANL deck into the INEL deck would be less accurate it was decided to simplify the LANL VESSEL module and incorporate it into the INEL deck. This produced a TRAC-PD2 input deck for the RESAR-3S plant which is also in agreement with the Westinghouse staff recommendations. The new VESSEL module now has 224 cells in comparison to 180 in the INEL deck and 544 in the LANL deck. The total number of cells including the VESSEL module is now 556.

The BNL best-estimate calculation has been performed with this modified TRAC-PD2 deck now designated the BNL deck. The peak clad temperature again occurred in the blowdown phase and it was 800.5K which is slightly lower than LANL's prediction of the peak clad temperature with TRAC-PF1. This best-estimate calculation has been run up to approximately 30 seconds and required approximately seventeen (17) CPU hours on the BNL CDC-7600 computer. The clad temperatures for the hot pins during the transient calculation so far were always lower than the first peak clad temperature which occurred at around 2.5 seconds. Figure 6.2 shows the clad temperature for one of the hot rods. The clad temperature started increasing after the first cool down which was due to flow reversal at the core inlet. The clad temperature started decreasing again due to rewet from the upper plenum. This second peak in clad temperature was lower than the first peak. The final rod cool down began when the core entered into the reflood phase at around 30 seconds.

A second calculation is being performed with additional modifications to the BNL deck in order to assess the modeling conservatisms built into Appendix K of 10CFR50. The initial and boundary conditions that were used in the Westinghouse licensing calculation with reactor pumps tripped are imposed in this calculation. Therefore, this calculation will indicate the degree of conservatism in the estimation of peak clad temperature by comparing the results of an advanced best-estimate systems code such as TRAC-PD2 with those obtained from an evaluation model code. The plant conditions such as fuel, containment pressure, safety injection and accumulator inventory were the same as those used in the Westinghouse licensing calculation.

The fuel arrangement in the Westinghouse calculation consisted of a hot pin in a hot channel and the rest of the core in a second channel. Some cross-flow was allowed between these two channels. On the other hand, the TRAC-PD2 vessel has a three-dimensional cylindrical arrangement. The fuel rods were arranged in eight sections; the only way to impose the same arrangement used in the Westinghouse calculations would be to have four inner cells of the same size as the Westinghouse hot channel. However, this would require major changes in the nodalization; furthermore, the inner cylinder in the VESSEL module would be very small. This problem was resolved by making one quadrant of the inner cylinder represent the hot channel with the average rods in the other core sections. The hot pin in the hot quadrant would interact with hotter fluid and it would thus conform to the most conservative situation as required by the Appendix K assumptions.

Another difficulty arose when incorporating the friction torque model for the Reactor Coolant (RC) pumps in TRAC-PD2 as supplied by Westinghouse for the pump coastdown calculation. The TRAC-PD2 friction torque model is given as:

$$\tau_{fr} = \tau_f + C|\Omega|\Omega/\Omega^2_{ref}$$

where τ_f and C are friction torque and a constant for bearing and winding friction torque, respectively. This model will have a friction torque even when the pump is not running. Westinghouse (1973) supplied the following form for the friction torque:

$$\tau_{fr} = A\,(\Omega/\Omega_{ref}) + B\,|\Omega|\,\Omega/\Omega^2_{ref}$$

The TRAC-PD2 code required some updates in order to include this description for the friction torque.

This second calculation has been run for 28.57 seconds and could not proceed any further due to oscillations in the cold leg components, requiring time steps smaller than 10^{-6} seconds and more than 15 outer iterations. Safety injection has not yet started due to the Westinghouse-specified 25 second delay between safety injection and reception of the safety injection signal triggered when the pressure in the pressurizer is reduced to below 121.337 bar. However, the accumulator flow into the cold leg had started. One possible cause of these oscillations could be due to the lack of an external driving momentum towards the vessel because of the RC pump trip and delay in the safety injection flow. The peak clad temperature so far occurred in the blowdown phase and was 999.2°K (1307°F). The hot pin having this peak clad temperature has not yet cooled and the clad temperature was still 988°K (1287°F) at 28.57 seconds.

6.2.2 BWR/4 ATWS Calculations Using TRAC-BD1 and RAMONA-3B Codes (C. J. Hsu, L. Neymotin, J. H. Jo and H. R. Connell)

To explore the causes for the anomalous feedwater ramp-down rate and the recirculation pump coastdown rate observed in the earlier TRAC-BD1 ATWS calculation (Hsu, 1983) using the automatic control system, a thorough review of the TRAC-BD1 automatic control block diagram and control parameters was undertaken. This also included a detailed comparison with the Browns Ferry control system logic and control block constants used in the RETRAN and RELAP5 code calculations. It was discovered that the relatively slow coastdown of the recirculation pumps was due to a couple of input errors in the block constants associated with the recirculation coupler torque dynamics and coupler frictional losses. Correction of these input errors resulted in a significant improvement of the recirculation pump coastdown characteristic when either the pump-motor or the motor-generator set of the recirculation pumps was tripped. Tripping the motor generator set showed a relatively large coastdown time constant as compared to tripping the pump-motor; however, the coastdown curves for the two cases eventually merged.

The rapid ramp-down of the feedwater flow rate following the MSIV closure is attributed to the feedwater flow pressure correction factor used to account for the effect of feedwater line pressure on the feedwater pump flow. Previously, this feedwater pump shut-off head was set to be 1255 psia. This caused the rapid ramp-down of the feedwater because the earlier TRAC-BD1 calculations showed that the reactor pressure reached 1255 psia within a few seconds. The cause for this relatively high reactor pressure predicted in the TRAC-BD1 calculation was found to be due to incorrect input data in the relief-and-safety valve lines flow area and the valve flow area. Several test runs were performed to determine the valve flow area such that valve discharge rate is correct when the set pressure is reached.

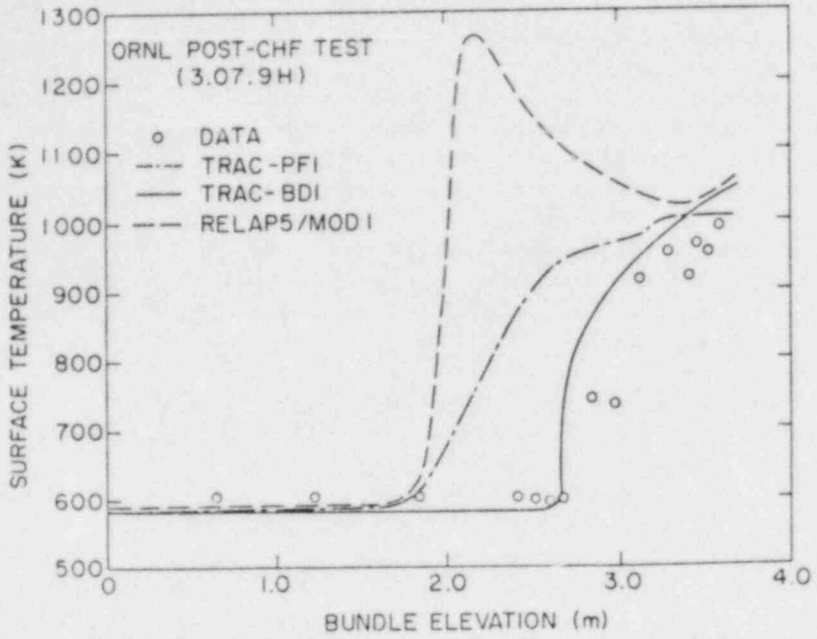

Figure 6.1 Comparison Between the Experimental Data and Code Predictions for ORNL Post-CHF Test 3.07.9H.

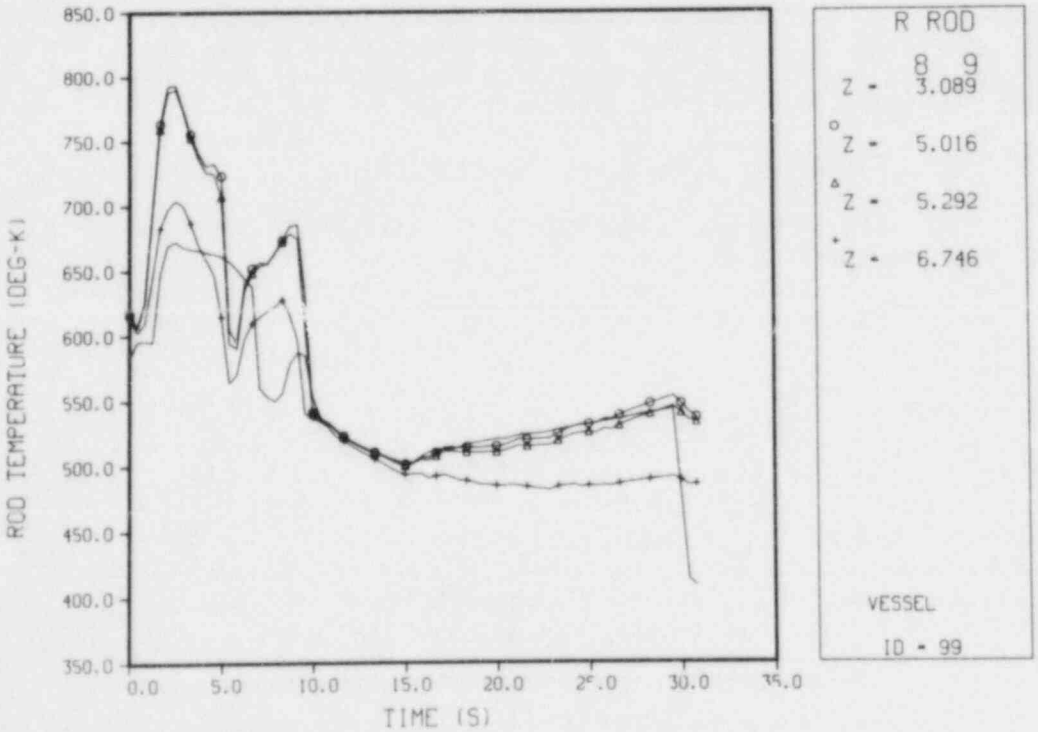

Figure 6.2 Calculated Hot Rod Surface Temperature for the RESAR-3S Best-Estimate Large Break LOCA Analysis.

After correcting all the input errors mentioned above, a new 200 second MSIV closure ATWS calculation was carried out using the automatic control system option. Some of the results, such as the normalized reactor power and the steam dome pressure, are illustrated in Figures 6.3 and 6.4, respectively. The peak steam dome pressure is seen to be about 9.37 MPa (1360 psia) occurring at approximately 11 seconds. The boron injection was initiated at 165 seconds including a 45 second delay. The calculation is being continued until the reactor hot shutdown is achieved.

For the ATWS calculation using the RAMONA code, an error in the steam line part of the code was discovered and corrected. The calculation has been successfully rerun for 300 seconds of transient. Typical results are shown in Figures 6.5 and 6.6.

During this reporting period, effort was made to compare the thermohydraulic performance of the RAMONA-3B and TRAC-BD1 codes for the same reactor power and feedwater flow boundary conditions. For this purpose, another TRAC-BD1 calculation was performed by imposing the RAMONA-3B calculated reactor power. This last calculation provided a one-to-one comparison between the RAMONA-3B and TRAC-BD1 predictions for the same reactor power and feedwater boundary conditions. The results of this comparison are shown in Figures 6.7 through 6.12. Figure 6.7 represents the reactor power calculated by the RAMONA-3B code. This reactor power was used as a boundary condition in the TRAC-BD1 calculation. As can be observed from Figures 6.8 through 6.12, the transient behaviors of the average fuel temperature, the steam dome pressure, the relief-and-safety valve flow, and the core and recirculation pump flow rates as predicted by the two different codes are quite close. This may be an indication that for the ATWS calculation, the differences in the results obtained from the two codes are mainly due to the difference in the neutron kinetics model.

6.2.3 RAMONA-3B Nodalization Study (G. Slovik)

During this quarter, a RAMONA-3B nodalization study simulating the Peach Bottom-2 Turbine Trip test #3 (Carmichael, 1978) has been completed. The initial conditions for the turbine trip test #3 can be found in Table 6.1. The nodalization of the original input (or reference) deck is outlined in Table 6.2.

The only modification made to the nuclear data during this study was to add a fuel parameter data set. This was done to collapse two zones in the fuel which became necessary in reducing the number of axial levels from 24 to 12 in the core. This particular collapsed node contained a region which was made up of a section containing burnable poison (i.e., gadolinium) while the other section did not. The new fuel data set was generated by taking the volume average for each of the coefficients in the diffusion coefficients and cross sections. This new set was then used in every calculation that used 12 axial levels in the core.

The modeling changes of the reactor were made by collapsing the reference case (i.e., 24 axial levels and 191 neutronic channels in a quarter

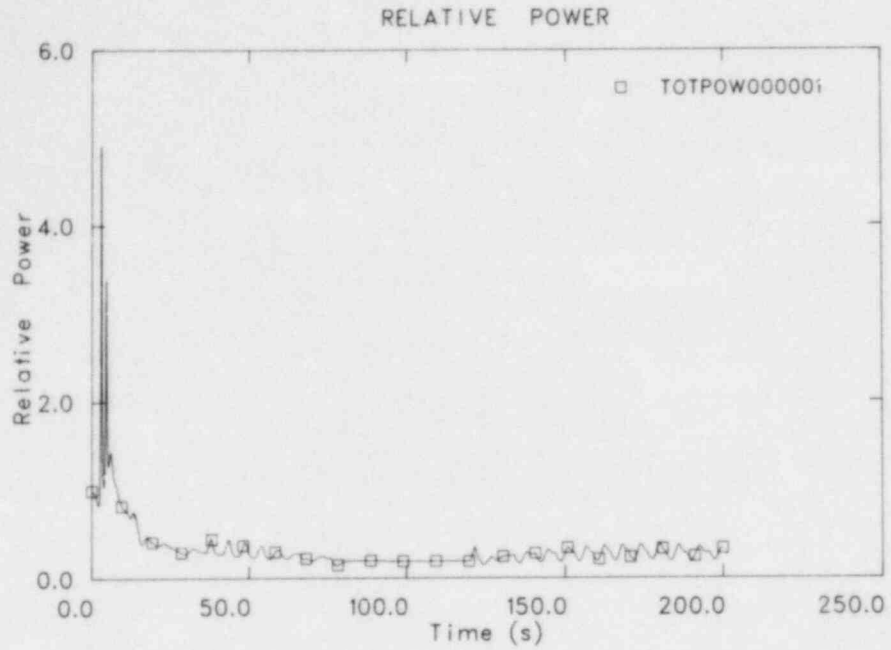

Figure 6.3 TRAC-BD1 Reactor Power for a BWR/4 MSIV Closure ATWS Event.

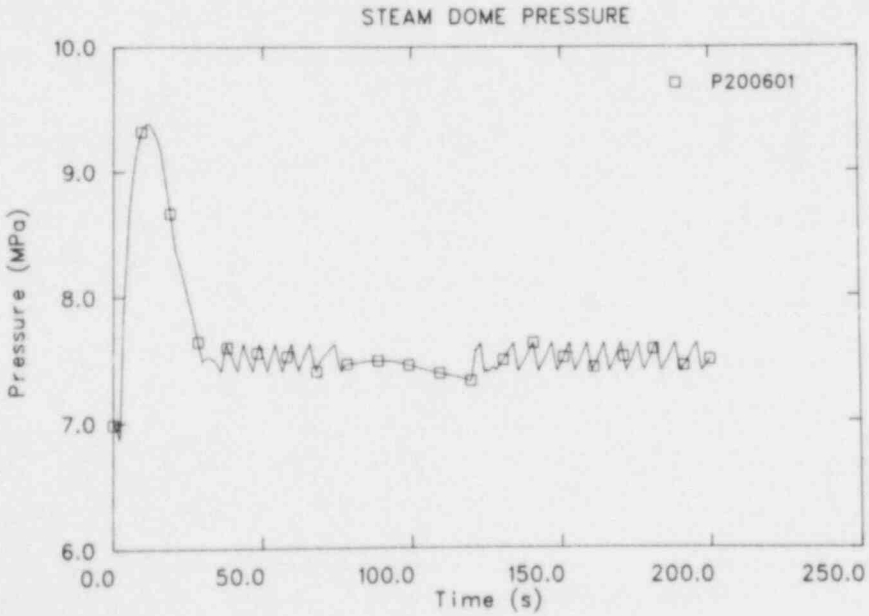

Figure 6.4 TRAC-BD1 Steam Dome Pressure for a BWR/4 MSIV Closure ATWS Event.

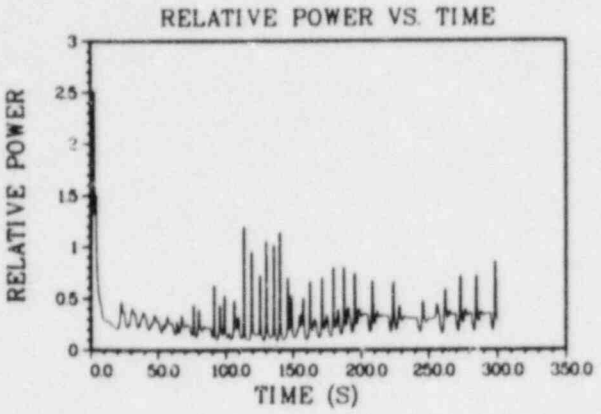

Figure 6.5 RAMONA-3B Reactor Power for a BWR/4 MSIV Closure ATWS Event.

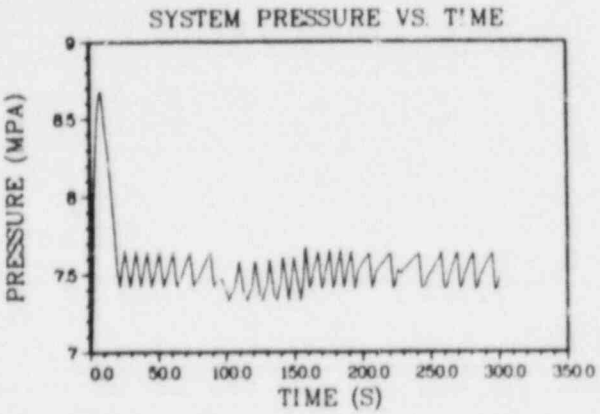

Figure 6.6 RAMONA-3B Vessel Pressure for a BWR/4 MSIV Closure ATWS Event.

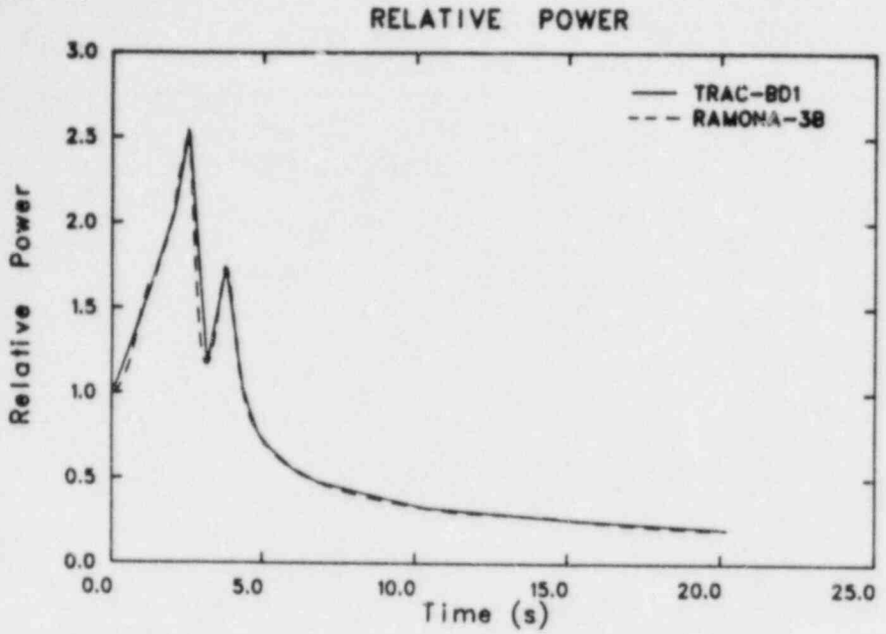

Figure 6.7 RAMONA-3B Reactor Power as Imposed on TRAC-BD1.

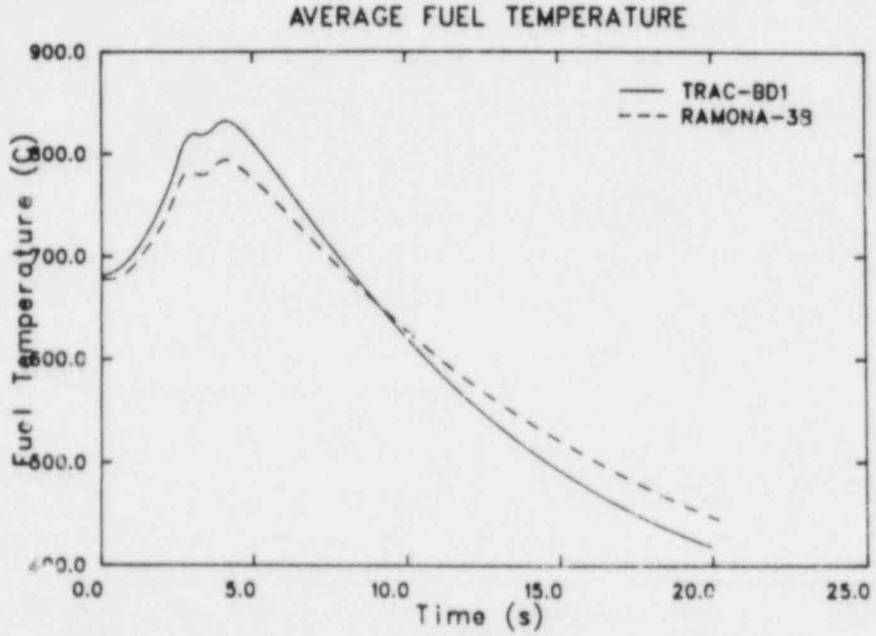

Figure 6.8 Comparison Between the TRAC-BD1 and RAMONA-3B Average Fuel Temperatures for the same Reactor Power and Boundary Conditions.

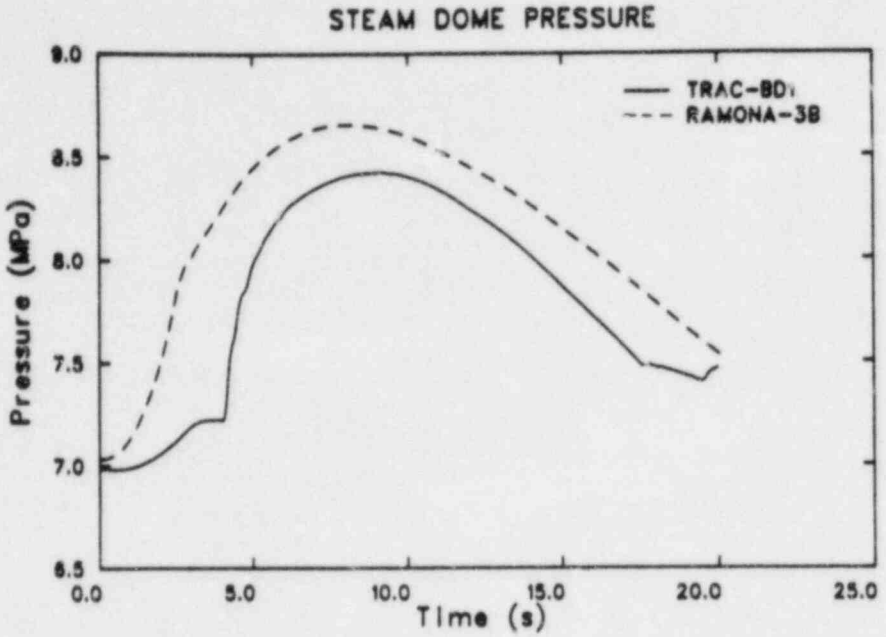

Figure 6.9 Comparison Between the TRAC-BD1 and RAMONA-3B Steam Dome Pressures for the same Reactor Power and Boundary Conditions.

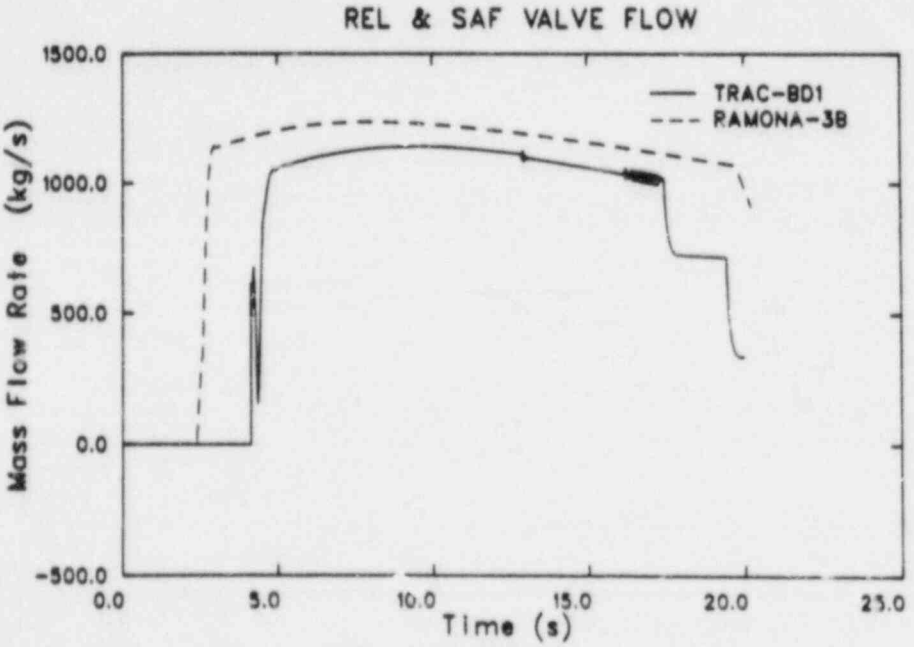

Figure 6.10 Comparison Between the TRAC-BD1 and RAMONA-3B Relief and Safety Valve Flow Rates for the same Reactor Power and Boundary Conditions.

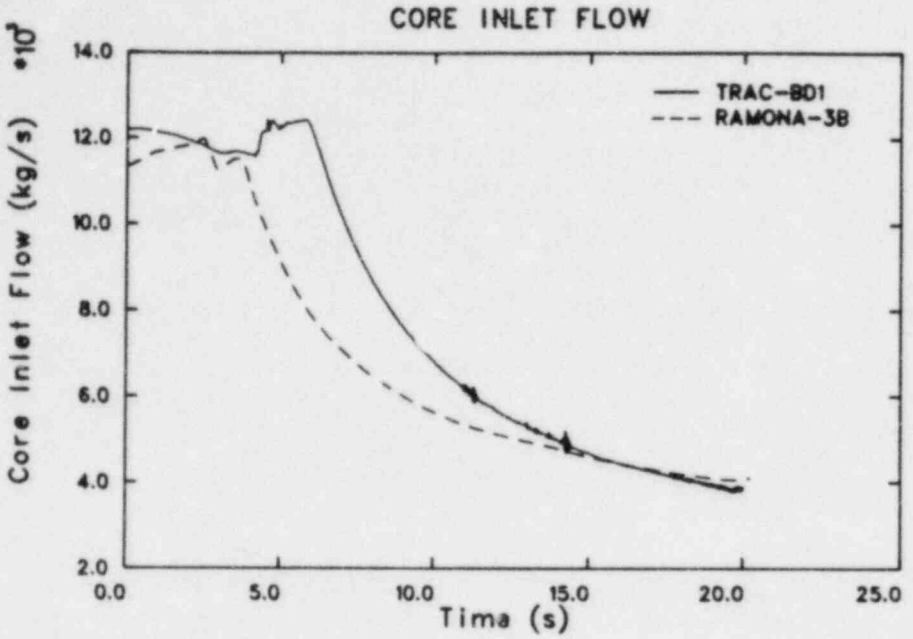

Figure 6.11 Comparison Between the TRAC-BD1 and RAMONA-3B Core Inlet Flow Rates for the same Reactor Power and Boundary Conditions.

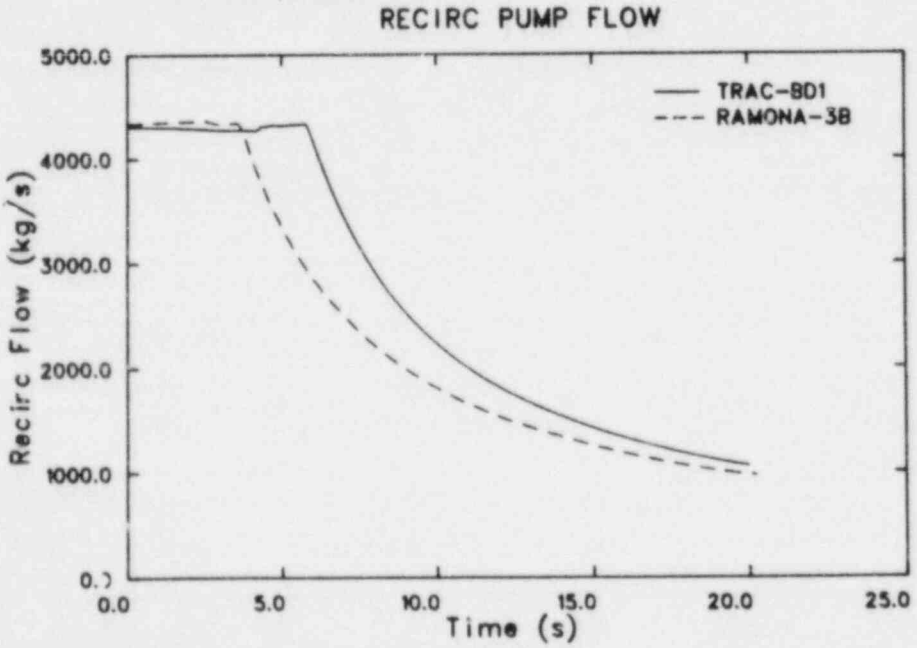

Figure 6.12 Comparison Between the TRAC-BD1 and RAMONA-3B Core Inlet Flow Rates for the same Reactor Power and Boundary Conditions.

core representation) which modeled the core by having 54 control blades and 31 hydraulic channels. The neutronic nodes represented each fuel assembly explicitly with each node having dimensions of $\Delta X = \Delta Y = 15.24$ cm and $\Delta Z = 15.24$ cm for 24 axial levels in the core. The first modified run (i.e., 12 axial levels and 191 neutronic channels in the core) was made by changing the axial levels from 24 to 12. The same extrapolation lengths used in the reference run were used to represent the reflectors, but new albedos were calculated to match the initial average axial power distribution. This type of adjustment was made for each nodalization. Also, it should be noted that the control blade pattern, as fixed by the initial test condition was used in the calculation.

The next modeling change was made by combining four assemblies into one neutronic channel. This was a relatively straightforward process because each control blade controls four assemblies; hence, the positioning of the fuel and its associated control blade was completely consistent with the reference case. This produced neutronic nodes that had dimensions of $\Delta X = \Delta Y = 30.48$ cm while $\Delta Z = 15.24$ and 30.48 cm to represent a core with 24 and 12 axial levels, respectively.

The final core model in this nodalization study had 12 axial levels and 22 neutronic channels. Difficulties arose in this nodalization because the nodes contained an equivalent of about 9 assemblies. Also, the hydraulic channels and control blades had to be remodeled since the reference case had 31 hydraulic channels and 54 control blades. Because of large neutronic nodes, the model lost its direct relationship to the details of the reactor core. Hence, the control blade pattern from the test data was abandoned and the control blade positions were adjusted to give the most correct initial average power distribution. Each node was assigned a unique hydraulic channel and control blade to preserve as much of the 3-dimensional effect as possible. For the neutronic nodes, this coarse mesh representation crossed many fuel zones and no clear collapsing was possible. However, the fuel types were arranged as appropriately as possible using the same fuel types in the reference case. The dimension of these neutronic nodes were $\Delta X = \Delta Y = 45.72$ cm and $\Delta Z = 30.48$ cm.

The initial relative axial power distributions for each of the different core nodalizations and the main global parameters predicted for this transient can be seen in Figures 6.13 through 6.16. A summary of the different nodalizations used, and the CPU time used to run each model out to 2.0s, are presented in Table 6.3.

It can be seen in Figures 6.13 and 6.14 that the core models that used either 191 or 55 neutronic channels were able to represent the initial power distribution reasonably well. This ability stems from the fact that in the 191 neutronic channels representation, each assembly in a quarter core was represented along with its assigned control blade, which in turn, controls the four nearest assemblies. This symmetry was taken into account when constructing the 55 channel case which grouped the four assemblies into one neutronic node; hence, the same control blade pattern as was used in the test was used in these models, thus contributing to good agreement with the

TABLE 6.1
PEACH BOTTOM-2 TURBINE TRIP TESTS
INITIAL CONDITIONS

Test No.	Power % Rated	Scram Setting % Rated	Core Flow % Rated	Core Pressure MPa	Inlet Temperature K
3	69.1	77	100.9	6.95	549

TABLE 6.2

NODALIZATION FOR TURBINE TRIP TEST CALCULATION

Region	Number of Nodes
Upper Downcomer	6
Lower Downcomer	6
Lower Plenum	5
Upper Plenum, Riser, Separator	5
Steam line	
Vessel to junction for Bypass Valve (BPV)	65
Junction for BPV to Turbine Stop Valve (TSV)	2
Junction for BPV to BPV	10
Core (one quadrant)	
Axial	24
Planar	
Neutron Kinetics	19
Thermohydraulics	31

data shown in Figures 6.15 and 6.16. The nodalizations with 24 and 12 axial levels showed that these two predicted almost identical results for the case with 191 neutronic channels. However, in Figure 6.15 the relative power for the case with 24 axial levels (and 55 neutronic channels) predicts the peak to within 6 percent while the case with 12 levels (and 55 channels) predicts the maximum value to within 10 percent. While these differences did exist, hydraulically the results of the 55 channel case were very similar to the reference case because the total integrated power was still close to the reference case. In Figure 6.16, this fact is borne out since the system pressure for the cases with 191 and 55 neutronic channels predicted the same pressure response.

TABLE 6.3

RUN TIME STATISTICS FOR PEACH BOTTOM TURBINE TRIP TEST #3

Core Nodalization		Total	Hydraulic	Total	CPU
Axial Levels	Neutronic Channels	Neutronic Nodes	Channels in Core	Hydraulic Nodes	Time (s)
24	191 (Reference)	4584	31	843	1578
12	191	2292	31	471	821
24	55	1320	31	843	683
12	55	660	31	471	384
12	22	264	23	235	299

For the case with 12 axial levels and 22 neutronic levels, the results were not as good. In Figure 6.14 it can be seen that the initial average relative axial power distribution was underpredicted in the lower part of the core and overpredicted near the top. This situation existed because the nodes encompassed about 9 assemblies on the horizontal plane. Hence, the effect of inserting a control blade into the node affected a larger area. RAMONA-3B was not designed to control this type of node; thus, the control blades are represented explicitly in the core which means that as the control blade moves into a core, the node preceding it must be completely rodded. While this is fine when representing one assembly at a time, it greatly underpredicts the nodal power when used in neutronic nodes containing 9 assemblies, particularly when each assembly may have a different control blade pattern. This problem can be circumvented by using the control density in a node; however, that option is not presently available in RAMONA-3B. This problem caused the underprediction of the relative power for the transient shown in Figure 6.15 which resulted in the system pressure being underpredicted, as shown in Figure 6.16.

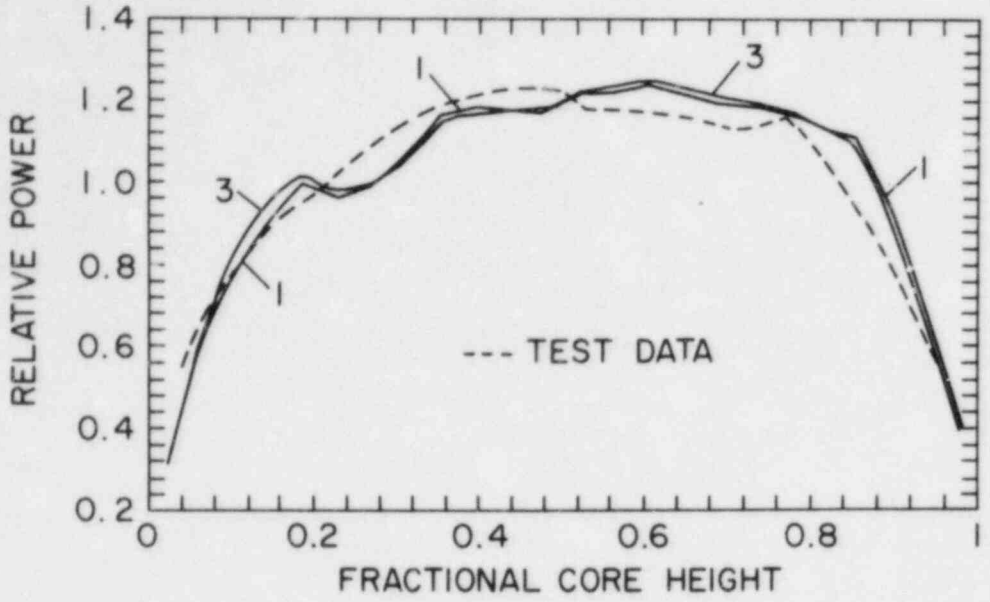

Figure 6.13 Comparison Between the Measured and RAMONA-3B Steady-State Axial Power Distribution (Case 1: 24x191 Neutronic Nodes, Case 3: 24x55 Neutronic Nodes). (BNL Neg. No. 11-65-83).

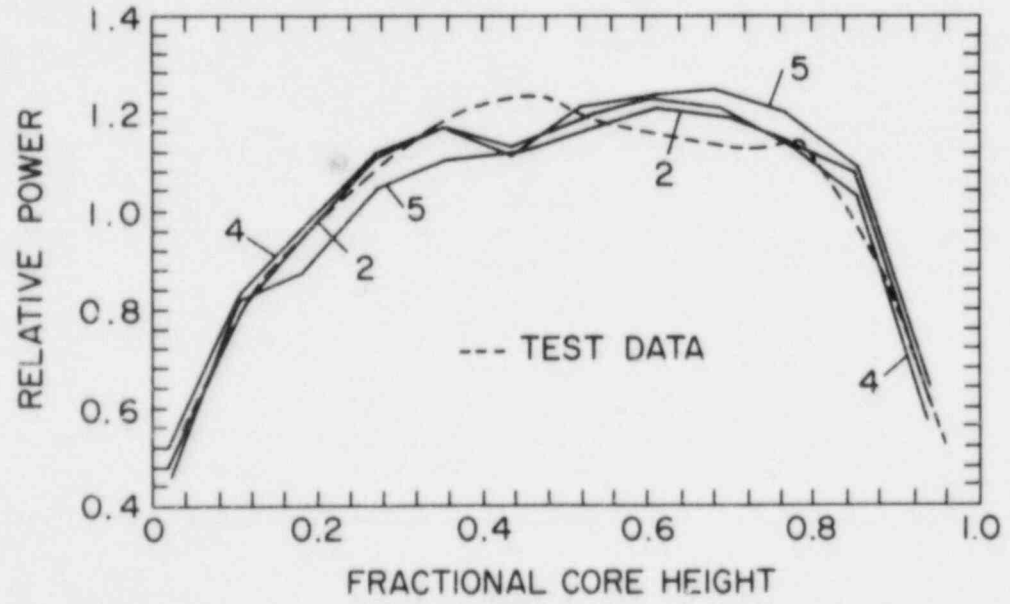

Figure 6.14 Comparison Between the Measured and RAMONA-3B Steady-State Axial Power Distribution (Case 2: 12x191 Neutronic Nodes, Case 4: 12x55 Neutronic Nodes, Case 5: 12x22 Neutronic Nodes). BNL Neg. No. 11-64-83

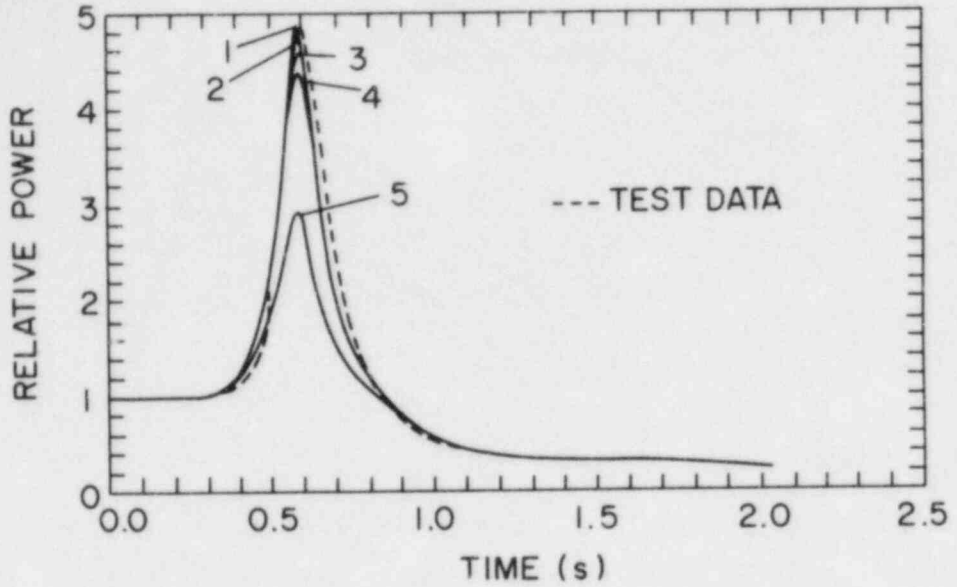

Figure 6.15 Comparison Between the Measured and RAMONA-3B Transient Total Power. (BNL Neg. No. 11-63-83)

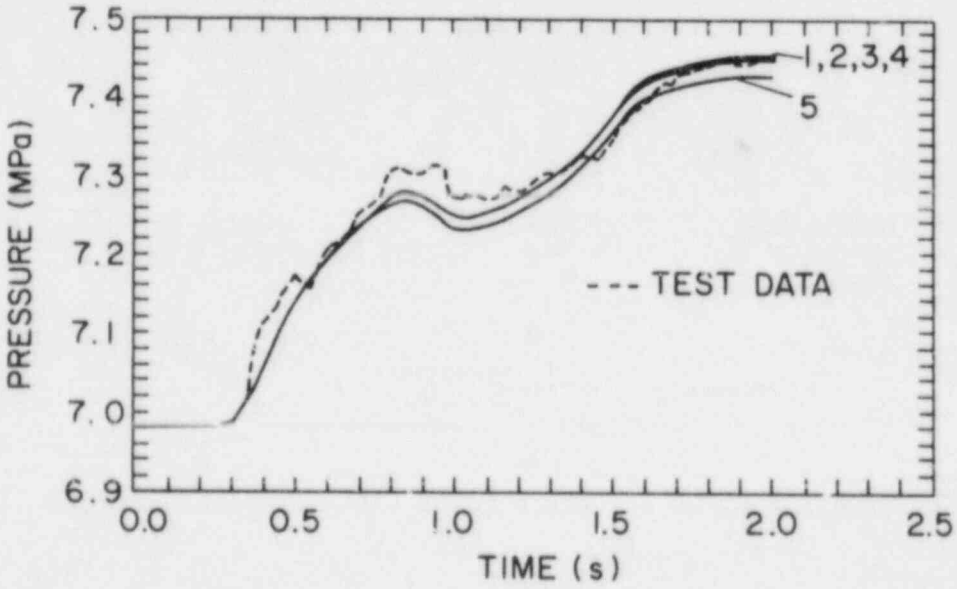

Figure 6.16 Comparison Between the Measured and RAMONA-3B Steam Dome Pressure. (BNL Neg. No. 11-62-83)

In conclusion, the predicted response of the Peach Bottom Turbine Trip Test #3 can be best simulated with a quarter core representation of one node per assembly (i.e., 191 neutronic channels) with either 24 or 12 axial levels in the core with equal results. This test can also be represented by using 55 neutronic channels because the control blade pattern can still be explicitly expressed. Hence, it would appear that a RAMONA-3B user can represent the core of Peach Bottom EOC-2 with reasonable accuracy by using a neutronic channel containing four assemblies. As seen in Table 6.3, the CPU time is greatly reduced with each reduction of the total number of neutronic nodes. Also, it was found that the number of assemblies in a node should not exceed four (4) since a control blade pattern cannot be accurately defined. This could be alleviated if a control density option was added to RAMONA-3B when called upon to use such large nodes, and should be considered for future improvement.

6.3 Peer Review of Systems Thermal Hydraulics for NRC PTS Study
(J. H. Jo, U. S. Rohatgi, and P. Saha)

BNL staff members attended the Calvert Cliffs Pressurized Thermal Shock (PTS) review meeting held at the Baltimore Gas and Electric Company in Baltimore, Maryland on September 20-21, 1983. The BNL staff also attended meetings on the H. B. Robinson PTS analysis held at Idaho Falls, Idaho on August 23-24, 1983 and September 29, 1983. Work has begun in reviewing the TRAC input deck for the Calvert Cliffs plant and the resultant steady state.

References

CARMICHAEL, L. A., and NEIMI, R. O., (1978), "Transient and Stability Tests at Peach Bottom Atomic Power Station Unit 2 at End of Fuel Cycle 2," EPRI NP-564.

HSU, C. J., (1983), "BWR/4 ATWS Calculations Using TRAC-BD1 and RAMONA-3B Codes," in Safety Research Programs Sponsored by Office of Nuclear Regulatory Research, Quarterly Progress Report, April 1 - June 30, 1983, NUREG/CR-2331, BNL-NUREG-51454, Vol. 3, No. 2 Section 6.2.2.

NEYMOTIN, L., (1983), "Analysis of Oak Ridge Post-CHF Tests with TRAC-BD1," in Safety Research Programs Sponsored by Office of Nuclear Regulatory Research, Quarterly Progress Report, January 1 - March 31, 1983, NUREG/CR-2331 BNL-NUREG-51454, Vol. 3, No. 1, Section 6.1.2, 1983.

WESTINGHOUSE ELECTRIC CORP., (1973), "Topical Report: Reactor Coolant Pump Integrity in LOCA," WCAP - 8163, September 1973.

YUELYS-MIKSIS, C., ROHATGI, U.S., and CONNELL, H. R., (1983) "LOCA Analysis of Westinghouse RESAR-3S Plants," in Safety Research Programs Sponsored by Office of Nuclear Regulatory Research, Quarterly Progress Report, April 1 -June 30, 1983, NUREG/CR-2331, BNL-NUREG-51454, Vol. 3, No. 2, Section 6.2.1, 1983.

7. Thermal Reactor Code Development (RAMONA-3B)

(P. Saha, L. Neymotin, and L. Moberg (ScP))

This project includes the modifications, improvements and preliminary (or developmental) assessment of the BWR transient analysis code called RAMONA-3B. Work on this project has been resumed after the conclusion of the BNL-Scandpower agreement on the release of RAMONA-3B. The code (RAMONA-3B) is now available, at no cost, to U. S. organizations for the analysis of U. S. reactors.

During this reporting period of July to September 1983, a collapsed water level tracking capability has been added to the RAMONA-3B code and significant progress has been made in implementing the feedwater and recirculation flow control systems. The work on collapsing the 3-D cross sections for 1-D calculations and reactivity edits, under subcontract to Scandpower is nearly completed. The details of the progress achieved are described below.

7.1 Collapsed Water Level Tracking Capability (L. Neymotin)

In addition to the existing two-phase mixture level tracking calculation in the downcomer, a procedure to calculate the collapsed water level has been implemented in RAMONA-3B. This capability is important for the correct initiation of the safety injection system and the feedwater control system currently being developed for the RAMONA-3B code. The code's output will include both the downcomer two-phase mixture and collapsed water level location history.

7.2 Feedwater Control System (L. Neymotin)

A stand-alone computer program was written for the feedwater control system and the check-out calculations and sensitivity studies have been performed. The control system structure (Jo, 1982), time constants and the controller gains have been taken from a RETRAN input deck (Forkner, 1978). A complete description of the system together with results of the developmental assessment will be presented when the system implementation into the RAMONA-3B code is completed.

7.3 Recirculation Pump Control System (L. Neymotin)

Development of the recirculation pump control system has reached the same stage as that of the feedwater control system mentioned above. Implementation will begin after the latest version of the code is created.

7.4 Support for the MSIV Closure ATWS Calculation (L. Neymotin)

A number of corrections to the code have been made and the calculation was successfully continued up to 1000 seconds of transient time. Results

for the first 300 seconds are shown in Figures 6.5 and 6.6 of Section 6.2.2 of this report. The final results will be discussed in the next quarterly report.

7.5 Improvement Tasks Performed at Scandpower (L. Moberg, ScP)

7.5.1 1-D Cross-Section Data Generation

A methodology for collapsing a 3-D cross section distribution to an equivalent 1-D (axial) cross section data set has been developed. The procedure consists of first performing a reference 3-D static calculation with RAMONA-3B followed by a series of perturbation calculations which reflect the cross section dependence on the free variables void, fuel and coolant temperature. Data files are saved from each of these cases and fed into a new stand-alone code, FRAM, which performs the actual collapsing. The 1-D data are fitted to polynomials producing a data file for use in a corresponding 1-D RAMONA-3B model. The coding of FRAM, and the required modifications to RAMONA-3B, have been completed and functionally tested at Scandpower.

7.5.2 Reactivity Edits

Edits of total reactivity, as well as the reactivity contributions from void, fuel temperature, coolant temperature and control rod effects have been implemented in RAMONA-3B. The total reactivity is calculated by two methods; from the inverse reactivity equation (point kinetics) and from the perturbation theory. The reactivity components are calculated from the perturbation theory, and are printed out at user specified intervals.

The coding of the reactivity calculations is completed and functionally tested at Scandpower.

References

FORKNER, S. L., (1978), "Calculation of Generator Load Rejection Transient for 3293 MW BWR with RETRAN-01-RET-12B," TVA Report, July 1, 1978.

JO, J. H., (1982), "Feedwater and Recirculation Flow Control," in Safety Research Programs Sponsored by Office of Nuclear Regulatory Research, Quarterly Progress Report for January 1 - March 31, 1982, NUREG/CR-2331, BNL-NUREG-51454, Vol. 2, No. 1, Section 5.3.4, pp. 102-104, July 1982.

II. DIVISION OF ENGINEERING TECHNOLOGY

SUMMARY

Stress Corrosion Cracking of PWR Steam Generator Tubing

The experimental program on stress corrosion cracking (SCC) at Brookhaven National Laboratory (BNL) is aimed at the development of a quantitative model for predicting the behavior of Inconel 600 tubing in high temperature aqueous media.

Laboratory tests involve U-bends, constant extension rate tests (CERT), and constant load. Plots are made of failure time and crack velocity vs. temperature, and also of SCC time vs. stress, using mainly pure water, and some tests with environments related to the ingredients of primary or secondary water. Cold work of Alloy 600 is also included.

SCC has now been found in four U-bends of production tubing exposed in deaerated pure water at 315°C and provide a continuous Arrhenius plot from 365°C to 315°C. CERT with 0.01% carbon material are now starting in secondary water ingredients. The CERT data curves continue to form a family of parallel semi-log plots, with no significant differences in slopes which correspond to Q = 33 Kcal/mole. Our data are in general agreement with crack velocities obtained at other laboratories in dilute deaerated sodium hydroxide. Tests at constant load are consistent with a log-log relationship between the applied stress and the time to fracture at 365°C for low carbon Alloy 600. Computer programs are being set up for handling the proposed model used for predictive purposes for Inconel steam generator tubing. The principal purpose of further data acquisition is to refine factors related to the environment and the condition of the tubing.

A proposed standard test procedure for ASTM balloting is near final modified form, dealing with Electrochemical Potentiokinetic Reactivation (EPR) tests used in detecting sensitization of stainless steels. The first ballot produced two negative votes, which will presumably be resolved by the presently outlined procedures.

The drastic reduction in funding for the FY 1984 SCC program will eliminate tests to make needed adjustments to the preliminary equations of the model, as well as its verification with tubing from the Surry steam generator which was taken to PNL.

Bolting Failure Analysis

Materials were assembled and the program completed for the study of the effects of lubricants on SCC of bolting materials. Notch-tensile specimens were machined from actual stock materials: ASTM A-197 B7 and A-540 B-24,

Class 2 and all testing has been completed. Additionally, the scanning electron microscopy work and coefficient of friction experiments have been completed. The report will be completed in the last quarter of 1983.

Probability Based Load Combinations for Design of Category I Structures

A probabilistic model for tornado load has been developed. Based on the model, a load combination methodology for tornado load and dead load has also been established. This method was applied to the Clinton containment structure for the evaluation of the limit state probability.

A reliability analysis method for shear walls has been developed and applied to a typical shear wall. This reliability analysis method can be used to evaluate the reliability level in existing structures and to derive load factors for design of shear walls.

Mechanical Piping Benchmark Problems

A draft report describing the blind prediction phase of the extended Z-bend physical benchmarking effort was completed. The report presents a comparison of the predicted and measured results. The study of multiple supported piping systems continues. The SAM analyses were repeated using new data and the inconsistencies previously observed were no longer evident. All previously developed tables of dynamic results were updated to include the newly developed results for uniform support excitation.

8. Stress Corrosion Cracking of PWR Steam Generator Tubing

(D. van Rooyen)

The objective of this program is to develop quantitative data to serve as a predictive basis for determining the useful life of Alloy 600 tubing in service. For this purpose, tests are being run on production tubing of Inconel 600 at different carbon levels to examine the various factors that influence the cracking of tubing. Verification was planned with tubing to be obtained from a decommissioned steam generator, but this will not be possible due to a reduction in funding level for 1984.

The present experimental program addresses two specific conditions, i.e., 1) residual stess conditions where deformation occurs but is no longer active, and 2) where plastic deformation of the metal continues, as would occur during denting. Laboratory media consist of pure water as well as solutions to simulate environments that would apply in service; tubing from actual production is used in carrying out these tests. The environments include both normal and "off" chemistries for primary and secondary water. Material condition also includes various degrees of cold work.

The results summarized here were obtained in several different tests. The main ones are 1) split tube "reverse" U-bends, 2) CERT, and 3) constant load. The temperature range covered is 290°C-365°C.

8.1 Constant Load

For the case where denting or active deformation is no longer occurring, it is necessary to obtain data that relate failure times to stress, i.e., the load on the tube. In service these stresses can consist of residual plus operational stress, and may be complex. Tensile specimens under applied load have given good data for 0.01% carbon Inconel, but not for 0.03 and 0.05% carbon heats, and the latter appear to need a different stress pattern. This type of exploration also will not be pursued due to lack of support.

The effect of temperature was shown in the previous report, together with the data from various environments. Cold work effects are not effectively sorted out by the constant load test, and have been discontinued. The long term, low stress test with as received material at 365°C continues, and a few additional tests are scheduled for 1984 in AVT.

8.2 CERT

CERT data on SCC require a better distinction between the initiation and propagation stages than can be achieved by our present extrapolation technique. Corrections are needed to improve the quantitative determination of SCC induction times, which are used for calculating crack propagation rates and used for predicting strain levels at which SCC will become a problem. An activation energy of 33 Kcal/mole continues to be the best value available for crack growth, pending the introduction of a better correction in the calculation.

We have discontinued plans for the new test that would permit simulation of an active dent.

Work on finalizing a design for a test intended to improve the accuracy of determining the initiation period during CERT in high temperature water has stopped.

8.3 U-Bends

Split tube type U-bends cracked in earlier tests at 325°C-365°C and suggested a possibility that the carbon level of the Inconel influences the crack initiation/temperature relationship, i.e., activation energy seemed to increase with increasing carbon content. A larger number of replicate samples have been exposed in water at 290°C and 315°C since 1981. These U-bends have not shown cracking for 0.02 and 0.03% carbon, but the 0.01% material showed cracks in four samples. These data plus earlier results at higher temperature are plotted in Fig. 1, showing a straight line Arrhenius plot of failure time vs. inverse absolute temperature. Some of the other materials (0.02 and 0.03%C) are now at points that may show an increasing activation energy at the lower temperatures, and they will continue for longer times.

Testing continues with tubes at 365°C in pure H_2O to correlate a static "dent" size with susceptibility to SCC of 0.01% C Alloy 600. The "dents" were made by pressing semicylindrical pieces of metal onto the outside surface while the tube is in a test jig. All materials are made out of Inconel 600, and the "dents" range from 5 to 40 mils (actual inward deformation). The exposure time is now over four months, without SCC.

8.4 Future Work

Little future work will be possible along lines of verifying and improving the reliability of our predictive model at the 1984 funding level. Its application at present is not believed to be more than semi-quantitative.

9. Bolting Failure Analysis

(C. J. Czajkowski and J. R. Weeks)

9.1 Effects of Lubricant in Causing Failure on Bolts for Nuclear Applications

Experimental work was completed on the project. The results have been evaluated and a report is being written. A draft of the report will be sent to NRC in December. The abstract from the investigation follows:

An increase in the number of bolting failures attributed to lubricant coolant interaction at nuclear power plants has caused a great deal of concern regarding the more judicious use of lubricants by the nuclear power industry. An investigation was performed on ten more commonly used lubricants by the nuclear power industry. The investigation included EDS analysis of the lubricants, notched tensile CER testing of bolting materials with the lubricants, frictional testing of the lubricants and weight loss testing of a bonded solid film lubricant. The report generally concludes that there is a good deal of variance in the mechanical properties of common bolting materials; that MoS_2 can hydrolize to form H_2S at 100°C, and that the use of copper containing lubricants can be potentially detrimental to high strength steels in an aqueous environment.

10. Probability Based Load Combinations for Design of Category I Structures

(H. Hwang, M. Reich, M. Chang, P. Brown, S. Kao
M. Shinozuka, B. Ellingwood and P.C. Wang)

10.1 Load Combination Methodology for Tornado Load

The tornado load is considered as a quasi-static load so that only the static responses of structures are taken into consideration. The occurrence of tornado is assumed to follow the Poisson arrival law during the structural lifetime. For each occurrence, the tornado wind force is idealized as a rectangular pulse with a random duration and a random intensity.

It is reasonable to believe that the duration and intensity, the two variables required in the procedure, are positively correlated. However, they can be treated as being independent in the reliability analysis for the following reasons. (1) For a tornado load alone, since the response analysis is static, the duration does not need to be considered. (2) In combination with other loads, Wen and Pearce (1981) showed that this type of correlation has only a minimal effect on the combined load probability, i.e., it can be neglected without causing any significant error.

According to Wen and Chu (1973), the mean annual rate of a nuclear power plant being hit by a tornado is given by

$$\lambda_{W_T} = \lambda^{(0)}_{W_T} \mu_A \tag{10.1}$$

where $\lambda^{(0)}_{W_T}$ is the mean occurrence rate of tornadoes ($1/mile^2/year$) at a site which can be evaluated from statistical data. μ_A is the mean damage area ($miles^2$), and is estimated to be 0.85 $mile^2$ by Schaefer, et al (1979). The mean duration μ_{DW_T} of a tornado acting on a power plant is also an important parameter. Following Wen's recommendation, the mean duration is taken to be 23.2 seconds in this study.

The pressure on the external surface of structures resulting from a tornado is

$$p = c_p q \quad (psf) \tag{10.2}$$

where $q = 0.00256V_T^2$ (psf) represents the dynamic pressure and V_T is the maximum wind speed (in mph and the sum of the translational and rotational components) generated by a tornado. C_p is the pressure coefficient and its value is either specified by codes or documented in reports.

The annual probability of a wind speed threshold v being exceeded at a site can be found in Reinhold and Ellingwood (1982). This is the probability of the joint event that the tornado wind speed exceeds v and a site is struck by a tornado. Since the mean annual rate of a nuclear power plant being hit by a tornado can be computed as indicated in Eq. 10.1, the conditional distribution of the maximum wind speed V_T, given a tornado hit the site under consideration, can be easily established. For the Clinton Power plant site, the conditional distribution of the maximum wind speed V_T

is

$$F_{V_T}(v) = 1 - 10e^{-0.0338v} \quad \text{for} \quad v \geq 75 \text{ mph} \tag{10.3}$$

For completeness of the distribution function of V_T, a linear form between v = 0 and v = 75 mph is assumed for $F_{V_T}(v)$. Then,

$$F_{V_T}(v) = 2.77 \times 10^{-3}v \quad \text{for} \quad 0 \leq v \leq 75 \text{ mph} \tag{10.4}$$

If one sets

$$W_T = V_T^2, \tag{10.5}$$

then the distribution function of W_T given a tornado hit can be expressed as follows:

$$\begin{aligned} F_{W_T}(w) &= 1 - 10e^{-0.0338\sqrt{w}} \quad \text{for } w \geq 75^2(\text{mph})^2 \\ &= 2.77 \times 10^{-3}\sqrt{w} \quad \text{for } 0 < w < 75^2(\text{mph})^2 \end{aligned} \tag{10.6}$$

On the basis of the above probabilistic model for tornado load, a load combination methodology for dead/live load and tornado load has been developed. This methodology together with the data indicated above has been applied to the Clinton containment structure. It is found that the conditional limit state probability of the critical element is about 1.15×10^{-10} based on the ultimate limit state defined in this program. The limit state probability in the lifetime of the containment 40 years, therefore, is about 0.18×10^{-11}.

10.2 Reliability Analysis of Shear Walls

A reliability analysis method for shear walls has been developed. In this method, a shear wall is modelled as a deep beam. The limit states for flexure and shear are defined according to the ACI strength design for combined axial and bending moments, and deep beam requirement for shear. To derive the statistical distribution of structural resistance, the variations of material strength and wall dimension are taken into consideration. At present, three loads, i.e., dead load, live load and earthquake ground acceleration, are considered in the reliability analysis. Both dead and live loads are assumed to be Gaussian distributed and the probabilistic model for earthquakes is the same as that used in concrete containment reliability analysis. Based on the above information, the limit state probabilisties for flexure and/or shear during the lifetime of the shear wall can be computed. This reliability analysis method has been applied to a typical shear wall, and the limit state probabilities are found to be about of the order of 10^{-4}. The details of the methodology and the numerical examples will be included in a technical report.

This reliability analysis method can be used to evaluate the reliability level of an existing shear wall, and to derive load factors for design of shear walls. In FY 84, this work will be expanded to include more loads, and a load combination criteria for design of shear walls will be suggested.

11. Mechanical Piping Benchmark Problems

(P. Bezler, M. Subudhi, Y.K. Wang, S. Shteyngart and R. Alforque)

11.1 Elastic Benchmark Development

Volume 2 of the benchmark report series is complete and has been reviewed by the NRC. The inclusion of an alternate problem taken from an actual reactor system and the impact of applicant comments from the trail usage phase are being considered before submitting the report for printing.

11.2 Physical Benchmark Development

A draft of the report describing the blind predictions for the extended Z bend test was completed. The report will be submitted for printing following NRC staff review.

Two analyses were performed for the extended Z bend. In the first analysis, the measured sled accelerations and displacements were used directly as input. In the second analysis, the measured sled accelerations were again used, however, the input sled displacements were the time history records produced when the measured acceleration records were twice integrated and baseline corrected. The inputs then, for the second analysis, were a consistent set. This was not necessarily true for the first analysis.

For both analysis, the independent support motion, modal superposition, time history algorithms were used with a 10 mode approximation and a integration time step of 0.001 sec. A uniform damping value of 2% was employed based on estimates from the test results. Lastly, the input displacement and acceleration time histories were digitized on 0.001 sec. intervals.

A listing of the predicted natural frequencies for the Z bend are presented in Table 11.1. The corresponding experimental estimates for the fundamental frequencies of the system are presented in the last column of this table. As can be seen, the agreement between the measured and predicted values is good.

The finite element model used in the calculations is shown in Fig. 11.1. The seismic inputs were imposed at nodes 1, 7 and 34. Figures 11.2 and 11.3 show time history traces of the measured and predicted displacements in the Z direction of nodes 15 and 26. On each of these figures the upper curve is the measured response, the center curve is the predicted response based on measured acceleration and displacement inputs (test input) and the lower curve is the predicted response based on measured accelerations and integrated displacement inputs (integrated test input). Figures 11.4 and 11.5 show time history traces for the measured and predicted accelerations in the Z direction at nodes 9 and 27. In these figures the upper curve is the measured data and the lower curve is the predicted data.

Considering the displacement results, the displacements predicted using the test inputs are almost identical to the measured results for the first 18 seconds. Beyond 18 seconds the measured results show greater amplification of the high frequency components of response resulting in higher peak amplitudes

than are evident in the predicted response. These differences become progressively more evident as the node numbers increase or the right support is approached. The greatest difference in peak amplitude occurs at approximately 19 seconds and expressed as a ratio is 1.35 for node 26 (Fig. 11.3). The general character of both response traces in this time regime, however, remain similar.

The correspondence between the displacements predicted using integrated inputs and the measured results seems at first glance poorer than that achieved for the test inputs. However, detailed comparisons indicate that the predicted response trace appears to be 180° out of phase with the measured trace. Taking this into account, the degree of correspondence in all key respects for these results are approximately equivalent to thos achieved for the test input analysis. That is, general wave character is similar and peak responses are in phase and show the same correspondence to the measured results.

A review of the acceleration results indicate that the degree of correspondence between the predicted and measured results are poorer than those observed for the displacements. For points 5, 9 and 11, located on the lower horizontal span, the agreement is good to 18 seconds with some deterioration after that time. For points 21 and 27, located on the vertical and upper horizontal spans respectively, the correspondence is poor. Throughout these traces, the response amplitudes differ with the differences becoming pronounced beyond 12 seconds. The greatest difference in amplitude, expressed as a ratio, was 1.5, at 19 seconds, for node 27 (Fig. 11.5).

The overall agreement between the predicted and measured results obtained for this physical benchmark are considered fair. The good agreement achieved for the displacement predictions are offset by the poorer agreement achieved for the acceleration predictions. This outcome is surprising as these results are not as good as those achieved for the first Z bend benchmark system, a system known ti incorporate a nonlinear element.

A bright spot in the analysis results was the relatively good correlation obtained for the displacements predicted using integrated displacement inputs. The Trifunac methods apparently yielded an accurate baseline correction of the input displacements over the entire time history. The 180° phase shift noted for these results appears correct and makes these displacements consistent with the measured accelerations in the Z coordinate direction. ANCO engineers, the organization that performed the test, when advised of this result, responded that there was a distinct possibility that the acceleration data for accelerations in the Z coordinate direction were phase shifted 180° relative to all other data.

11.3 Multiple-Supported Piping Systems

During this quarter, the studies for both dynamic and pseudo-static responses were completed for the two LLNL piping models and three BNL models. In addition, the dynamic response tables for the two LLNL models were updated to include results corresponding to uniform response spectrum analysis. For this analysis, an envelope spectra for each spatial direction was developed from all the support point spectra and then used as input for the analysis.

The modal and directional combinations for this case follow the guide-lines given in US NRC Regulatory Guide 1.92. All other input parameters used in this analysis were consistent with those used in independent response spectrum analysis.

The results for independent support motion are presented in tabular form. Table 11.1 - 11.4 summarize AFW piping model response comparisons for both the dynamic and static components. The tables indicate the node/element numbers, their components/type, time history results and the results for the different cases considered. For the dynamic analysis, the different cases represent the fourteen combination procedures between groups, modes and direction of excitation. Also included are the results corresponding to the uniform (or envelope) Response Spectrum (URS) method. For the SAM analysis, the five different methods constitute ten different cases. The results listed under each represent the percentage of conservatism associated with each parameter when compared to the time history value. If it is a negative number, it signifies that the BNL predicted value is less then the actual time history results.

The parameters chosen for comparison are the displacements and accelerations at selected nodal locations, and the resultant pipe moments and support forces at selected pipe element locations. Each predicted parameter calculated by any of the procedures is compared with the time history responses obtained from an independent time history analysis. A total of six different piping systems are considered in the study. The time history results for two piping systems were provided by LLNL. BNL predicted the pipe responses using the LLNL supplied data. Thirty-three different earthquakes were considered for these piping systems. For the other four piping systems, the analysis of three, for one seismic excitation, have been completed to date.

For the dynamic responses, the envelope spectrum analysis, which is current practice, yields conservative results except at some isolated locations. At these locations, the participation factors computed for independent excitation are large but cancel when uniform methods are used eliminating the phasing between support points. Even if the input spectra are large, the product of the above factor with the spectrum value result in a lower response. However, because of the complicated layout of a typical piping system, this effect does not occur frequently.

For the independent response spectrum methods, it is found that in general the absolute sum among groups yields the most conservative response. However, algebraic and SRSS combination between groups can go either way, although the mean values over all the earthquakes studied are conservative. The sequence between groups, modes and directions does not significantly alter the level of conservaties.

The pseudo-static responses predicted by any of the five methods reveal that there exists no unique method to predict this component of seismic response. BNL is currently involved in a parametric study to identify all the factors that influence the SAM responses. No particular conclusion has been reached at this time.

Table 11.1 Natural Frequencies.

Mode No.	Analytical Estimate Hz	Experimental Estimate Hz
1	8.7	8.4
2	17.4	18.4
3	20.9	
4	71.8	
5	72.6	
6	88.9	
7	106.8	
8	118.1	
9	145.4	
10	156.6	

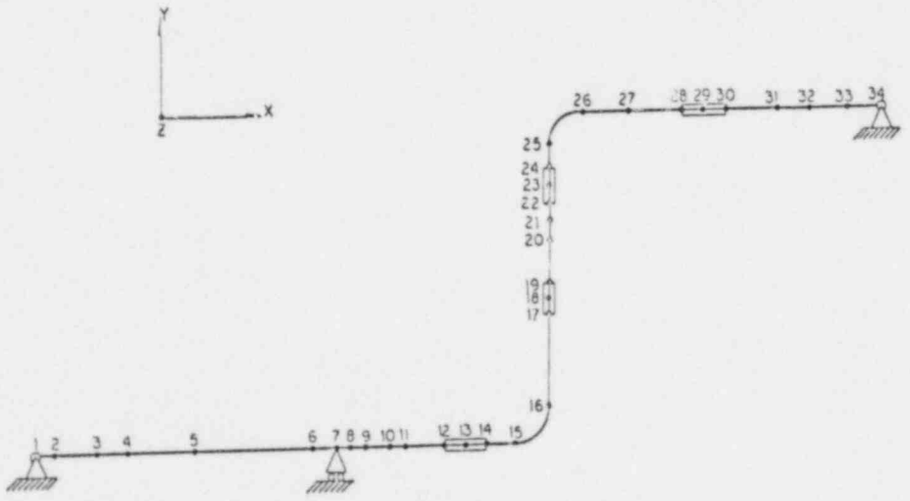

Fig. 11.1 Z Bend T6R1R Finite Element Model.

Table 11.2 Pipe Moment Responses (Dynamic) of AFW Model for Earthquake 15.

AFWSG1 MODEL

EARTHQUAKE NO. 15

*MOMENTS, AND FORCES(INERTIA COMPONENT)

ELEM. NO.	FORCE CODE	FORCE (T.H.)	URS	CASE NUMBERS (PERCENTAGE OVER TIME HISTORY (T.H.) VALUES) 1	2	3	4	5	6	7	8	9	10	11	12	13	14
10	12	.15352E+03	605	30	26	51	50	44	51	44	44	234	232	268	285	315	317
14	12	.31085E+03	624	30	27	52	51	46	52	46	46	241	240	283	293	323	324
18	12	.50048E+03	583	25	24	38	38	36	38	36	36	216	215	242	266	282	282
23	12	.50770E+03	556	23	22	30	30	29	30	29	29	199	199	212	249	257	257
34	12	.72801E+03	575	22	19	40	39	36	40	36	36	217	216	254	265	292	292
44	12	.44972E+03	490	20	16	39	38	31	39	31	32	201	199	249	249	291	294
52	12	.72559E+03	420	0	0	7	7	6	7	6	6	143	142	169	183	203	204
62	12	.75422E+03	523	18	17	28	27	25	28	25	25	190	190	217	239	260	261
71	12	.12298E+04	458	3	2	11	11	9	11	9	9	152	152	172	194	208	209
76	12	.55486E+03	606	42	40	49	48	44	49	44	45	230	229	262	289	320	323
82	12	.11794E+04	542	19	19	27	27	26	27	26	26	190	190	208	239	252	253
86	12	.46735E+03	644	36	34	49	49	45	49	45	45	229	228	270	284	318	319
93	12	.87656E+03	475	5	4	16	15	13	16	13	13	160	159	186	203	225	226
98	12	.43182E+03	474	10	9	24	24	20	24	20	20	168	167	213	216	261	262
101	12	.61886E+03	410	-11	-13	1	0	-3	1	-3	-3	113	112	145	146	174	175
108	12	.25052E+03	560	30	26	50	49	41	50	41	41	199	197	265	256	322	324
110	12	.66157E+03	427	4	2	18	16	12	16	12	12	144	143	197	187	245	245
121	12	.15758E+05	80	-2	-2	-13	-13	-13	-13	-13	-13	41	41	49	73	83	83
132	12	.16653E+05	65	-12	-12	-21	-21	-22	-21	-22	-22	28	28	34	57	65	65
133	12	.19611E+05	62	-23	-23	-30	-30	-31	-30	-31	-31	8	8	15	33	43	43
134	12	.95839E+04	132	24	24	11	11	11	11	11	11	82	82	94	127	140	141
157	6	.20478E+02	720	52	44	83	81	69	83	69	70	295	292	326	355	388	392
158	12	.40949E+04	130	7	7	-6	-6	-7	-3	-7	-7	53	53	61	87	95	95

Table 11.3 Support Force Responses (Dynamic) of AFW Model for Earthquake 15.

AFWSG1 MODEL

EARTHQUAKE NO. 15 *MOMENTS, AND FORCES(INERTIA COMPONENT)

ELEM NO.	FORCE CODE	FORCE (T.H.)	URS	CASE NUMBERS (PERCENTAGE OVER TIME HISTORY (T.H.) VALUES) 1	2	3	4	5	6	7	8	9	10	11	12	13	14
4	1	.52273E+02	548	31	28	33	31	28	33	28	28	192	189	218	243	275	278
5	1	.11654E+03	654	25	13	77	75	59	77	59	60	277	273	303	325	351	354
6	1	.51715E+02	593	48	38	54	50	38	54	38	40	206	199	257	261	314	319
7	1	.89431E+02	398	-10	-13	3	2	-2	3	-2	-1	112	110	154	148	191	193
8	1	.21906E+03	579	22	20	41	41	36	41	36	37	218	217	260	267	298	299
9	1	.58262E+02	470	42	34	36	32	23	36	23	25	160	153	204	220	273	280
10	1	.18432E+03	378	15	13	23	22	16	23	16	17	155	153	211	194	253	256
11	1	.95930E+02	171	-33	-38	-29	-31	-37	-29	-37	-37	28	25	53	71	99	102
12	1	.78347E+02	393	20	5	8	2	-12	8	-12	-10	117	108	138	176	204	211
13	1	.25860E+03	385	-1	-4	24	24	19	24	19	19	166	165	208	205	244	245
14	1	.49854E+02	453	24	13	37	32	21	37	21	22	162	154	213	235	300	304
15	1	.85402E+02	296	-2	-4	-8	-9	-15	-8	-15	-14	79	76	111	127	155	160
16	1	.38359E+03	450	5	3	20	19	16	20	16	16	167	166	205	210	238	239
17	1	.13854E+03	355	-7	-9	9	8	2	9	2	2	119	117	180	161	226	228
18	1	.21431E+02	528	16	15	24	24	22	24	22	22	184	183	198	230	238	238
19	1	.47415E+03	326	-17	-19	-9	-10	-13	-9	-13	-13	98	97	128	133	161	162
20	1	.42296E+03	431	0	-1	8	7	5	8	5	5	140	140	172	181	212	212
21	1	.28345E+0*	434	2	1	9	9	7	9	7	8	146	146	175	188	217	218
22	1	.40541E+03	444	2	2	9	9	8	9	8	8	150	150	164	192	210	210
23	1	.13808E+03	352	-10	-12	0	-1	-5	0	-5	-5	108	107	150	150	199	200
24	1	.56286E+03	379	-8	-9	1	0	0	1	0	0	123	123	156	162	197	197
25	1	.29571E+03	486	1	-1	19	18	12	19	12	13	140	139	189	180	229	230
26	1	.12894E+01	418	2	0	23	22	16	23	16	17	137	135	205	186	255	256
27	1	.22971E+04	132	-13	-14	-20	-20	-21	-20	-21	-21	16	15	28	47	64	64
28	1	.25751E+04	224	24	24	4	4	3	4	3	4	74	74	91	113	128	129
29	1	.40881E+04	212	8	7	-18	-18	-18	-18	-18	-18	34	34	43	68	75	75
33	1	.10868E+04	217	46	46	29	29	28	29	28	28	110	110	124	164	179	179
34	1	.65440E+03	203	25	24	28	28	25	28	25	25	119	118	148	162	196	197

Table 11.4 Pipe Moment Responses (Static) of AFW Model for Earthquake 15.

AFWSG1 MODEL

RESULTANT PIPE MOMENT RESPONSES FOR EARTHQUAKE NO. 15

				(PERCENTAGE OVER TIME HISTORY (T.H.) VALUES)							
		METHOD 1		METHOD 2		METHOD 3		METHOD 4		METHOD 5	
ELEM. NO.	T.H.	F=1.0	MAX. F	SRSS	ABS	SRSS	ABS	SRSS	ABS	SRSS	ABS
10	6.3230E+01	-80	5.02	2542	5119	-40	-4	318	681	350	546
14	8.2756E+01	-19	1.25	663	2363	1	25	375	876	300	512
18	8.7012E+01	-27	1.38	1275	3268	-11	5	309	794	259	500
23	1.0442E+02	-31	1.47	757	2331	-21	-1	191	581	99	261
34	9.3028E+01	-29	1.41	341	1591	-13	3	213	678	91	275
44	7.3355E+01	-4	1.04	231	975	-13	-2	190	550	-19	47
52	3.7375E+0	-41	1.70	854	2986	-24	2	739	1770	187	507
62	8.9644E+0	-5	1.06	322	1158	-19	2	263	673	63	226
71	8.7030E+01	-33	1.49	456	1632	-40	-14	194	679	249	533
76	9.0253E+01	-30	1.45	535	1868	-32	3	278	898	348	736
82	7.4864E+01	-59	2.48	1001	2934	-47	-21	318	1068	444	924
86	1.3366E+02	-53	2.16	240	1063	-54	-32	144	474	197	472
93	4.3398E+02	-58	2.40	146	690	-63	-47	108	315	161	371
98	7.2621E+02	-63	2.70	110	447	-68	-59	110	290	159	347
101	7.2099E+02	-59	2.46	106	414	-66	-58	104	270	166	353
108	2.7688E+02	-38	1.63	132	673	-16	21	116	412	315	501
110	1.7780E+03	-67	3.03	115	474	-68	-57	115	301	171	363
121	5.4567E+04	-32	1.49	21	127	-5	27	21	74	18	37
132	1.3688E+05	-35	1.54	13	60	-12	-3	13	43	-41	-35
133	1.4812E+05	-33	1.51	13	76	-11	5	13	46	-47	-41
134	4.5288E+04	-40	1.67	56	239	1	31	56	183	216	307
157	1.3428E+02	-36	1.57	606	1070	-23	-23	473	716	673	975
158	4.6506E+04	-18	1.23	309	553	-12	4	309	502	331	566

Table 11.5 Support Force Responses (Static) of AFW Model for Earthquake 15.

AFWSG1 MODEL

SUPPORT FORCE RESPONSES FOR EARTHQUAKE NO. 15

SUPP NO.	T.H.	METHOD 1 F=1.0	METHOD 1 MAX. F	(PERCENTAGE OVER TIME HISTORY (T.H.) VALUES) METHOD 2 SRSS	METHOD 2 ABS	METHOD 3 SRSS	METHOD 3 ABS	METHOD 4 SRSS	METHOD 4 ABS	METHOD 5 SRSS	METHOD 5 ABS
4	1.3611E+02	-29	1.41	1955	3525	-18	-8	458	725	666	976
5	5.5706E+01	-45	1.84	456	1562	-15	-9	380	792	270	452
6	9.0873E+01	-28	1.40	2816	5251	-23	-2	431	743	623	922
7	1.2005E+01	-26	1.36	4824	10389	-3	54	504	1112	409	625
8	2.2472E+01	-65	2.91	550	2361	-60	-41	318	873	380	678
9	2.2804E+01	-13	1.15	706	2290	-30	1	380	827	9	73
10	2.0162E+01	-27	1.38	586	2048	-5	10	475	1027	244	442
11	1.2663E+01	-29	1.42	1150	2815	-80	-69	1072	2105	-51	-19
12	3.1251E+01	-9	1.10	464	1152	-21	-19	459	1024	-86	-72
13	1.5608E+01	-51	2.05	462	2196	-30	7	289	963	170	467
14	5.5432E+01	-5	1.05	293	773	-18	-16	246	580	-86	-72
15	3.5051E+01	0	1.00	615	1359	-17	-12	258	607	6	76
16	1.1902E+01	-22	1.29	254	1396	-19	-2	184	586	73	220
17	1.0726E+01	-36	1.57	1719	3973	-56	-32	392	1098	535	1012
18	3.2004E+00	-51	2.08	411	1556	-56	-27	396	965	381	756
19	2.6373E+01	-57	2.34	373	2077	-6	59	251	987	287	675
20	2.4664E+01	-62	2.65	243	1508	-32	12	174	695	107	425
21	4.5706E+01	-64	2.85	758	2131	-66	-55	170	581	208	509
22	8.8370E+01	-62	2.65	451	1344	-68	-53	118	360	146	366
23	2.7434E+01	-37	1.61	408	1415	-47	-21	125	520	289	545
24	7.3225E+02	-63	2.70	110	425	-68	-67	109	271	145	326
25	4.6449E+02	-64	2.86	118	494	-66	-56	113	287	138	318
26	8.0199E+00	-55	2.25	128	497	-61	-36	128	409	111	265
27	3.0739E+03	-38	1.63	282	698	-70	-54	282	841	424	787
28	3.1577E+03	-40	1.69	89	450	-69	-52	89	298	470	675
29	1.0692E+04	-37	1.61	15	96	-17	-5	15	67	-1	17
33	8.4264E+03	-8	1.09	390	762	-25	11	390	727	469	880
34	8.0549E+03	-30	1.44	110	445	-77	-71	110	293	380	594

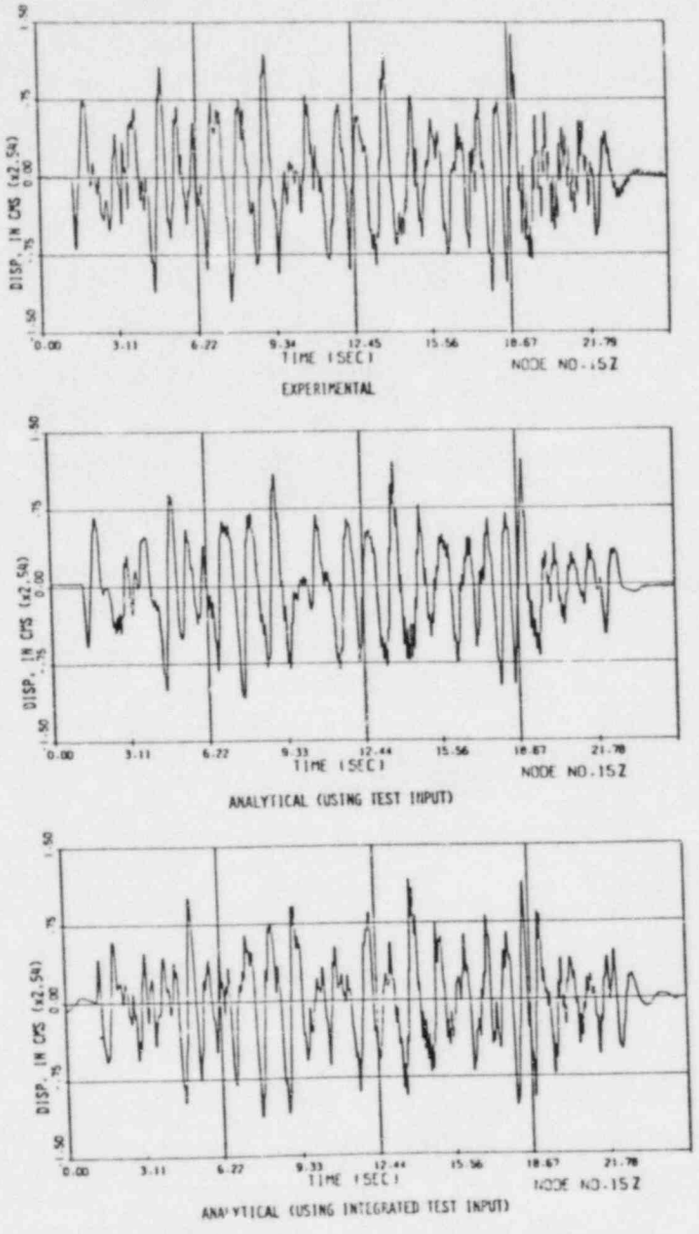

Fig. 11.2 Displacement Node 15Z.

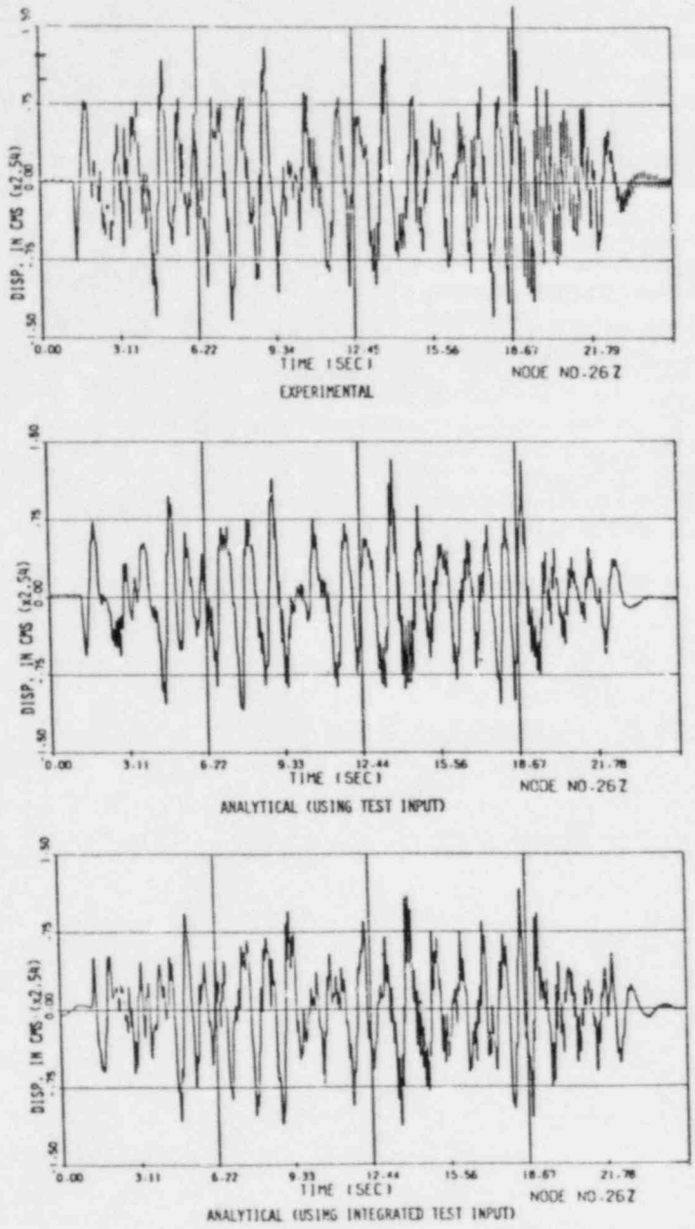

Fig. 11.3 Displacement Node 26Z.

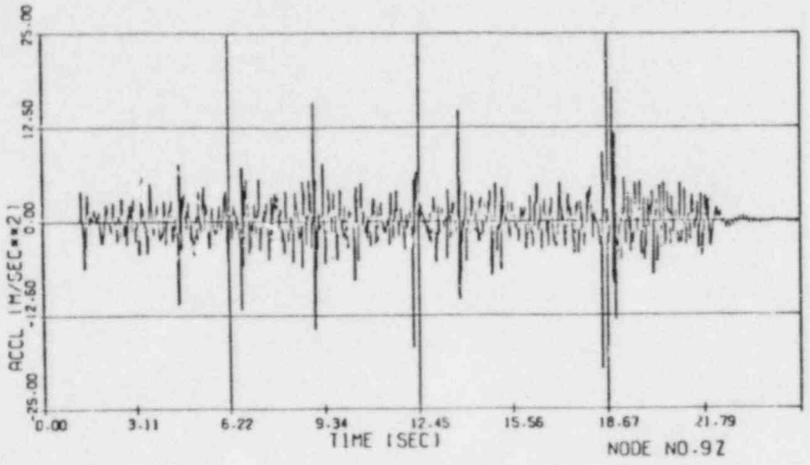

EXPERIMENTAL

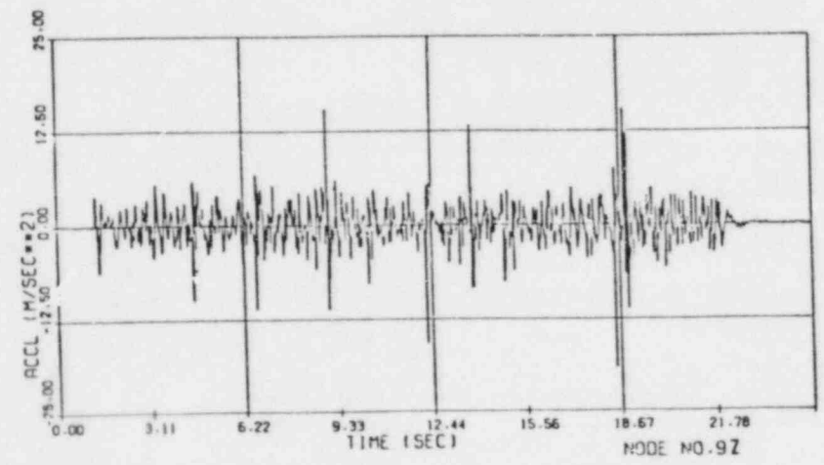

ANALYTICAL

Fig. 11.4 Acceleration Node 9Z.

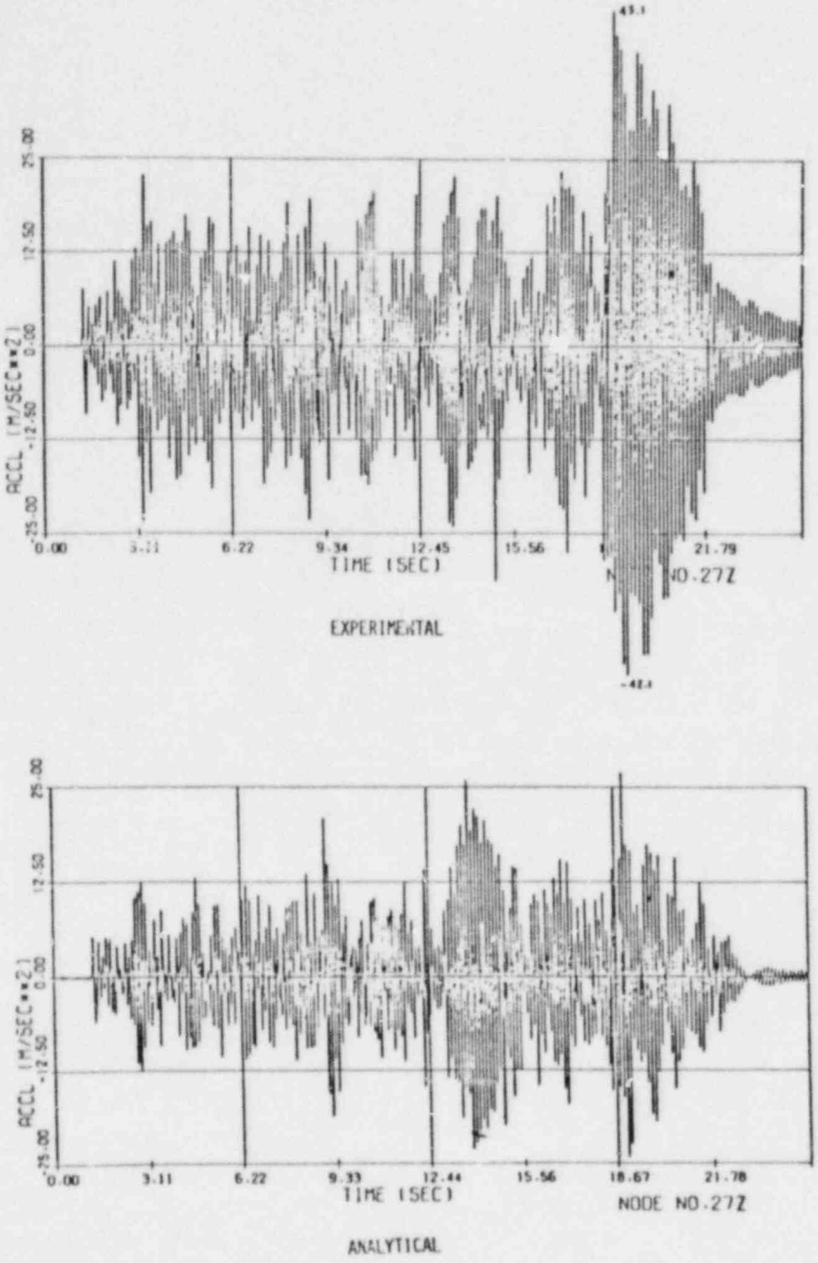

Fig. 11.5 Acceleration Node 27Z.

III. DIVISION OF FACILITY OPERATIONS

SUMMARY

Human Error Data for Nuclear Power Plant Safety-Related Events

Brookhaven National Laboratory has been tasked in this program to develop and apply realistic human performance data and models to help evaluate the human's role in nuclear power plant safety. To meet this objective, the major FY 1983 efforts are being placed in the following areas of investigation, namely:

- The development of Human Error Rates (HERs)
- The use of Performance Shaping Factors (PSFs) and quantified expert judgment in the evaluation of human reliability - the Success Likelihood Index Method (SLIM).
- The development of the Multiple Sequential Failure (MSF) Model.

Human Factors in Nuclear Power Plant Safeguards

Brookhaven National Laboratory has been tasked in this program to develop a long-term research plan for studying the effects of human factors on the security at nuclear power plants. In the past, relatively little attention has been paid to human factors affecting security personnel, in spite of the high level of attention the Three Mile Island 2 accident brought to human factors affecting operational personnel. In order to remedy this, the NRC is developing a coordinated long-term research plan, and to meet this objective, BNL will develop a planning document to assist NRC in identifying safeguards-related human factors research that can be undertaken over the next 5-7 years.

12. Human Error Data for Nuclear Power Plant Safety Related Events

(W. J. Luckas, Jr.)

Brookhaven National Laboratory (BNL) has been tasked in this program to develop and apply realistic human performance data and models to help quantify and qualify the human's role in nuclear power plant (NPP) safety. To meet this objective, the major FY 1983 efforts are being placed in the following areas of investigation, namely:

- The prediction of Human Error Rates (HERs) using Licensee Event Report (LER) data and nuclear systems expertise - a utility analysis.
- The use of Performance Shaping Factors (PSFs) and quantified expert judgement in the evaluation of human reliability - the Success Likelihood Index Method (SLIM).
- The development of the Multiple Sequential Failure (MSF) Model.

12.1 Utility Analysis of Using LER Data for HERs Prediction

(K. J. Voska, W. J. Luckas, Jr.)

The objective of this research has been the development of a methodology which can be used to obtain human error rate (HER) data from an analysis of Licensee Event Reports (LERs). A further objective was to assess the practicality, acceptability, and usefulness of using the HERs obtained to predict human error probabilities (HEPs) for use in Probabilistic Risk Assessment (PRA).

In order to calculate HER, the total number of observed errors must be divided by the total opportunity for error as follows:

$$\text{HER} = \frac{\text{total number of a particular type of human errors}}{\text{total number of opportunities for those errors}}$$

A method for the calculation of HERs was originally presented in NUREG/CR-1880 and -2417.

During the fourth quarter of FY 1983, a structured methodology for the identification, classification, and quantification of human errors found in LERs has been completed and subject to peer review. Copies of the methodology along with a short questionnaire were distributed to 20 human reliability experts. Responses received indicated the relative usefulness of the methodology and the confidence that could be placed in the resulting HERs in the opinion of those experts responding.

An assessment of the potential usefulness of existing LERs for human reliability predictions was made by evaluating the compatibility of human errors identified on LERs, with the human errors descriptions used in two well known data banks (NUREG/CR-2744 and -1278). By referring to the human errors

identified in LERs by NUREG/CR-2417 and -2987, an estimate of the total number of LERs that could potentially be used for HER calculations was made. The quality of the resulting HER data was evaluated in terms of reliability and validity by assessing the LER system as a measure of human performance.

With regard to practicality, a history of LERs and their availability was obtained through interviews with personnel at the NRC office of Analysis and Evaluation of Operational Data. In addition, consideration was given to difficulties that might occur in the necessary derivation of opportunity for error.

It has been assumed that the use of LERs to provide human error data which could be applied to improve the safety of nuclear plants is generally acceptable to the licensees and NRC.

The results of research conducted in this project in FY 1983 along with conclusions and recommendations have been documented in a draft report which has been submitted to the NRC for review. The report is entitled "Utility Analysis of Using Human Error Rates Developed from Licensee Event Reports to Predict Human Error Probabilities" and has been assigned: NUREG/CR-3519.

12.2 Success Likelihood Index Method (SLIM) Development
(D. E. Embrey of Human Reliability Associates)

The use of Performance Shaping Factors (PSFs) and quantified expert judgment using SLIM is important in the evaluation of human reliability. It should be noted that the amount of authentic quantitative human reliability data that exists is small (and is likely to remain small for the foreseeable future). It is therefore likely that subjective judgment and extrapolation will continue to play an important part. Nevertheless, present extrapolation techniques are covert, unsystematic, and rely on the knowledge of a limited number of judges. They do not systematically take into account the ways in which PSFs combine together to affect the probability of success in particular situations. Moreover, certain tasks cannot effectively be quantified using reductionist approaches. For these tasks, involving diagnosis, decision making and other cognitive activities, a holistic technique will probably be necessary.

Quantified subjective judgment has emerged from the previous analysis as being of critical importance for human reliability evaluation. SLIM is a quantified subjective judgment approach which uses PSFs as comprising any or all of the factors which combine to produce the observed likelihood of success. The basic premise of the approach is that when an expert judge (or judges) evaluate(s) the likelihood that a particular task will succeed, he or she is essentially considering the utility of the combination of PSFs in the situation of interest in either enhancing or degrading reliability. SLIM has the means of positioning a task on a subjective scale of likelihood of success, which is subsequently transformed to a probability scale. This positioning is derived by considering the judges' perceptions of the effects of the PSF in determining task reliability. NUREG/CR-2986 documents the initial appraisal of SLIM.

During the fourth quarter of FY 1983, efforts were devoted to determining the progress completed to date on the extension of the original SLIM concept, now called SLIM-MAUD (Success Likelihood Index Method using Multi-Attribute Utility Decomposition). The addition of MAUD to the basic SLIM procedure represents the incorporation of an interactive microcomputer based program into the elicitation procedures so that assessors may generate their own PFSs. The assessor generated PSFs are evaluated for theoretical consistency by the program and then converted to failure probabilities. An assessment of progress on the development of the MAUD addition to SLIM is an essential precursor to the actual field testing of the technique.

12.3 Multiple Sequential Failure Model Development
(P. K. Samanta, J. N. O'Brien)

The dependence of human failure on multiple sequential action is important in the evaluation of human reliability. NUREG/CR-2211 has analyzed the nature of this dependence and has distinguished it from other types of multiple failures. Human error causes selective failure of components depending on when the failure started. Two models have been initially developed for quantifying the failure probability in a multiple sequential action. The first is very general in nature and does not require any dependent failure data. The failure probability obtained from this model is a conservative one with associated uncertainty. The uncertainty is calculated considering many possible sources such as data, coupling, and modeling. In the second model, details of the process in multiple sequential failures (MSF) are taken into account. The model increments the conditional failure probabilities by a certain amount from their lower bounds (independent failure probability). This approach provides important insights into the influence of dependence of failures on system reliability. The model can be used effectively to choose an optimum system considering the individual failure probability, dependence factor, and the amount of redundancy in a system.

During the fourth quater of FY 1983, the small-scale psychological experiment being used to test the model was further developed. Programming of test sequences was initiated and experimental tasks were tentatively identified. Development of subject training approaches was undertaken along with other experimental design requirements. The experiment is scheduled to be fully underway during the next quarter.

References

COMER, M. K., KOZINSKY, E. J., SECKEL, J. S., AND MILLER, D. P. (1983). "Human Reliability Data Bank for Nuclear Power Plant Operations," NUREG/CR-2744.

EMBREY, D. E. (1983). "The Use of Performance Shaping Factors and Quantified Expert Judgement in the Evaluation of Human Reliability: An Initial Appraisal," NUREG/CR-2986.

HALL, R. E., FRAGOLA, J. R., and LUCKAS, W. J., JR., Tech. Eds. (1981). Conference Record for NRC/BNL/IEEE Standards Workshop on Human Factors and Nuclear Safety, NUREG/CP-0035.

HALL, R. E., FRAGOLA, J., and WREATHALL, J. (1982). "Post Event Human Decision Errors; Operator Action Tree/Time Reliability Correlation," NUREG/CR-3010.

LUCKAS, W. J., JR. and HALL, R. E. (1981). "Initial Quantification of Human Errors Associated with Reactor Safety System Components in Licensed Nuclear Power Plants," NUREG/CR-1880.

LUCKAS, W. J., JR., LETTIERI, V., and HALL, R. E. (1982). "Initial Quantification of Human Error Associated with Specific Instrumentation and Control system Components in Licensed Nuclear Power Plants," NUREG/CR-2416.

SAMANTA, P. K. and MITRA, S. P. (1981). "Modeling of Multiple Sequential Failures During Testing, Maintenance, and Calibration," NUREG/CR-2211.

SAMANTA, P. K., HALL, R. E., and SWOBODA, A. L. (1981). "Sensitivity of Risk Parameters to Human Errors in Reactor Safety Study for a PWR," NUREG/CR-1879.

SCHMALL, T. M., Ed. (1979). Conference Record for NRC/BNL/IEEE Standards Sponsored December 1979 Workshop on Human Factors and Nuclear Safety.

SPEAKER, D. M., THOMPSON, S. R., and LUCKAS, W. J., JR. (1982). "Identification and Analysis of Human Errors Underlying Pump and Valve Related Events Reported by Nuclear Power Plant Licensees," NUREG/CR-2417.

SPEAKER, D. M., VOSKA, K. J., AND LUCKAS, W. J., JR. (1983). "Identification and Analysis of Human Error Underlying Electrical/Electronic Component Related Events Reported by Nuclear Power Plant Licensees," NUREG/CR-2987.

13. Human Factors in Nuclear Power Plant Safeguards

(J. N. O'Brien)

Brookhaven National Laboratory (BNL) has been tasked in this program to develop a long-term research plan for studying the effects of human factors on the security at nuclear power plants. In the past, relatively little attention has been paid to human factors affecting security personnel, in spite of the high level of attention the Three Mile Island Unit 2 accident brought to human factors affecting operational personnel. In order to remedy this, NRC is seeking a coordinated, cost effective, long-term research plan. To meet this objective, BNL is developing a planning document to assist NRC in identifying safeguards related human factors research that can be usefully undertaken over the next 5-7 years.

13.1 Safeguards Related Human Factors Research

The first step employed to develop this research plan was to assess four principal data sources to identify and rank in importance human factors affecting safeguards. These are: (1) a human factors analysis of the Safeguards Summary Event List, (2) a set of comments supplied by over twenty human factors and/or safeguards experts, (3) an extensive literature review, and (4) NRC's own survey and analysis of human factors affecting safeguards (NUREG/0768).

During the fourth quarter in FY 1983, a third draft interim report was prepared which discussed the results of a literature review on social scientific research design with particular emphasis on how to design research approaches for safeguards human factors problems. This draft was combined with the two interim reports discussed last quarter to form the basis of an overall final report.

The format of the final report is in two volumes. Volume I is a summary of the overall research effort and a presentation of the final research plan. It contains an overall description of the four major program elements which are: (1) training and performance evaluation, (2) organizational factors, (3) man-machine interface, and (4) trustworthiness and reliability. For each program element, several project descriptive statements are included to specifically describe the optimal sequence of research efforts. Volume II contains all three interim reports condensed as chapters in the volume. Chapter 1 is an introduction; Chapter 2 describes the effort and results of identifying and ranking safeguards human factors issues; Chapter 3 contains an analysis of the feasibility of research on those issues identified in Chapter 2; and Chapter 4 documents the literature review conducted to investigate scientifically valid research approaches applicable to the issues identified.

The entire plan was presented to the NRC staff in a high-level briefing and it is expected to be available in published form during the next quarter.